UNIVERSIDAD DE CONCEPCIÓN
DIRECCIÓN DE POSTGRADO
FACULTAD DE INGENIERÍA - PROGRAMA DE DOCTORADO EN CIENCIAS DE LA INGENIERÍA CON MENCIÓN EN INGENIERÍA QUÍMICA

ATOMISTIC STUDIES OF WATER TRANSPORT IN NANOFLUIDIC CONDUITS

POR

ELTON EDGARDO OYARZUA VARGAS
CONCEPCION - CHILE 2018

Tesis para optar al grado de Doctor en Ciencias de la Ingeniería con mención en Ingeniería Química

Tutor: Dr. Harvey A. Zambrano
Departamento de Ingeniería Química
Facultad de Ingeniería - Universidad de Concepción

Co-tutor: Dr. Jens H. Walther
Departament of Mechanical Engineering
Technical University of Denmark

Advisor	:	Dr. Harvey A. Zambrano
Co-advisor	:	Dr. Jens H. Walther
Evaluation Committee	:	Dr. José Matias Garrido
		Dr. Alejandro Pacheco Sanjuan

Dedicado a mi familia ...

Acknowledgments

First of all, I would like to thank Harvey Zambrano for giving me the opportunity to perform this research under his guidance. For almost five years he continuously encouraged me to pursue the evidence of things and to seek the fundamental knowledge. I would also like to thank Jens Walther for his mentoring in computing, the valuable discussions on each APS-DFD, and for being a great host during my visits to DTU. Additionally, I would like to thank the Department of Physics at the Technical University of Denmark for the computational support and Petros Koumoutsakos at the Chair of Computational Science at ETH Zurich for allowing me to use the FASTTUBE package.

I would like to thank the entire crew of the Department of Chemical Engineering at UdeC, for being a real support during my PhD. Specially to the "NanoLab guys" for all the scientific discussions and the good moments. I would also like to thank to the heads of the PhD program of Chemical Engineering during my stay here: the former head of the program, Andrés Mejía and the current, Romel Jimenez, for being a real support during my PhD.

I am deeply grateful to my family and Miska for believe in me and for giving me the emotional support. All my effort is for them.

Finally, I wish to thank CONICYT and the Government of Chile, under the Doctorado Nacional Program, for giving me the founding to carry out this research and for giving me the possibility to perform this PhD.

Abstract

The dynamic and static behavior of fluids in contact with a solid substrate at the nanoscale has been the subject of intense study during the last two decades due to its important role in medicine, biology and engineering. Moreover, advances in fabrication techniques are making possible the design and development of functional nanofluidic devices with unprecedented capabilities based on the unique dynamical, structural, electrokinetic, mechanical and thermal properties of nanocofined fluids. Therefore, in order to fabricate these highly accurate systems and design its functional parts, a fundamental understanding of the transport of fluids inside basic nanostructures is required.

In this thesis, molecular dynamic simulations are employed to investigate the transport of fluids in nanoconduits, addressing different physical transport mechanisms for driving water flows. Nanoscale capillarity is studied as the mechanism inherent in the filling of fluids at the entrance of hydrophilic channels. The atomistic description of the capillary filling process confirms that spontaneous imbibition follows a purely inviscid flow regime with constant velocity during the very first stage of imbibition. Thereafter, the capillary filling kinetics evolves to a developing flow where the capillary force is balanced by contributions from inertia and viscous drag losses.

A fundamental analysis of the thermophoretic motion of water droplets in carbon nanotubes (CNTs) is also developed within this thesis, focusing on the relation between the advancing velocity of the droplet, the thermophoretic force, and the retarding friction force at the wall. The results indicate that the thermophoretic force is not velocity dependent while the friction force increases linearly with the droplet speed. Furthermore, we find that the magnitude of the thermophoretic force is determined by the imposed thermal gradient and the particular length of the droplet. These conclusions provide further insight into the water transport through CNTs with implications in nanosensors, CNT membranes and molecular sieving processes. Finally, the capability of CNTs subjected to a thermal gradient to sustain continuous and fast water transport is investigated. Therefore, by exploiting the thermal fluctuations inherent in the molecular scale, a nanomotor based on the thermal Brownian ratchet concept is proposed. The device consists of a single-wall CNT filled with water and including fixed points along the carbon nanotube under an imposed thermal gradient. The mechanisms driving the fluid flow are thermally induced asymmetric oscillations along the CNT, which propel the fluid in a constant, whip-like motion.

Resumen

El comportamiento dinámico y estático de fluidos en contacto con un substrato en la nanoescala ha sido sujeto de un intensivo estudio durante las últimas dos décadas debido a su relevancia en medicina, biología e ingeniería. Del mismo modo, los avances en técnicas de fabricación están haciendo posible el diseño y desarrollo de dispositivos nanofluídicos con capacidades sin precedentes, basados en las extraordinarias propiedades dinámicas, térmicas y eletrocinéticas de los fluidos nanoconfinados. En consecuencia, con el fin de fabricar estos sistemas altamente precisos, y diseñar sus partes funcionales, es que el entendimiento fundamental del transporte de fluidos al interior de nanoestructuras es necesario.

En esta tesis se utilizaron simulaciones de dinámica molecular para investigar el transporte de fluidos en nanoconductos, analizando diferentes mecanismos de transporte para impulsar flujo de agua. Se estudió el fenómeno de capilaridad en la nanoescala como el mecanismo inherente en el llenado de canales hidrofílicos en etapas tempranas. La descripción atomística del llenado capilar confirma que la entrada espontánea sigue un régimen puramente inercial descrito por una velocidad constante durante sus primeros instantes de llenado. Posteriormente, el llenado capilar adquiere un flujo desarrollado en el cual la fuerza capilar es balanceada por las contribuciones de disipación viscosa y el momento inercial.

En esta tesis también se realizó un análisis fundamental del movimiento termoforético de gotas de agua confinadas en nanotubos de carbono (CNTs), con especial énfasis en la relación entre la velocidad de avance de la gota de agua y las contribuciones de la fuerza termoforética y la fuerza de fricción en la pared. Los resultados obtenidos indican que la fuerza termoforética no depende de la velocidad de avance de la gota, mientras que la fuerza de fricción incrementa linealmente con esta velocidad. En esta investigación se encontró además que la magnitud de la fuerza termoforética es determinada por el gradiente de temperatura impuesto y el largo particular de la gota. Estos resultados entregan un mayor entendimiento sobre el fenómeno de termofóresis en gotas de agua confinadas en CNTs, con implicaciones en el desarrollo de nanosenores, membranas de filtración y procesos de separación. Finalmente, en esta tesis se estudió la capacidad de los CNTs para conducir un movimiento continuo de agua mediante la aplicación directa de un gradiente de temperatura. Para ello se ha propuesto un nanomotor basado en el concepto de motor térmico Browniano el cual aprovecha las fluctuaciones térmicas inherentes en esta escala molecular. El dispositivo consiste en un CNT de capa simple, completamente lleno de agua, con puntos fijos específicos a lo largo del nanotubo de carbono más un gradiente de temperatura impuesto axialmente. En este dispositivo, el mecanismo que impulsa el fluido son las oscilaciones térmicas asimétricas inducidas a lo largo del CNT, las cuales rectifican el movimiento del fluido en un movimiento constante de tipo “latigo”.

Contents

List of Figures

List of Tables

Nomenclature

Acronym

CNT	Carbon Nanotubes
FFT	Fast Fourier Transform
Kn	Knudsen number
LJ	Lennard-Jones
LOC	Lab-On-a-Chip
LW	Lucas-Washburn
MD	Molecular Dynamics
MM	Molecular Mechanics
NEMD	Non Equilibrium Molecular Dynamics
SCP/E	extended simple point charge water model
TBM	Thermal Brownian Motor
TTAMm	Tsuneyuki-Tsukada-Aoki-Matsui modified potential for silica

Greek Symbols

γ	Surface tension
μ	Viscosity
ω	Torsion angle
σ	Collision diameter for LJ potential
τ_T	coupling constant of the Berendsen thermostat
θ	Contact angle or bending angle
ε	Well depth parameter for LJ potential
ε_0	Vacuum Permittivity
φ	Phase factor

Latin Symbols

$\mathbf{f}_i$	Force vector
$\mathbf{r}_i$	Position of the i particle
Ã	Helmholtz free energy
G	Gibbs free energy
E	Energy
F_F	Friction force
F_N	Net force or total force
F_T	Thermophoretic force
N	Number of particles in a system or sub-system
q	partial atomic charge
r	Distance between center of mass of two particles
r_{list}	Neighbor list radius
T_0	Target Temperature
U	Potential Energy

Chapter 1

Introduction

The dynamic and static behavior of fluids in contact with a solid substrate at the nanoscale has been the subject of intense study during the last decades due to the its importance in numerous industrial and natural processes, such as water distribution in soil by porous media [1, 2], fluid behavior in biological systems [3, 4], or filling in microfluidic channels [5, 6]. In fact, because of the nanotechnological revolution at the hands of constant miniaturization, manipulating fluids at the nanoscale has become relevant. Nanoscale devices, or nanodevices, such as Lab-On-a-Chip [3, 5, 7] or DNA chips [8–10] are examples of that ongoing size reduction trend. Therefore, in order to fabricate these highly accurate devices and design its functional parts, a comprehensive understanding of the behavior of fluids at the nanoscale is necessary [11].

At the molecular level, owing to the relevance of the intermolecular interactions such as the electrostatic forces or the steric repulsion, fluids under confinement experience spatial distributions departing from the classic bulk behavior [12]. Furthermore, thermal fluctuations become relevant at this length scale, being an important factor when the collective behavior of fluids is analyzed [13, 14]. Therefore, classical macroscopic properties such as viscosity, density or conductivity are distorted from the continuum framework, showing spatial distributions or depicting unexpected behaviors [14–16]. These arguments suggest that the dynamic behavior of fluids at the nanoscale cannot be treated according to the classical framework of continuum hydrodynamics.

In order to generate a continuous fluid flow in nanoscale devices, several mechanism has been proposed, such as pressure gradients [17], electrokinetic transport [18, 19] and thermal gradients [20, 21]. Among these mechanisms, the application of temperature gradients is highlighted because it takes advantage of the thermal fluctuations inherent in the molecular scale [22]. Moreover, the application of two temperatures to generate a thermal gradient in a system is experimentally feasible and effortless in comparison to other mechanisms [23, 24]. However, a nanoscale device capable of supplying a continuous water flow by imposing thermal gradients has not yet been proposed experimentally. This is mainly explained because the understanding of the fluid behavior at the nanoscale is still in progress and the fundamental investigations that evaluate the rectification of fluid flows by taking advantage of the thermal fluctuations are very few. The rectification of fluid motion by using thermal gradients is based on the Smoluchowski-Feynman ratchet concept. This molecular ratchet concept state that in order to produce useful work from the random motion of molecules, two conditions need to be satisfied: (i) the breaking of spatial symmetry and (ii) the breaking of thermal equilibrium [25, 26]. Following these two concepts, the thermophoresis mechanism is also described. This phenomenon occurs when a solid particle, or liquid cluster, is subjected to a thermal gradient in a surrounding medium, triggering a di-

rected motion of the object. Therein, the momentum transfer in the hot side of the solid particle overcome the transfer momentum from the cold side, generating a net motion towards the cold side.

Computational simulations of molecular systems have proven to be a powerful and revealing tool for the study of the individual and collective behavior of atoms and molecules. The Nobel Prize of chemistry in 2013 for "*the development of multiscale models for complex chemical systems*", awarded jointly to Martin Karplus, Michael Levitt and Arieh Warshel is a demonstration of that fact. Computational simulations have served to explain and to interpret behaviors that experimental research, due to the limitation of the length scale and the high costs associated, cannot attain. In addition, with the correct scientific basis and detailed justification, investigations performed with computational simulations can make a leap forward in terms of scientific advance. Thus, disclosing behaviors that can be useful for the manufacture and performance of novel technological applications.

In this thesis, the computational technique of molecular dynamics is employed to investigate the transport of fluids in nanoconduits at different stages. The capillary phenomenon is studied at the entrance of hydrophilic channels. The atomistic description of the capillary filling process on its earliest time stages delivers a complete characterization of the kinetics of imbibition in nanodevices. A fundamental analysis of the thermophoretic movement in carbon nanotubes is also developed on this thesis. The direct motion of a water droplet inside a carbon nanotube is analyzed, focusing on the relation between the advancing thermophoretic velocity of the droplet and the retarding friction force at the wall. The results of this investigation indicate that the thermophoretic force is not velocity dependent while the friction force increases linearly with the droplet speed. Finally, in order to contribute to the investigation of nanoscale devices capable of supplying a continuous fluid flow by imposing thermal gradients, a nanomotor based on the thermal Brownian ratchet concept is proposed. The device consists of a single-wall CNT filled with water and strategic fixed points along the carbon nanotube. The proposed thermal Brownian motor is able to pump continuous flows with average velocity up to 5 m/s. Other devices based in the Smoluchowski-Feynman ratchet concept are also proposed within this thesis. The hypotheses and objectives of this thesis are presented in the following.

1.1 Hypotheses

- The capillary filling of water in hydrophilic channels, with at least one dimension in the nanometric scale, can be classified within the different capillary regimes of imbibition proposed in the literature. Moreover, during the capillary filling, an air gas overpressure in front of the advancing meniscus is observed.

- Considering the dynamic behavior in the thermophoretic motion of a water droplet inside carbon nanotubes, a dependency of the thermophoretic force with the advancing velocity is expected.

- A nanomotor based on the thermal Brownian ratchet concept is capable to perform fast and continuous water flow through a nanoconduit.

1.2 Objectives

1.2.1 General Objectives

Using molecular dynamics simulations, different physical transport mechanism for driving water flow in nanoconduits are studied. The main goal of this investigation is to deliver a further understanding of the fluid behavior at the nanoscale which is imperative for the development of a new generation of nanofluidic devices.

1.2.2 Specific Objectives

- Analyzing the capillary action of water in silica nanochannels at early stages of imbibition surrounded by air gas.
- Studying the kinetics associated with thermophoresis of water nanodroplets confined inside single wall carbon nanotubes and their interplay with the solid–liquid friction force.
- Proposing a thermal Brownian motor which enables a continuous water flow through a carbon nanotube by imposing an axial thermal gradient along its surface.

Chapter 2

Transport Mechanisms

Nature, from its inherent processes or phenomenons, holds up this world and the universe into its harmonic functioning. As rational thinking human beings, we have led to the analysis and categorization of each of these processes according to our perspectives. Perspectives that have evolved along with knowledge and scientific development.

In nature, fluids experience motion given by different conditions: two reservoirs at different pressures, different concentrations of solute or the presence of an electric field, for example. Due to the different conditions and applicability, many of those mechanisms are still the subject of incessant research. Nowadays, owing to the nanotechnological revolution and the incessant miniaturization of length scale, many of these transport mechanisms need to be analyzed and characterized in dimensions never studied before [27, 28].

In this chapter, the main transport mechanisms involved in this thesis are discussed. These phenomenons will be described in physical terms within a historical context and will serve to define the conceptual framework and establish the scope of this thesis. The first transport mechanism to be discussed is the capillary filling in nanochannels, subsequently the thermophoresis phenomenon, and finally the thermal Brownian ratchet concept to produce useful work from the random fluctuation of molecules.

2.1 Capillarity

Capillarity, or capillary action, is the ability of fluids to travel in narrow spaces due to the action of the free surface of the liquid in contact with an attractive solid. This phenomenon has been studied for centuries, and the first studies are often attributed to Leonardo da Vinci [29, 30]. However, the first recorded study was made by Robert Boyle in 1660 [30]. Then, the capillary action was analyzed by Newton and Hauksbee in 1712 [31–33], studied by Jurin in 1717 [34] and explained by Young in 1805 [35] and Laplace in 1806 [36].

In general, capillarity is understood as a competition between the cohesion of the fluid and the adhesion of the liquid with the solid. In other words, how the intermolecular forces of the atoms or molecules in the liquid are related with the molecular interaction between the atoms of the liquid and the atoms at the interface of the solid wall. These concepts and a further explanation of the definitions that account for capillarity, such as surface tension or capillary pressure, are discussed in the following.

2.1.1 Surface Tension

The surface tension is the concept that arise when an interface is discussed. This concept was first introduced to explain the curvature of droplets with a macroscopic smooth shape [36]. With the development of the molecular theory, the surface tension concept evolved to include the molecular interactions [37]. In general, the surface tension is defined as the change of energy per unit area. For example, if two flat liquids of the same substance and surface area are separated by a minimum distance, the work done (or the energy involved) to join these two liquids describe the surface tension of the substance (see Figure 2.1), which will differ depending on the substance. This change of energy per area also describe the surface tension between two different substances and different phases. From statistical thermodynamics, depending on whether the system under study is at constant volume, V, or constant pressure, p, the definitions of the surface tension are,

$$\gamma \equiv \left(\frac{\partial \tilde{\mathrm{A}}}{\partial A}\right)_{V,T} \quad ; \quad \gamma \equiv \left(\frac{\partial G}{\partial A}\right)_{p,T} \tag{2.1}$$

where $\tilde{\mathrm{A}}$ is the Helmholtz free energy, G the Gibbs free energy, and T the temperature of the system. Equation 2.1 serve as a general definition of the surface tension. Nevertheless, from a practical point of view, the mechanical statistical approach, in terms of the pressure tensor, is more appropriate. From a planar interface, the surface tension can be obtained as an integral over the difference of the uniform normal pressure P_n and tangential P_t components of the pressure tensor across the interface [38, 39],

$$\gamma = \int \left[P_n(z) - P_t(z)\right] dz \tag{2.2}$$

where z is the direction parallel to the normal of the interface surface. This approach has some implications on the shape of the interface being analyzed and where the surface interface is defined (dividing surface), leading to a controversial and not fully understood curvature effects on the surface tension [39–42].

From the mechanical point of view, the surface tension can be regarded as an attractive force tangent to the surface or parallel to the interface [43]. However, nonequilibrium and rate-dependent interactions lead to hysteresis effects, where very different paths and forces can be experienced depending on the rates at which surfaces are moved. These processes lead to very different forces, but the net energy change is the same [37].

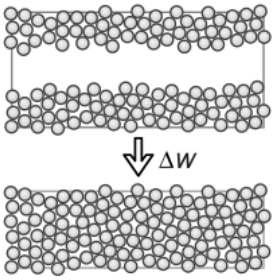

Figure 2.1: Sketch of the work done by joining two flat fluids describing the surface tension (Reprinted from ref. [37]).

2.1.2 Capillary pressure

Young in 1805 [35] and Laplace in 1806 [36], independently described the capillary action and the cohesion of the fluids in a curved surface in terms of an acting pressure in the interface. Since the concept of a gradual interface between the liquid and vapor phase was developed in the 20th century, Young and Laplace studied the interface from the macroscopic view of a smooth and sharp surface.

The concept of a pressure arises from Newton's third law. Considering a spherical droplet, if a "superficial cohesive" force contracts the droplet (surface tension), an opposite reaction force is expected to maintain the equilibrium of the droplet. Thus, according to Young and Laplace, the pressure difference between the reactive force per surface area and the outside vapor pressure is proportional to the tension and inversely proportional to its radius. In the general form, this pressure difference is [44],

$$P_l - P_v = \gamma \left(\frac{1}{R_1} + \frac{1}{R_2} \right) \tag{2.3}$$

where R_1 and R_2 are the two local radii of curvature in the planes perpendicular to the normal of the surface. In this way, the Young-Laplace equation relates the pressure in the interface with the radius of curvature. For example, in a flat surface, according to equation 2.3, the Young-Laplace pressure is zero. Furthermore, some considerations must be taken when the curvature is either positive (convex) or negative (concave), leading to a positive pressure difference or negative.

2.1.3 Contact angle

In theory of surfaces, by considering a system with three different phases, the angle that appears in the contact line where the three immiscible phases meet, is called the contact angle. The most fundamental example is a droplet in contact with a solid wall as shown in Figure 2.2.a, where the contact angle is defined as the tangent of the circumferential shape of the droplet in the limit with the solid.

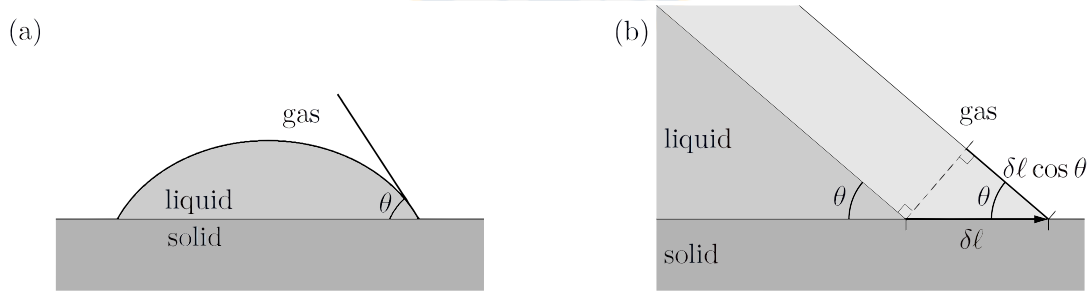

Figure 2.2: (a) Representation of the contact angle of a droplet in equilibrium with a solid surface. The angle in the tangential three-phase limit is the contact angle. (b) Differential area extension in the three-phase limit. Source: Own elaboration.

The contact angle is a macroscopic observable that describes the equilibrium state of the three phases in a system, which is fundamental to understand the surface interactions and the capillary action. For a droplet on a solid wall, the three interfaces involved are the solid-liquid, liquid-gas and gas-solid, leading to a thermodynamic equilibrium of the surface tensions γ_{sl}, γ_{lg} and γ_{sg}. The energy balance at equilibrium for the Gibbs energy is,

$$\delta G = \delta G_{sl} + \delta G_{lg} + \delta G_{gs} = 0 \tag{2.4}$$

Then, by considering a differential increased area in a wall of length l and depth w, as depicted in Figure 2.2.b, and the definition of surface tension from equation 2.1, thus

$$\gamma_{sl}(w\delta l) + \gamma_{lg}(w\delta l \cos\theta) + \gamma_{gs}(w\delta l) = 0 \tag{2.5}$$

By rearranging the contact angle, the Young's equation is obtained

$$\cos\theta = \frac{\gamma_{sg} - \gamma_{sl}}{\gamma_{lg}} \tag{2.6}$$

As a consequence of a curved interface in a capillary tube, the capillary or Laplace pressure arise due to imbalance generated as the tensioned interface is curved by the wettability action. In this process, the surface tension of the liquid-vapor acts as a force parallel to the interface contracting the meniscus, whereas the solid-liquid surface tension attracts the liquid to the solid. At steady state, the capillary pressure due to the curvature, results in a force opposing to the normal of the meniscus interface, pulling the fluid in a motion known as capillary action. The force balance in the capillary front is performed in the next section, with a description of the different regimes presented in capillarity.

2.1.4 Capillary regimes

At the begging of the 20th century, two researchers independently described the dynamics of the capillary action. Lucas in 1918 [45] and Washburn in 1921 [46] solved a mathematical model, based on the Poiseuille flow, describing the filling velocity of a fluid in a capillary. This equation comes from a pseudo-steady state balance between the viscous forces or the drag that comes from the walls, and the capillary forces that pull the fluid according to Young-Laplace. The Lucas-Washburn equation has been widely used in the study of capillarity [47–49]. However, this equation predicts an infinite velocity at very short times, as discussed below, thus it cannot be applied at early stages of the capillary filling. Recent studies [50–54] have proposed that the dynamic of the capillary filling can be divided in different regimes wherein the viscous and capillary forces dominates at different filling stages.

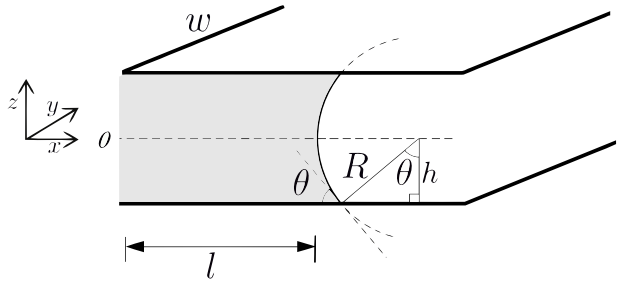

Figure 2.3: Schematic of the capillary filling in an infinite parallel walls system. Source: Own elaboration.

In order to describe the capillary regimes, a general force balance in the capillary front will be performed, according to the schematic of Figure 2.3. This force balance is mainly based in the work of Xiao et al. [55] who performed a capillary force balance by taking into account the analysis

of previous works [51,56]. The force balance developed in the following is performed in a parallel plates system, as shown in Figure 2.3, where the depth of the channel, w, is assumed infinite. Considering a deformable control volume inside the channel (grey area in Figure 2.3) [55, 57] and by neglecting gravity, the only forces acting in the fluid are the capillary force and viscous forces [50, 51, 55], thus,

$$\frac{d(m\langle v_x\rangle)}{dt} = F_{cap} + F_{vis} \tag{2.7}$$

Due to the development of a velocity profile in the flow, the average condition $\langle v_x\rangle$ of the velocity profile is assumed as the representation of the capillary motion. The left-hand side of equation 2.7 is expanded using the chain rule,

$$\frac{d(m\langle v_x\rangle)}{dt} = m\frac{d\langle v_x\rangle}{dt} + \langle v_x\rangle\frac{dm}{dt} \tag{2.8}$$

Assuming a fully developed parabolic profile with no-slip (Poiseuille flow profile), the velocity v_x is [55, 56],

$$v_x = \frac{3}{2}\frac{dl}{dt}\left(1 - \left(\frac{z}{h}\right)^2\right) \tag{2.9}$$

where dl/dt is the rate of progression of the meniscus. The assumption of a fully developed velocity profile in the analysis constitutes an approximation, whose accuracy must be considered when regions near the entrance and the flow front are analyzed. The average of the velocity is computed as,

$$\langle v_x\rangle = \frac{\int_{-h}^{h}\int_{0}^{w} v_x dydz}{\int_{-h}^{h}\int_{0}^{w} dydz} \tag{2.10}$$

$$= \frac{\frac{3}{2}\frac{dl}{dt}w\left[z|_{-h}^{h} - \frac{1}{h^2}\left.\frac{z^3}{3}\right|_{-h}^{h}\right]}{2wh} \tag{2.11}$$

$$= \frac{\frac{3}{2}\frac{dl}{dt}w\left[2h - \frac{2}{3}h\right]}{2wh} \tag{2.12}$$

leading to an average velocity equal to the advancing meniscus rate,

$$\langle v_x\rangle = \frac{dl}{dt} \tag{2.13}$$

Thus, considering that the fluid is incompressible, $m = V\rho = 2hwl\rho$, then equation 2.8 is ,

$$\frac{d(m\langle v_x\rangle)}{dt} = 2hwl\rho\frac{d^2l}{dt^2} + \frac{dl}{dt}\frac{d(2hwl\rho)}{dt} \tag{2.14}$$

$$\frac{d(m\langle v_x\rangle)}{dt} = 2hw\rho\left(l\frac{d^2l}{dt^2} + \left(\frac{dl}{dt}\right)^2\right) \tag{2.15}$$

The capillary force in the right-hand side of equation 2.7 is computed from the Young-Laplace equation (see section 2.1.2) in the differential area of the interface. The pressure in the liquid is then the Young-Laplace pressure due to the curvature minus the pressure immediately outside the interface, or vapor pressure,

$$F_{cap} = \iint \left(\Delta P_{cap} + p_0\right) dydz \tag{2.16}$$

From the schematic of Figure 2.3, the curvature radii are

$$R_1 = \frac{h}{\cos\theta} \quad ; \quad R_2 = \frac{w}{2} \tag{2.17}$$

From equation 2.3, the Young-Laplace pressure is,

$$\Delta P_{cap} = \gamma \left(\frac{\cos\theta}{h} + \frac{2}{w}\right) \tag{2.18}$$

Considering that the y-dimension is infinite, $w \to \infty$,

$$\Delta P_{cap} = \frac{\gamma \cos\theta}{h} \tag{2.19}$$

Assuming an experiment in vacuum, and neglecting the vapor pressure at normal working temperatures, the capillary force is then,

$$F_{cap} = \int_{-h}^{h} \int_{0}^{w} \frac{\gamma \cos\theta}{h} dydz \tag{2.20}$$

Note that h in the function to integrate is not a variable in z, it is a constant that defines the curvature radius (see eqn. 2.17 and Fig. 2.3). Thus, by integrating the equation 2.20,

$$F_{cap} = 2w\gamma \cos\theta \tag{2.21}$$

Under the assumption of a fully developed velocity profile (eqn. 2.9) and considering a Newtonian fluid, the viscous forces in the right-hand of equation 2.7 is computed as [55, 56],

$$F_{vis} = 2 \int_{0}^{w} \int_{0}^{l} \left(\mu \frac{dv_x}{dz}\right)_{\pm h} dxdy \tag{2.22}$$

where μ is the viscosity of the fluid. By deriving v_x from equation 2.9, and evaluating at $\pm h$ in the limit with the walls,

$$\frac{dv_x}{dz} = -\frac{3}{h}\frac{dl}{dt} \tag{2.23}$$

and replacing 2.23 in 2.22 and integrating,

$$F_{vis} = -6\mu l \frac{w}{h}\frac{dl}{dt} \tag{2.24}$$

Finally, replacing equations 2.15, 2.21 and 2.24 into the general force balance (eqn, 2.7),

$$2hw\rho\left(l\frac{d^2l}{dt^2}+\left(\frac{dl}{dt}\right)^2\right)=2w\gamma\cos\theta-6\mu l\frac{w}{h}\frac{dl}{dt} \tag{2.25}$$

By rearranging the previous equation and considering that the height of the channel is $H = 2h$, the dynamic equation of the capillary flow in infinite parallel plates is obtained,

$$\rho\left(l\frac{d^2l}{dt^2}+\left(\frac{dl}{dt}\right)^2\right)=\frac{2\gamma\cos\theta}{H}-\frac{12\mu l}{H^2}\frac{dl}{dt} \tag{2.26}$$

Viscous Regime or Washburn Regime

The viscous or Washburn regime is characterized for describing the classic dynamic motion of capillarity: an advancing meniscus with a displacement proportional to the square root of time. In this regime, the capillary flow is dominated by the capillary and viscous forces in a pseudo-steady state [51]. Here, the capillary force that pull the fluid, is balanced by the viscous dissipation from the walls. By assuming a pseudo-steady state balance, equation 2.26 leads to,

$$\frac{2\gamma\cos\theta}{H}=\frac{12\mu l}{H^2}\frac{dl}{dt} \tag{2.27}$$

Rearranging the previous equation by clearing the rate of progression of the meniscus,

$$\frac{dl}{dt}=\frac{\gamma H\cos\theta}{6\mu l} \tag{2.28}$$

Using the initial condition of $l = 0$ at $t = 0$, and integrating equation 2.28, the Lucas-Washburn equation is obtained,

$$l=\sqrt{\frac{\gamma H\cos\theta}{3\mu}}\sqrt{t} \tag{2.29}$$

It should be noticed that during the early stages of capillary filling, when $l \to 0$, equation 2.28 predicts infinite velocities. Owing this result, it follows that the Lucas-Washburn equation it is not suitable to predict the dynamics of capillary action at very short times. However, the square-root of time dynamics of the displacement of the capillary front has been found in many practical scenarios and length scale dimensions [47, 49, 58, 59] and thus can be considered as a reference point for any study of capillarity [48, 59, 60].

Inertial or Inviscid Regime

In this regime the viscosity of the fluid is ignored and the capillary flow occurs as a result of the balance between the capillary pressure and the counteracting inertial effects. This behavior was first observed by Quéré in 1997 [57] by studying the capillary rise with low viscosity fluids. This regime is attributed to the early stages of capillary filling, before the viscous dissipation has taken place. The dynamics of capillarity in this regime is characterized by a linear relation between the meniscus position and time, with a constant filling velocity [53,54,57]. In the general equation 2.26, by neglecting the viscous contribution we obtain,

$$\rho\left(l\frac{d^2l}{dt^2}+\left(\frac{dl}{dt}\right)^2\right)=\frac{2\gamma\cos\theta}{H} \tag{2.30}$$

Then, by assuming that the filling velocity is constant in this regime [50, 52, 57], the second derivative of time can be neglected, obtaining,

$$\frac{dl}{dt}=\sqrt{\frac{2\gamma\cos\theta}{\rho H}} \tag{2.31}$$

Equation 2.31 shows the theoretical constant filling velocity under the inertial regime. With the initial conditions of $l=0$ at $t=0$, the equation that describes the capillary filling during the inertial regime is obtained,

$$l=\sqrt{\frac{2\gamma\cos\theta}{\rho H}}\,t \qquad \text{or} \qquad l=A_I t \tag{2.32}$$

Transition or Visco-Intertial Regime

Between the end of the inertial regime and the beginning of the viscous regime there is a transitory stage, wherein the viscous forces and inertia combine to balance the capillary force. This transition regime, mathematically links the viscous and inertial regimes through a single transition curve. This equation was proposed by Bosanquet in 1923 [61] as a critical analysis of the Washburn equation and it is physically described by the general equation 2.26 for parallel plates,

$$\rho\left(l\frac{d^2l}{dt^2}+\left(\frac{dl}{dt}\right)^2\right)=\frac{2\gamma\cos\theta}{H}-\frac{12\mu l}{H^2}\frac{dl}{dt} \tag{2.33}$$

By defining,

$$A_I=\sqrt{\frac{2\gamma\cos\theta}{\rho H}} \qquad \text{and} \qquad B=\frac{12\mu}{\rho H^2} \tag{2.34}$$

equation 2.33 becomes,

$$\frac{d}{dt}\left(l\frac{dl}{dt}\right)+Bl\frac{dl}{dt}=A_I^2 \tag{2.35}$$

where A_I is the prefactor of the inertial equation (eqn. 2.32) and B is the viscous term. With the initial conditions of $l=0$ and $dl/dt=0$ at $t=0$, and by integrating equation 2.35 [53, 61] the transition regime equation or the Bosanquet equation is obtained,

$$l^2=\frac{2A_I^2}{B}\left[t-\frac{1}{B}\left(1-\exp(-Bt)\right)\right] \tag{2.36}$$

The Bosanquet equation at very long times, $t\to\infty$, converges to the Washburn equation (eqn. 2.29), while at very short times, $t\to 0$ converges to the inertial equation, describing the two asymptotic solutions of the Bosanquet equation [53].

2.1.5 Capillarity at the Nanoscale

The capillary action is a fundamental phenomenon with more than two hundred years of intense analysis [32]. Nowadays, with the development of nanotechnological applications and tools such as Molecular Dynamics, the study of capillarity has reached a new level of prominence, mainly due to the fact that this transport mechanism is generated fundamentally from the interatomic interactions.

Experimentally, the capillary filling of water has been studied in highly accurate silica nanochannels under the 150 nm in height [11, 49, 62–65] up to 5 nm [66]. These investigations revealed a nanoscale behavior that diverges from the macroscale, wherein the capillary filling behaves qualitatively according to Lucas-Washburn, but with lower filling velocities.

One of the properties that has been most analyzed and discussed in capillarity is the contact angle. The intense debate is related to the assumption of a constant contact angle during the capillary filling; however, experimental and theoretical studies have reported that the meniscus contact angle during capillary filling is not constant [67–70]. Furthermore, it has been shown that the contact angle depends on the filling velocity, with different proposed models [67, 70–73]. In a recent study, Wu et al. [48] systematically compared the capillary filling of various wetting liquids against the Lucas-Washburn equation modified by different dynamic contact angle models.

The scientific study in nanoscale dimensions has led to discover behaviors that differ from the classical continuum predictions. This is the case of the viscosity of fluids [74, 75], which is one of the properties affecting the classical behavior of capillary filling. Besides of the nanoconfinement effect in the viscosity [74, 75], it has been proposed that other factors may affect the viscosity in capillarity, such as the presence of bubbles [11] or electrolytes by inducing an electrical double layer [62, 76, 77]. In addition, another factor to be considered in the capillary filling is the pressure of the vapor phase or gas in front of the meniscus, which could have a significant effect in nanoscale channels [78, 79].

However, one of the most fundamental discussions in capillarity is the effectiveness of the Young-Laplace equation at the nanoscale [80,81]. Some authors have modified the Young-Laplace equation according to different conditions, such as the presence of nanobubbles or nanoparticles [82] or elastic materials [83], for example. Nonetheless, recent investigations have analyzed the applicability of the Young-Laplace equation in the nanoscale with implications related to the curvature effects on the surface tension [42, 80, 81], showing very good agreement with the Young-Laplace equation.

In Chapter 4 of the present thesis, an atomistic study of water capillarity in silica nanochannels is reported [84]. The scope of this investigation is to study the early stages of water imbibition at different air pressures.

2.2 Termophoresis

Thermophoresis is the phenomenon wherein particles experience a net drift induced by a thermal gradient. It is understood as consequence of a thermally rectified Brownian motion [85], where molecules in the hotter region of the media collide with a solid particle, transferring a greater momentum as compared to the molecules in the colder regions. Tyndall in 1870 was the first who observed and described this phenomenon [86]. He noted how aerosol particles in a room full of dust were driven away from a heat surface, however, without mentioning the molecular origin of this phenomenon.

2.2.1 Brownian Motion

Back in 1718, Newton already hypothesized the molecular or atomic origin of things by analyzing the capillary action on his book *Opticks* [33]. In the Query 31 he stated: *There are therefore Agents in Nature able to make the Particles of Bodies stick together by very strong Attractions. And it is the business of experimental Philosophy to find them out.* The next important step forward to describe the presence of molecules or atoms was made by Robert Brown almost a century after, in 1828 [87]. He observed that pollen particles suspended in water appeared to be in constant and chaotic movement. He stated that this motion was not produced by light or high temperature and that never slowed down or stopped. By observing the same behavior with other types of particles and fluids, Brown stated that this is a general physical phenomena [88].

Deepening into Brown's work, Einstein in 1905 [89] and Smoluchowski in 1906 [90] independently suggested that the motion of the particles was produced by the incessant collisions between the molecules of the fluid (atoms) and the solid particle, which generates an endless motion of the particle. This is how today the random motion of a particle in a fluid medium is known as Brownian motion.

2.2.2 Thermophoresis as a Rectified Brownian Motion

From the Einstein's investigation of Brownian motion [89], the isothermal dispersion coefficient for fluid is,

$$D_0 = \frac{k_b T}{6\pi R\mu} \tag{2.37}$$

where k_b is the Boltzmann constant, T the temperature of the fluid, R the radius of the particle and μ the viscosity of the fluid. From equation 2.37, it can be inferred that while the temperature is increased, the dispersion of the particles also increases. Therefore, if a thermal gradient is imposed in the fluid, the particles in the hot region will have a higher dispersion compared to the cold region. The net effect of the differential dispersion results in a net migration of the particles from the hotter regions to the colder regions. This means that under a thermal gradient, the particles will travel against the gradient of temperature, where the average motion of the particles is known as thermophoresis.

From a molecular point of view, the thermophoretic motion is generated by the momentum transfer from the molecules in the fluid to the solid particle, where molecules in the high temperature zone have higher kinetic energy compared to the low temperature zone. Therefore, the momentum transfer in the hot side of the solid particle overcomes the momentum transfer from the cold side, generating a net motion towards the cold side. The general definition of thermophoresis is derived from different studies, with different combinations of phases involved (gas-solid or liquid-solid for example), which are summarized in the following.

2.2.3 Thermophoresis in gases

The first studies of thermophoresis were performed in a gas medium, due to the inherently higher kinetic energy compared to other phases. This higher kinetic energy allows a higher momentum transfer from the gas phase to a solid particle, enabling the macroscopic observation of this phenomenon. The collision rate is quantified by the Knudsen number, Kn= λ/L, where λ is the mean free path (average distance traveled by a moving particle) and L is the representative physical length scale of the solid, e.g. the radius for a sphere.

James C. Maxwell, in 1879 [91] studied the momentum transfer of molecules in rarefied gases in a system with inhomogeneous temperature. Later, with the attempt to apply these concepts in the computation of the forces involved in a radiometer, Epstein in 1929 derived the first expression for the thermophoretic force [92]. Epstein obtained an equation to describe the forces exerted on spherical particles produced by a gas medium under a temperature gradient. This approach is valid in a continuum flow regime of gas-particle interactions characterized by very small Knudsen numbers (Kn ≤ 0.1) [85, 93, 94]. The equations for the thermophoretic velocity and force are,

$$v_{tp} = -\frac{3}{2}\left(\frac{k_g}{2k_g + k_p}\right)\frac{\mu}{\rho}\frac{\nabla T}{T} \tag{2.38}$$

$$F_{tp} = -9\pi R\left(\frac{k_g}{2k_g + k_p}\right)\frac{\mu^2}{\rho}\frac{\nabla T}{T} \tag{2.39}$$

where k_g y k_p are the thermal conductivities of the gas and the particle, respectively, μ the viscosity of the fluid and ρ the gas density. Epstein's equation is in good agreement with experimental results for particles with low thermal conductivity but underestimates the force in particles of high thermal conductivity [94, 95]. Therefore, Brock [96] and later Talbot et al. [94] developed a more detailed analytical work for a wider range of thermal conductivities, but in the same appropriate continuum regime (Kn < 0.1). In 1965, Derjaguin and Yamalov [97] determined the thermophoretic velocity in a gas medium by using irreversible thermodynamic and Onsager principle. They obtained an equation similar to the one proposed by Brock [96], but including the effects of temperature slippage in the fluid-particle interface.

These studies lay the foundations of the thermophoretic theory, allowing the extended analysis of this phenomenon. More recently, in 2004, Zhigang Li and Hai Wang developed a gas-kinetic theory to describe the thermophoresis of solid particles in gases [98], with important implications in nanoscale studies [98–101].

2.2.4 Thermophoresis in liquids

Several experimental works of thermophoresis in gases have been performed in the literature, whereas the experiments performed in liquids are very few [85]. This is mainly due to the fact that the mean free path of a liquid is much lower than gases and the average speed of gases is much higher than in liquids. Therefore, the thermophoretic force in liquids will be lower in comparison to system in a gas phase under similar conditions.

The first investigation of thermophoresis in liquids was made by McNab and Meisen in 1973 [93]. They used latex spheres of 0.79 μm and 1.01 μm, in water and n-hexane, leading to Knudsen numbers less than 7×10^{-4}. The experimental results of their work showed that the thermophoretic process is significantly slower in liquids than in gases, while the Epstein's equation overestimates the thermophoretic velocity by 17%. They proposed an equation of the thermophoretic velocity in liquids inspired by the work of Epstein [92] and Derjaguin [97],

$$v_{tp} = -0.26\frac{k_l}{2k_l + k_p}\frac{\mu}{\rho T}\nabla T \tag{2.40}$$

Nowadays, with the development of highly accurate computational tools and a new generation of accurate measuring equipment, the thermophoretic phenomena in liquids has attracted considerable attention. Han in 2004 [102] with molecular dynamics simulations showed that the temperature gradient applied to a nonconducting liquid induces a pressure gradient tangential to

the particle surface. Michaelides in 2015 [85] performed Monte Carlo simulations to determine that the thermophoretic velocity is proportional to the viscosity of the fluids and to the imposed thermal gradient, in line with McNab and Meisen results [93]. In addition, motivated for the potential applications of nanofluid solutions, this phenomenon has also been studied in dispersions of nanoscale particles immersed in liquids. For example, Martin y Bou-Ali [103] showed that the thermophoretic effect is significant in solutions of fullerene in toluene. Based on the work of McNab and Meisen, Buongiorno [104] showed that thermophoresis may cause the redistribution of nanoparticles in liquid laminar boundary sublayers, while Haddad et al. [105] demonstrated the heat transfer of nanofluids is increased by the thermophoresis.

2.2.5 Thermophoresis in solids

A couple of decades ago, studying the successive Brownian collisions between two solid phases and quantifying the momentum transfer between them would have been an impossible task, therefore analyzing thermophoresis in solid phases was not a topic of interest for the scientific community. Nowadays, owing to the nanotechnological revolution and the rise of computational tools like Molecular Dynamics, the thermophoresis in solids has become a topic of considerable scientific and technological interest. However, since this topic has been developing for less than a decade, a comprehensive understanding of the fundamentals of thermophoresis in solids has not yet been achieved.

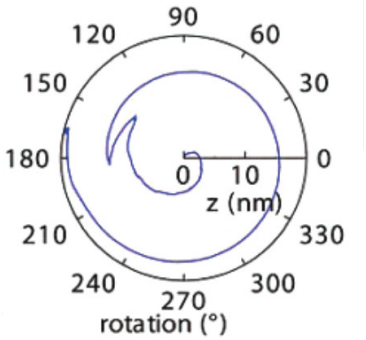

Figure 2.4: The trajectory of a gold tracer atom located in the outermost gold shell of the nanoparticle during the thermophoretic motion inside the carbon nanotube (Reprinted from ref. [106]).

The first investigation of thermophoresis in solids was performed by Schoen et al. in 2006 [106]. In this work, Molecular Dynamics simulations were conducted to study the thermophoretic transport of gold nanoparticles inside carbon nanotubes. They observed that the force acting on the particle increases with the applied thermal gradient while the motion of the nanoparticle follows the threadlines of the carbon nanotubes with a helical motion (see fig 2.4). Then in 2008, Zambrano et al. [20] performed an investigation of the thermophoretic motion of water nanodroplets confined in carbon nanotubes. In this case, the momentum transfer is from the solid to the liquid, the opposite case of the thermophoresis in liquids where the collision of the water molecules produces the motion in a solid body. Zambrano and co-workers shown that the water droplets can be transported inside carbon nanotubes and the force applied is proportional to the imposed thermal gradient, in line with Schoen et al. [106]

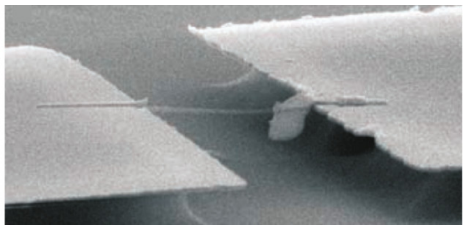

Figure 2.5: Scanning electron microscope (SEM) image of the device fabricated by Barreiro et al. [107] Here, a gold cargo is attached to the carbon nanotube between two silica plates. (Reprinted from ref. [107])

The thermophoretic motion in solids was observed experimentally in the work of Barreiro et al. in 2008 [107]. In this investigation, two silica plates were joined by a carbon nanotube, and on top of this nanotube, a cargo was placed, as shown in Figure 2.5. They observed that the cargo was driven by the thermal gradient towards the cold side.

Due to the great interest of graphene-based technologies in the last years, the thermophoretic motion of solid bodies supported on graphene has also been studied, but only theoretically. Becton and Wang in 2014 [108] with Molecular Dynamics showed that a graphene nanoflake supported on a graphene substrate can be transported by imposing a thermal gradient, displaying a motion towards the cold side. Similarly, Panizon and co-workers noticed in 2017 [109] that a gold nanoparticle supported on graphene is also transported with an imposed thermal gradient. Interestingly, they observed that this motion is proportional to the temperature difference (ΔT), but independent of the length and thus, of the thermal gradient. They state that the phoretic force is due to the flexural phonons, whose flow is known to be ballistic and distance-independent up to relatively long mean-free paths.

Nowadays, it is accepted that the thermophoretic motion in solids is originated by the phonon current in the interface [110, 111]. In 2007, Schoen and co-coworkers measured the phonon dispersion or the correlated lattice vibrations, showing that the thermophoretic motion of gold nanoparticles correlates with the phonon dispersion exhibited by a standard carbon nanotube. In other investigation, Prasad and Bhattacharya in 2016 [111] stated that the thermophoretic motion in coaxial CNTs is initiated by the longitudinal acoustic phonon scattering mechanism, while Panizon and co-workers, stated that the flexural phonons are the responsible for thermophoretic mechanism of gold nanoparticles on graphene, rather than the harmonic phonons [109].

2.3 Brownian Ratchet

Atoms and molecules move constantly under thermal fluctuations by default, and the idea to obtain useful work from those fluctuations can be traced back to the origins of the study of the atom. The Brownian ratchet is a concept that describes a molecular scale motor capable to produce useful work by taking advantage of the random fluctuation of atoms or molecules, with the restriction of the second law of thermodynamics. This concept born as a thought experiment proposed by Smoluchowski in a conference talk in Münster, 1912 [25,112], and later extended by Feynman on his famous Lectures on Physics [113].

2.3.1 Smoluchowski-Feynman Ratchet

The Smoluchowski-Feynman ratchet device consists of an axle with paddles and a ratchet system at the respective ends, as shown in Figure 2.6. The ratchet (left side) consists of a circular gear with uniform but asymmetrical teeth and a pawl, allowing the rotation of the gear in one direction and in the other brakes it. Thus, if the whole device is surrounded by a gas at thermal equilibrium, the molecules of the gas will impact the paddles randomly, performing a rotatory Brownian motion on it. The pawl, therefore, will admit the gear to proceed into one direction ("forward") but practically exclude the rotation to the opposite direction ("backward"). In general, the gadget will produce on the average a systematic rotation in one direction only, thus allowing a load placed in the center to be lifted.

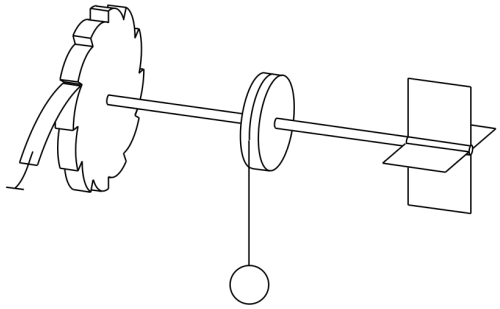

Figure 2.6: Smoluchowski-Feynman ratchet. The microscpocic device consist of a ratchet (left end), a load (center) and a paddle (right end). This gadget uses the random fluctuations of the atoms to perform a useful work (Reprinted from ref. [25]).

However, the Brownian ratchet concept of Figure 2.6 is not accurate. By considering thermal equilibrium, the gadget represents a perpetuum mobile of the second kind, also referred to as a Maxwell demon, would violating the second law of thermodynamics [114]. The misconception lies in assuming the operation of the pawl and its associated work, which is in indeed very similar to Maxwell's demon. Since the impacts of the gas molecules take place on the nanometer scale, the pawl has to be extremely small and smooth, in order to admit even a rotation in the allowed direction [115]. As Smoluchowski mentioned, the pawl itself is subject to non-negligible thermal fluctuations, which would eventually allow the pawl to be lifted and the gear will freely rotate even in the non-permitted direction.

Feynman, aware of the lack of accuracy in the Smoluchowski thought experiment, extended the ratchet concept on his Lectures on Physics in 1966. Feynman describes the same device proposed by Smoluchowski, but considering that the paddles and ratchet are at different temperatures, thus producing different collision ratios of the gas molecules on the device. In order to produce a useful work, without violate the second law of thermodynamics, Feynman proposed that the temperature of the paddle T_1 must be higher than temperature of the ratchet T_2 [113, 116, 117]. His calculation indicates that work can indeed be extracted considering these two asymmetries (the pawl and the thermal difference), reaching in fact Carnot efficiency. However, it was noted later by Parrondo and Español that the axle is indeed connecting the two reservoirs thermally, therefore, the engine will never achieve Carnot efficiency [117].

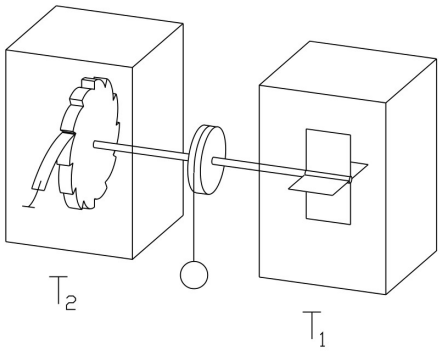

Figure 2.7: Feynman ratchet. Gadget proposed by Feynman inspired in the Smoluchowski concept, without violating the second law of thermodynamics (Reprinted from ref. [25]).

2.3.2 Brownian Ratchet Applications

The Brownian ratchet is a fundamental concept in the engineered transport of materials at the nano/micro scale. Based in the Smoluchowski-Feynman ratchet concept, in order to perform a useful work from the Brownian motion, two conditions need to be satisfied: (i) the breaking of spatial symmetry and (ii) the breaking of thermal equilibrium [25, 118]. In the quest to create applications that meet these conditions, it has been shown that the concept has already been applied in nature. For example, Peskin and co-workers [119] showed that chemical reactions generate protrusive forces by rectifying Brownian motion, driving a large number of intracellular forces. Similarly, it has been shown that plasmids evidence cargo transport by a ratchet mechanism [10, 120], and that interstitial collagenase is a Brownian ratchet that is able to rectify Brownian forces into a propulsion mechanism by coupling to collagen proteolysis [121].

Inspired by the ratchet mechanism, several applications have been developed both experimental and theoretically. A complete review of artificial Brownian ratchets until 2009 was collected by Hänggi and Marchesoni [122]. Notably, the work of Bader and co-workers is highlighted, who in 1999 fabricated a Brownian ratchet device that is capable of transporting small DNA molecules in aqueous solution [123]. In the same year, Van Oudenaarden et al. [124] fabricated a geometrical Brownian ratchet by using a two-dimensional fluid lipid bilayer membrane on a patterned solid support, causing a directional transport of molecules.

Theoretically, Tu and Hu [118] conceptually design a molecular motor from DWNT driven by varying electrical voltage. For fluid transport, John and co-workers [125] presented a 'wettability ratchets' based on two-layer thin film model that can be employed to transport a continuous system (see Figure 2.8).

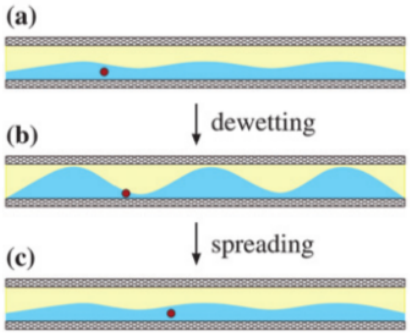

Figure 2.8: Sketch illustrating the working principle of a fluidic ratchet based on a switchable wettability profile that causes dewetting-spreading cycles (Reprinted from ref. [125]). Two immiscible liquids are confined between two parallel plates. At equilibrium (a), a flat interface between the two liquids is presented. Then, by switching the electric field (b) the films evolve into a set of drops because the interface is destabilized by the overall electric field and its local gradients. After switching the electric field again (c), the drops spread until reaching the homogeneous two-layer state. In this process, a net motion of the fluids is observed as depicted by the tracking red particle.

Chapter 3

Molecular Modeling

Molecular modeling is the branch of science that studies the molecular structure and its functioning by means of mathematical models and computational tools [126]. Here, molecules are represented as mechanical systems in which particles (atoms) are connected by strings (bonds). Thus, molecules can rotate, vibrate and move in a defined space to achieve favorable conformations as a consequence of the collective response of the intra and intermolecular interactions acting on each particle.

In the framework of molecular simulations, several methods can be found, but the most used in research are the *ab initio* methods, Semi-empirical quantum chemistry methods, Monte Carlo, Molecular Dynamics and Free Energy calculation methods. Each method is based on the resolution of a main mathematical model. For example, the *ab initio* methods solve different approximations of the Schrödinger differential equation without depending on fitted parameters whereas Molecular Dynamics simulations solves the Newton's equations of motion [127].

In this chapter, the main concepts of molecular modeling, such as Force Fields and the molecular dynamics technique are provided, which will introduce the main concepts of the methodology of this thesis. For further details, the reader is referred to text books given by Schlick [128], Leach [126] and Frenkel & Smit [129].

3.1 Molecular Mechanics

In fundamental chemistry, the atomic interactions are mathematically described by the Schrödinger equation. However, due to the stochastic and complex nature of this equation, analytic solutions are only known for special cases (e.g. hydrogen atom or free particle). In fact, numerical solutions of the Schrödinger equation rely on model approximations such as the Born–Oppenheimer approximation, which, because of the large mass difference between electrons and the nucleus, says that the position of the electron adapts instantaneously to the nucleus position. Still, the computational cost of these methods is considerably high, allowing the study of systems containing only a few hundred of atoms and time scales in the order of picoseconds. For a detailed introduction in Quantum Mechanics, the reader is referred to Quantum Chemistry books [130].

In the basis of the Born–Oppenheimer approximation, the Force Field methods ignore the individual and collective motion of the electrons and solve the energy of the system as a function of the position of the atoms only. Because of this, Force Field based methods, like Monte Carlo or Molecular Dynamics, compute large systems in a fraction of the computer time required for Quantum Mechanics [126].

In general, to describe the Molecular Mechanics of a system, the Potential Energy is computed from position-dependent functions based in empirical parameters, such as the van der Waals or Coulombic intermolecular interactions. These and others empirical Force Fields are described in the following.

3.1.1 Force Field for Molecular Mechanics

Force Field methods mathematically describe the potential energy of a system consisting of particles. In molecular mechanics, each particle is considered as a mass point atom. The general Force Field used in Molecular Modeling can be classified in terms of four components of intra and intermolecular forces within a system. Thereby, the energy changes occur with the deviation of the molecular bonds and angles respect to equilibrium values, and the non-bonding interactions between the relative position of the particles. The basic functional form of Molecular Mechanics is,

$$U(r^N) = \sum E_{bonds} + \sum E_{angles} + \sum E_{torsion} + \sum E_{non-bonding} \tag{3.1}$$

where $U(r^N)$ is the potential energy, which is a function of the position, r, of the N particles in the system. The first three terms, called bonding interaction, describe the intramolecular interaction of a molecule, and the fourth term, called the non-bonding, describe the intermolecular interactions.

The first term of Equation 3.1 describe the interaction energy between pairs of bonded atoms, based on the approach or stretching of the two atoms. The second term represent the energy obtained by the bending of the valence angles in the molecules, between three adjacent atoms. The third term is the torsion potential, which describe the energy of the rotation of a molecule consisting of four consecutive atoms. The final term represents the contribution of the non-bonding interactions between all the pairs of atoms in the system. In a simple force field, this last term is described by the Coulomb interaction for the electrostatic and the Lennard-Jones potential for the van der Waals interactions and steric repulsion. In the following, the most commonly used potentials are described.

Intramolecular or Bonding Potentials

Intramolecular potentials are empirical functions that describe the internal dynamics of the molecules, representing the electronic cloud behavior of the atoms and the repulsive forces at very short distances. The bond stretching potential is based in the dependency of the energy on the length of the bond, with respect to a reference value. One of the functional form is the Morse potential,

$$U(l) = D_e[1 - \exp[-a(l - l_0)]]^2 \tag{3.2}$$

where l is the time-dependent length of the bond and l_0 is the reference bond length, while D_e is the depth of the potential energy minimum and a is a constant with dependency on the vibrational frequency of the bond. The Morse curve describes a wide range of behavior from the strong equilibrium to dissociation. A simpler but widely used potential, due to the efficient computation, is the harmonic potential or Hooke's Law formula, in which the energy varies parabolically from a reference value l_0,

$$U(l) = \frac{k}{2}(l - l_0)^2 \tag{3.3}$$

where k is the stretching bond constant.

The angle bending potential is commonly described using the Hooke's law or harmonic potential, as well,

$$U(\theta_{bend}) = \frac{k}{2}(\theta_{bend} - \theta_{bend,0})^2 \tag{3.4}$$

The contribution of each bond is characterized by a force constant k and a reference angle value $\theta_{bend,0}$, which can be found in the literature [131, 132]. The stretching bond and bending angle are considered as hard degrees of freedom, which requires a large amount of energy to cause a significant deformation from the reference value. Thereby, the main variations in the structure and the relative energies are due to a complex relation between the torsional and non-bonding interactions.

The torsion potentials describe the energy changes in terms of the rotation of the bond between four consecutive atoms. However, force fields with torsion potentials are not widely used in the literature, in turn, a non-bonding interaction between the atoms at the extremes is sometimes introduced to obtain the desired energy function. Nevertheless, usually the force field used for organic molecules or graphite-based structures use explicit torsion potential with a contribution every four atoms (i.e. quartet of bonded atoms) in the system. One expression has the form,

$$U(\omega) = \sum_{n=1}^{N} \frac{V_n}{2}[1 + \cos(n\omega - \varphi)] \tag{3.5}$$

where ω is the torsion angle, φ is the phase factor which determines where the torsion angle passes through its minimum value and V_n is a force constant for each molecule.

The intramolecular potentials described in this section are widely used in molecular modeling. However, there are more complex potentials or *Cross-terms* potentials that can combine two or more intramolecular potentials to describe the dynamic of a molecule under study. For further information about intramolecular potentials the reader is referred to the literature [126, 127].

Non-bonding or Intermolecular Potentials

Intermolecular potentials are empirical energy functions in terms of the separation between the nuclei of the particles. In terms of quantum mechanics, the non-bonding interactions are electrostatic, including ionic molecules, polar molecules, and even non-polar molecules whose interaction is produced by the instantaneous dipoles induced from the incessant dynamics of the electronic clouds of the atoms. This last interaction is known as the London forces or dispersion forces and is classified within the van der Waals forces with the decay of r^{-6} of the energy interaction. The quantum mechanics computation of these forces is actually far from trivial, requiring electron correlation and very large basis sets [127]. For this reason, simple empirical expressions are required to describe the Molecular Mechanics of a system, such as the Coulomb forces, van der Waals forces and the repulsive forces, which we will review in the following. For a detailed introduction of the intermolecular forces, the reader is referred to the literature [37].

The electrostatic interaction between two point charges q is calculated according to the Coulomb's law,

$$U(r_{ij}) = \frac{q_i q_j}{4\pi\varepsilon_0 r_{ij}} \tag{3.6}$$

where ε_0 is the vacuum permittivity and the partial atomic charges q are separated with a distance r_{ij}. The *partial atomic charges* or *point charges* concepts refers to the charge magnitude restricted to the nuclear centers of the atoms, if not stated otherwise. This potential is used to describe the interaction between molecules with a net charge, between different parts of the same molecule or solutions with ions. Moreover, molecules with permanent dipoles are often characterized with partial charges within the molecules and its electrostatic is computed with this potential.

Totally neutral molecules, such as molecular argon or carbon dioxide, interact each other through the van der Waals forces. These forces are called in honor of the scientific Johannes Diderik van der Waals who quantified the deviation of rare gas from the ideal gas behavior. In general, the van der Waals forces consists of two terms, the attractive term and the repulsive term. The attractive term represents the dispersion forces or London forces, which describe the attractive interaction from the instantaneous dipoles induced from the fluctuations of the electronic clouds. London in 1930, using quantum mechanical perturbation theory, derived a r^{-6} distance dependence expression for the dispersion interaction energy between two identical atoms. The repulsive term describes the steric repulsion, sometimes called repulsive forces or exchange forces, at very short distances between the atoms. This interaction is understood as a repulsion of the neutral atoms due to overlapping of the electron orbitals. It is based in the Pauli exclusion principle, which formally prohibits any two fermions (electrons) in a system from having the same set of quantum numbers. The origin of the steric repulsion is quantum mechanics and unfortunately there is not a general equation for describing their distance dependence.

The most commonly used potential to describe the repulsive and attractive interactions between neutral atoms is the Lennard-Jones potential,

$$U(r_{ij}) = 4\varepsilon \left[\left(\frac{\sigma}{r_{ij}} \right)^{12} - \left(\frac{\sigma}{r_{ij}} \right)^{6} \right] \tag{3.7}$$

where σ is the collision diameter and ε is the well depth. In this potential the r^{-12} represent the steric repulsion of the atoms and the r^{-6} term represent the attractive forces mentioned above. The parameters σ and ε can be obtained from *ab initio* calculations or through fitting to experimental data. For complex multi-atomic systems, the Lennard-Jones parameters are usually obtained from the Lorentz-Berthelot mixing rules from the individual species,

$$\sigma_{AB} = \frac{1}{2}\left(\sigma_{AA} + \sigma_{BB}\right) \tag{3.8}$$

$$\varepsilon_{AB} = \sqrt{\varepsilon_{AA}\varepsilon_{BB}} \tag{3.9}$$

The obtained parameters from this method must be studied and analyzed for a justified utilization. For the Lennard Jones potential, there are no strong justification in favor of the repulsive r^{-12} term, besides the computational convenience [126, 127]. For example, quantum mechanics calculations suggest an exponential form in the repulsive term (from the analytical

solution of the Schrödinger equation for hydrogen). Therefore, there is some justification to use an exponential function in the repulsive term, which is found in the Buckingham potential,

$$U(r_{ij}) = A\exp(-Br) - \frac{C}{r_{ij}^6} \tag{3.10}$$

where A, B and C are fitting parameters. However, this potential has a problem at very short interatomic distances where the potential becomes strongly attractive. As r goes toward zero, the exponential becomes a constant while the r^{-6} term goes toward $-\infty$. This behavior could lead to nuclear fusion, therefore special precautions must be taken in the computation with this potential.

Combination of these intra- and intermolecular potential leads to several models used in molecular modeling. Among them we found the commonly used water models like SPC/E [133] and TIP3P or TIP4P models [134], or the Born-Huggins-Mayer potential for alkali halides [135].

3.2 Molecular Dynamics

Molecular Dynamics (MD) is a computational method that solves the dynamics of a particle system by integrating the Newton's equations of motion. It can be compared with a billiard game where the balls collide with each other, acquiring new positions as time progresses. Molecular dynamics is a deterministic method wherein the state of the system at any future time can be predicted from its current state. From time averages, different thermodynamic or mechanical properties can be calculated. This method was introduced by Alder and Wainwright in 1957 [136, 137] and since then has rapidly evolved along with the advances in computing.

In this method, atoms are represented as mass points which interact through force fields. Therefore, the selected force fields determine the motion of the atoms based on classical mechanics. According to the Newton's equations of motion,

$$m_i \frac{d^2\mathbf{r}_i(t)}{dt^2} = \mathbf{f}_i(t) \tag{3.11}$$

the position $\mathbf{r}_i$ of the i particle is updated in time according to the forces $\mathbf{f}_i$ acting on the particle. From classical mechanics, the forces are required to be conservative [138]. Conservative forces are defined as vector quantities that are derivable from a scalar function $U(r_1, ..., r_N)$ of N particles, called the potential energy function, thus,

$$\mathbf{f}_i(r_1, ..., r_N) = -\nabla U(r_1, ..., r_N) \tag{3.12}$$

where the force acting on the i particle, $\mathbf{f}_i$, depends on the potential energy interaction with every j particle of the entire N particle system, relatively to the i particle position,

$$\mathbf{f}_i = -\sum_{j\neq i}^{N} \frac{\partial U(r_{ij})}{\partial r_{ij}} \frac{\mathbf{r}_{ij}}{r_{ij}} \tag{3.13}$$

where $\mathbf{r}_{ij} = \mathbf{r}_j - \mathbf{r}_i$ and $r_{ij} = |\mathbf{r}_{ij}|$. In this way, a molecular dynamic simulation generates successive positions of the particles in a system through a time discretization of equation 3.11,

where the forces acting on every particle are computed from the gradient of empirical potential functions, such as the Coulomb or Lennard-Jones potentials.

In this thesis, the molecular dynamic package FASTTUBE [139] is used to integrate the equations of motion and to investigate molecular systems. This package was developed in ETH, Zurich, written in FORTRAN, and has been used extensively in nanofluidic applications [17, 20, 106]. In the next sections, additional computational details to perform a molecular dynamics simulation will be provided, such as the finite difference methods to integrate the Newton's equations of motion, boundary periodic conditions, or the thermostats to maintain the temperature of the system at a desired value.

3.2.1 Finite difference methods

In order to compute the positions of the particles in time, the Newton's equation of motion must be integrated according to a discretization in time. The main idea is that the integration is broken down into small stages, each one separated in time by a fixed time step δt. The total force on each particle in the system at time t is calculated from equation 3.13. From the forces we can determine the accelerations of the particles, which are then combined with the positions and velocities at a time t to calculate the positions and velocities at a time $t + \delta t$, under the assumption that these forces and velocities are constant for the small time step δt.

The basic algorithm for integrating the equations of motion is the Taylor series expansion,

$$\mathbf{r}(t+\delta t) = \mathbf{r}(t) + \delta t\mathbf{v}(t) + \frac{1}{2}\delta t^2\mathbf{a}(t) + \frac{1}{6}\delta^3 t\mathbf{b}(t) + ... \tag{3.14}$$

$$\mathbf{v}(t+\delta t) = \mathbf{v}(t) + \delta t\mathbf{a}(t) + \frac{1}{2}\delta t^2\mathbf{b}(t) + ... \tag{3.15}$$

$$\mathbf{a}(t+\delta t) = \mathbf{a}(t) + \delta t\mathbf{b}(t) + ... \tag{3.16}$$

where, $\mathbf{v}$ is the velocity (the first derivative of the position in time) and $\mathbf{a}$ is the acceleration (the second derivative) and $\mathbf{b}$ is the third derivative. The Verlet algorithm, the most widely used method in MD, uses the position at time t and from the previous step at $t - \delta t$, to calculate the new positions at $t + \delta t$. According to the Verlet algorithm, the position in the new step is calculated as,

$$\mathbf{r}(t+\delta t) = 2\mathbf{r}(t) - \mathbf{r}(t-\delta t) + \delta t^2\mathbf{a}(t) \tag{3.17}$$

This algorithm does not explicitly compute the velocities, nevertheless, these can be computed from the difference of the positions between the previous and the calculated next step,

$$\mathbf{v}(t) = [\mathbf{r}(t+\delta t) - \mathbf{r}(t-\delta t)]/2\delta t \tag{3.18}$$

The local error of this algorithm is in the order of $\mathcal{O}(t^4)$ for the position. Another commonly used algorithm in molecular dynamics is the *Leap-Frog* algorithm, with a half-step $t + \frac{1}{2}\delta t$ in velocity, which use the following relations,

$$\mathbf{v}(t+\frac{1}{2}\delta t) = \mathbf{v}(t-\frac{1}{2}\delta t) + \delta t\mathbf{a}(t) \tag{3.19}$$

$$\mathbf{r}(t+\delta t) = \mathbf{r}(t) + \delta t\mathbf{v}(t+\frac{1}{2}\delta t) \tag{3.20}$$

To implement this algorithm, the velocities at the half-step $t + \frac{1}{2}\delta t$ are first computed from the velocities at $t - \frac{1}{2}\delta t$ and the accelerations at time t. The positions at the new step $t + \delta t$ are then obtained from the velocities just calculated together with the position at the present step. In order to compute physical properties that depend on the velocity at time t, the velocities can be calculated as,

$$\mathbf{v}(t) = \frac{1}{2}\left[\mathbf{v}(t + \frac{1}{2}\delta t) + \mathbf{v}(t - \frac{1}{2}\delta t)\right] \tag{3.21}$$

The local error of this algorithm is in the order of $\mathcal{O}(t^3)$ for the position and velocity. This method has the advantage over the Verlet algorithm that explicitly includes the velocities and does not require the calculation of the differences of large numbers, like the positions in equation 3.17. Other algorithms of interest, like the *Velocity Verlet* algorithm, are explained in detail in the literature [126, 129].

3.2.2 Periodic Boundary Conditions

The periodic boundary conditions allow a particle system to be extended or replicated in space, enabling for example, that all the particles in a system experience forces as if they were part of the bulk of a fluid. This method also allows the study of a continuous mass transport in space, for example, a pressure driven flow along one dimension in a Cartesian coordinate system. In Figure 3.1 a bidimensional example is depicted. Here, each box is surrounded by eight exactly equal boxes, where the central box is the original computational box and the others are copies called *images*. During the simulation, only the properties of the original simulation box need to be recorded and propagated.

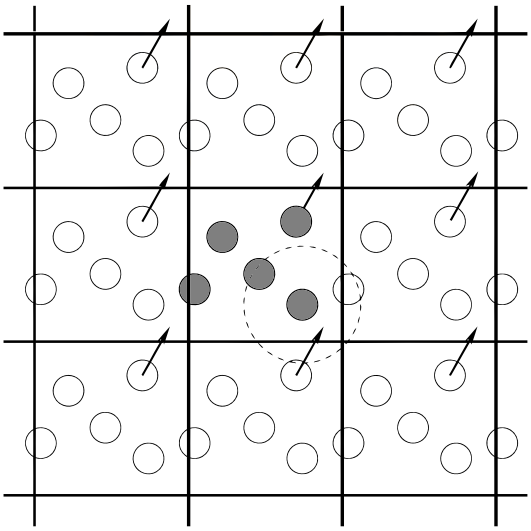

Figure 3.1: Bidimensional representation of the periodic boundary condition (Reprinted from ref. [140]).

As long as the potential is not long-range interaction, the *minimum-image* convention is adopted, in which each individual particle in the simulation interacts with the nearest image or particle in the periodic array. With this technique, if a particle passes through one side of

the unit cell during the simulation, this particle re-appears on the opposite side with the same velocity. This technique is commonly used to compute thermodynamics properties such as the diffusion or surface tension in liquids. However, special precautions must be taken when long-range interactions are implemented, which requires constraints to not induce spurious effects in the computation [127, 141, 142]. Furthermore, in simulations of solid systems, the strain field generated from any inhomogeneity in the system will be artificially truncated and modified by the periodic boundary [143]. Similarly, to study shock waves and phonons in a molecular dynamic simulation the system is limited by the box size.

3.2.3 Neighbor List and Cut-off Radius

As can be inferred from equation 3.13, the computation of the interatomic forces in a molecular dynamic simulation requires a large number of pairwise calculations, involving every interaction between each i atom with every j atom in the system to estimate the separation distance r_{ij} and the energy $U(r_{ij})$, problem known as the *N-body problem*. In order to reduce the computational cost, some consideration can be made with special precaution and justification.

Considering the short-range interactions, there is a minimum distance where the interaction energy becomes negligible. This distance is known as the *cut-off* radius, r_{cut}, and can be assumed that particles with a separation distance greater than the cut-off radius, $r_{ij} > r_{cut}$, do not interact. In this case, the program does not perform the force computation, thus avoiding an increase in the computational cost, and jumping to the next j particle. However, in order to test if this criterion is accomplished, the program must still compute all the pairwise distances in the system. The time to list all the pairs of separations is proportional to the number of distinct pairs in the system, with $\frac{1}{2}N(N-1)$ pairs in a $N-$particle system [140]. These calculations still consume a lot of computational time. In order to reduce the computational costs associated in listing particles, Verlet in 1967 implemented a neighbor list to speed up the computational time on the simulations [144], today known as the Verlet list. This technique consists of creating a list of all particles within a given list-radius r_{list} distance, which must be larger than the cut-off radius, $r_{list} > r_{cut}$, for each particle in the system (see Figure 3.2). According to this technique, the interaction forces are computed for the listed particles exclusively, and the list is updated every time step or between certain established integration steps.

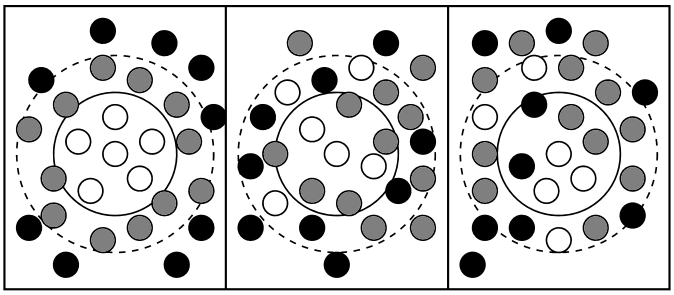

Figure 3.2: Bidimensional representation of the Verlet list. The solid line represents the cut-off radius r_{cut} and the dashed line the list-radius r_{list}, within the particles are listed (Reprinted from ref. [140]).

Another commonly used technique is the *Cell-List* [140]. This list consists of subdividing the computational box into three-dimensional cells with a length larger than the cut-off radius.

Thereby, the particles are sorted into each cell and the force is computed between particles in the same cell and the nearest cells only.

Cut-off Radius for Electrostatics

Special precautions must be taken when long-range interactions are involved and a truncation at some cut-off distance radius is implemented. Truncating the interaction by using a cut-off distance gives rise to discontinuous energies and forces, unrealistic equilibration times [145] and has some rather unfortunate consequences resulting in non-physical distributions of the solvent molecules near the cutoff distance [127]. *Switching* and *shifting* functions have been proposed to solve the mentioned spurious effects in the simulations [127, 145, 146]. A switching function gradually reduce the Coulomb interaction to zero over a range of a few angstroms near the r_{cut} limit, by defining two different radii. Whereas a shifting function modify the potential for all the r_{ij} distances less than the cut-off radius. A comparison between these two truncations is shown in Figure 3.3. In the simulations presented in this thesis, a truncation shift function is implemented for the calculation of the electrostatic interactions, which has the form,

$$\begin{aligned} S(r_{ij}) &= \left(1 - \frac{r_{ij}}{r_{cut}}\right)^2 \quad \text{for} \quad r_{ij} < r_{cut} \\ &= 0 \quad \text{for} \quad r_{ij} \geq r_{cut} \end{aligned} \tag{3.22}$$

where the general form of the Coulomb potential now is,

$$U(r_{ij}) = \frac{q_i q_j}{4\pi\varepsilon_0 r_{ij}} S(r_{ij}) \tag{3.23}$$

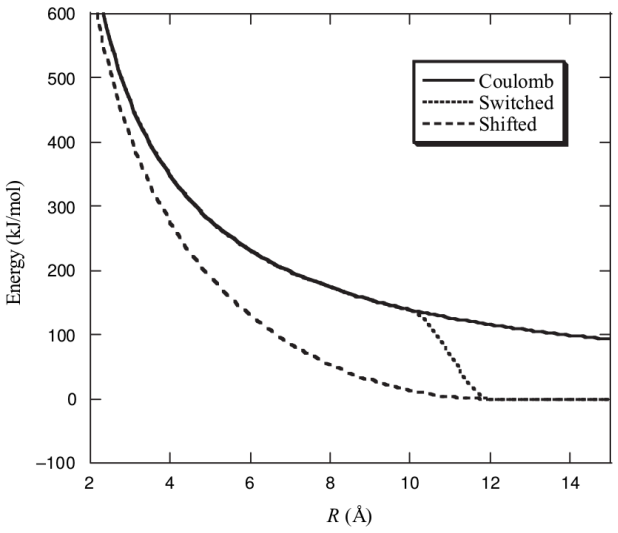

Figure 3.3: Representation of the switching and shifting truncation to the electrostatic interaction (Reprinted from ref. [127]).

In previous works it has been shown that this truncation method preserves the structural and dynamical properties of water [147] and it was validated in simulations of proteins in water solutions [145]. Furthermore, the water-graphene interaction was calibrated by adjusting the

parameters of the Lennard-Jones potential along with a Coulomb potential truncated at 1 nm, according to the binding energy and the water contact angle [148]. The obtained van der Waals energy interaction between water and graphene is interpreted as an average contribution from the "real" van der Waals energy, the induced electrostatic interactions and the Carbon-Hydrogen interactions that were not treated explicitly on that approach.

3.2.4 Initial Configuration

According to the integration algorithms (section 3.2.1), an initial configuration with positions and velocities for each particle is required. Thereby, the election of the initial positions of the particles is crucial to conduct a molecular study. For example, to perform simulations of liquids, an initial configuration from the crystal structure of the substance can be implemented, then this structure is melted under proper thermodynamic conditions of the liquid. Similarly, random initial coordinates can be assumed if particle overlapping and excessive short distances inducing strong repulsion between particles are avoided.

One of the most widely used initial lattice configuration in molecular modeling is the *face-centered cubic* lattice (see Figure 3.4.a.), which is inspired by typical crystalline structures of solids, such as NaCl or KCl crystals. In molecular studies of solids, the experimental crystal lattice is preferred. This is the case for Carbon Nanotubes for example, where the initial configuration comes from the rolling of graphene sheets. Different combinations of the rolling angles or axis of the sheet, produce different chiralities in the final carbon nanotube [149]. In Figure 3.4.b a Carbon Nanotube with zig-zag chirality is depicted.

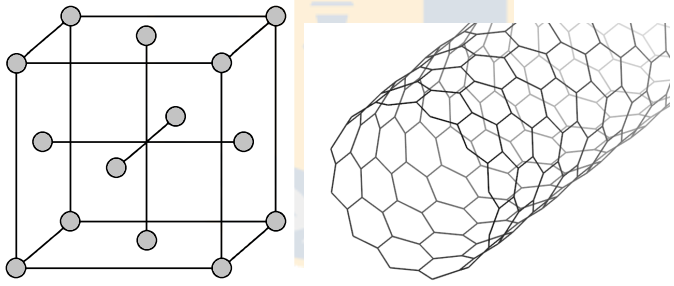

(a) (b)

Figure 3.4: Examples of initial configurations. (a) Face-centered cubic (fcc) lattice: basic configuration used in simulations inspired in the crystal structures of several solids (NaCl for example). (b) Rolled honeycomb crystal lattice for Carbon Nanotubes structures. Source: Own elaboration.

In terms of the initial velocities, a Maxwell-Boltzmann distribution is generally implemented, taking care that sampled velocities are consistent with any constraints imposed on the system. For a given temperature, T, and considering the mass of the particles m, the Maxwell–Boltzmann distribution for the velocity v is [138],

$$f(v) = \left(\frac{m}{2\pi kT}\right)^{1/2} e^{-mv^2/2kT} \tag{3.24}$$

In this way, a random velocity from the Maxwell–Boltzmann distribution at the temperature of interest is assigned to each particle.

In this thesis, the initial configurations are created using a molecular builder program developed in ETH, written in C and called with the acronym MMB [150]. This molecular builder

creates the initial configurations for the MD package, FASTTUBE, and contains the algorithms to easy create honeycomb lattices of Carbon Nanotubes and graphene, besides the classic lattices *fcc* or simple-cubic (one atom on each corner of a cube).

3.2.5 Hamiltonian Dynamics

As discussed in the previous sections, molecular dynamics solves the Newton's equations of motion to investigate molecular systems. Nonetheless, the rules of Statistical Mechanics provide the necessary connection between the microscopic laws and macroscopic observables [138]. These rules are based on the Hamiltonian and Lagrangian formulations of classical mechanics. This discussion will serve only as an introduction of the Hamiltonian concept, hence, for further reading the reader is referred to classic statistical mechanics books [138, 151].

First, instead of define the properties in term of the velocity, the momenta of the particle is more convenient, defined as $\mathbf{p}_i = m\dot{\mathbf{r}}_i$, where $\dot{\mathbf{r}}_i$ is the first derivative of the particle position. Thus, if the system is isolated, the Hamiltonian is simply the total energy of the system expressed as a function of positions and momenta by,

$$\mathcal{H}(\mathbf{r}_1, ..., \mathbf{r}_N, \mathbf{p}_1, ..., \mathbf{p}_N) = \sum_{i=1}^{N} \frac{\mathbf{p}_i^2}{2m} + U(\mathbf{r}_1, ..., \mathbf{r}_N) \tag{3.25}$$

where the summation at the right of equation 3.25 is the kinetic energy. Given the Hamiltonian, one can obtain the equations of motion for the system from it, known as the Hamilton's equations of motion. Considering that the Hamilton's equations are defined in generalized coordinates, for illustrative purposes the Hamilton's equations are presented here in the Cartesian coordinates,

$$\dot{\mathbf{r}}_i = \frac{\partial \mathcal{H}}{\partial \mathbf{p}_i} \qquad \dot{\mathbf{p}}_i = -\frac{\partial \mathcal{H}}{\partial \mathbf{r}_i}$$

If the forces are conservative the Hamilton's equations are completely equivalent to Newton's second law of motion. The most important property of the Hamilton's equations is that they conserve the total Hamiltonian:

$$\frac{\partial \mathcal{H}}{\partial t} = 0 \tag{3.26}$$

Since $\mathcal{H}$ is the total energy, equation 3.26 is just the law of conservation of energy.

3.2.6 Ensembles

The collective behavior of molecular systems has its theoretical foundation in Statistical Mechanics. In this framework, an ensemble is a collection of systems described by the same set of microscopic interactions and restricted by a common set of macroscopic properties (e.g. the same total energy, volume, and number of moles) [138,151]. Each system evolves under the microscopic laws of motion from different initial conditions so that at any time, every system has a unique microscopic state. Ensembles can be defined for a wide variety of thermodynamic situations, describing for example an isolated system from its surroundings, systems in contact with heat baths or coupled to pressure control mechanisms. Such ensembles are useful for determining static properties such as temperature, pressure, free energy, average structure, etc.

Given a long enough amount of time, the system will eventually visit all the microscopic states consistent with the constraints imposed to control the system. A system following this

hypothesis is said to be *ergodic* and can be used to generate different ensembles. Thereby, a macroscopic equilibrium observable G can be computed from M independent samples or states,

$$G = \frac{1}{M} \sum_{i=1}^{M} G_i \tag{3.27}$$

where G_i are instantaneous values of microscopic states. A familiar example is the temperature of a system which is related to the average kinetic energy. If an infinite number (or long enough [151]) of samples were available, then G would, by ergodicity, correspond to the ensemble average,

$$\lim_{M \to \infty} G = \langle g \rangle \tag{3.28}$$

where $\langle g \rangle$ is the ensemble average. In the molecular dynamics method, at some time t, the combination of positions $\mathbf{r}_i$ and momenta ($\mathbf{p}_i = m_i \mathbf{v}_i$) of all the particles represents one microscopic state. In this sense, in order to visit all the microscopic sates to describe the ensemble, simulations must be conducted for long enough times and averaged to generate the ensemble. However, in the study of any phenomenon, it is not known *a priori* how much is a *long enough* time. Therefore, special precautions must be taken to evaluate any macroscopic property (e.g. evaluating the standard deviation). Ergodicity problems are presented in systems wherein the potential energy displays high barriers. Systems with biological macromolecules such as proteins and polypeptides exemplify this problem, as important conformations are often separated by barriers in the space of the backbone dihedral angles or other collective variables in the system [138]. Other techniques are implemented to overcome this issue, such as coarse-grained methods [152, 153], assuming the cost of the atomistic detail compared to atomistic approaches.

The Microcanonical Ensemble

Statistical Mechanics defines the common restrictions in a system, or thermodynamic scenarios, to generate the different ensembles. The most fundamental scenario is a system isolated from its surroundings. Such system is described by a constant number of particles N in a container of volume V and constant total energy E corresponding to a Hamiltonian $\mathcal{H}$. This ensemble is known as the *microcanonical ensemble*.

Considering a dynamical system evolving according to Hamilton's equations of motion with constant particles in a fixed volume, the system will visit all the microscopic states with a constant energy. Therefore, in a molecular dynamics simulation, if the forces are conservative, simply by integrating the Newton's equations of motion the microcanonical ensemble is generated. For these reasons the microcanonical ensemble is the most fundamental equilibrium ensemble and provides a starting point from which all other equilibrium ensembles are derived.

The Canonical Ensemble

The main disadvantage of the microcanonical ensemble is that experiments, or the vast majority of natural processes, are not performed at conditions of constant total energy. Therefore, it is important to develop ensembles that have different sets of thermodynamic control variables in order to reflect more common experimental setups. The *canonical* ensemble is an example, wherein the thermodynamic control variables are the constant particle number N, constant volume V and constant temperature T. This ensemble characterizes a system in thermal contact with an infinite heat source where the energy can fluctuate.

This is explained as two connected NVE systems with exchange of energy between them, and assuming that the second system is much larger than the first system with $N_2 \gg N_1$, $V_2 \gg V_1$ and $E_2 \gg E_1$. Here, the universe consists of the combination of both systems with $E = E_1 + E_2$, and with the condition that the universe is treated within the microcanonical ensemble by means of the Hamilton's equations. Thereby, in the small system the energy fluctuates to generate a Boltzmann distribution due to the exchange of energy with the heat source to which it is coupled, leading to a constant temperature in the small system.

In molecular dynamics, several methods have been proposed to mimic the effect of a thermal reservoir. These methods are known as *thermostats* and can be classified into the coupling methods, the stochastic methods and the extended-system methods. One of the most commonly used thermostat is the coupling method developed by Berendsen et al. in 1984 [154]. This thermostat rescales the velocities of each particle every time step in such a way that the rate of change of the temperature is proportional to the difference between the heat bath temperature T_0 and the system temperature T,

$$\frac{dT}{dt} = \frac{1}{\tau_T}(T_0 - T) \tag{3.29}$$

where τ_T is a coupling parameter whose magnitude determines how strong is the coupling between the heat bath and the system. This method produces an exponential decay towards the target temperature T_0 according to the magnitude of the coupling constant τ_T. In this way, the velocities are rescaled with a λ factor defined as,

$$\lambda^2 = 1 + \frac{\delta t}{\tau_T}\left(\frac{T_0}{T(t)} - 1\right) \tag{3.30}$$

Thus, using for example the *leap-frog* algorithm (equation 3.19), the computed velocities of each particle are rescaled with the λ factor according to $\lambda \mathbf{v}(t + \frac{1}{2}\delta t) \rightarrow \mathbf{v}(t + \frac{1}{2}\delta)$.

The stochastic methods are based on applying stochastic disturbances to control the temperature according to the Boltzmann distribution. The most commonly used stochastic methods are the *Langevin* thermostat [155] and the *Andersen* thermostat [156]. In the Langevin thermostat a frictional force and a random force are applied to the momenta of the particles,

$$p_i = f_i - \gamma p_i + R_i \tag{3.31}$$

where γ is a friction coefficient, and R_i is a random force. Whereas the Andersen thermostat reassign the momentum of a random number of particles between a random number of steps according to the Boltzmann distribution. These methods must be used with special care when time-dependent properties, such as diffusion, wants to be computed, since these properties are directly dependent on the parameters used [157, 158].

The last methodologies to discuss are the extended-system methods. These are based on extending the degrees of freedom of the system in order to emulate the Newtonian dynamic of the external bath system. Since this method was introduced by Nosé [159] and modified later by Hoover [160], this thermostat is known as the Nosé-Hoover thermostat. In this method a new variable is introduced η, which is a scaling factor for velocities. This new variable has an

associated momentum $p_\eta = Q\dot{\eta}$, where Q is the "mass" of the extra degree of freedom. The motion equation for the extended system is then,

$$\dot{q} = \frac{p}{m} \tag{3.32}$$

$$\dot{p} = F(q) - p\frac{p_\eta}{Q} \tag{3.33}$$

$$\dot{p_\eta} = \sum \frac{p_i^2}{2m_i} - nk_BT \tag{3.34}$$

The temperature deviation from the heath bath drives the time derivative of the velocity scaling, rather than the scaling factor itself, as in the case of the coupling method. The Nosé-Hoover is widely used in simulations at equilibrium, however, the behavior of this thermostat is non-ergodic [161]. For this reason, Martyna et al. [162] formulated the Nosé-Hoover chain thermostat, which adds additional η variables to the thermostat. Although the Nosé-Hoover chain approach is valid at equilibrium, the desired kinetic temperature of the studied system away from equilibrium is not guaranteed [163, 164].

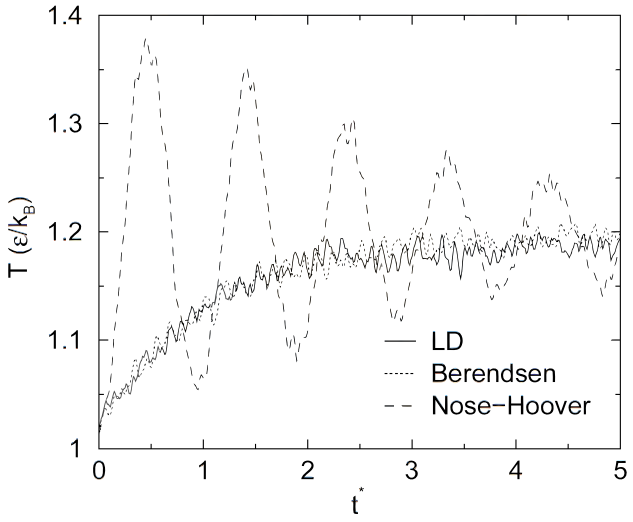

Figure 3.5: Comparison between the Langevin (LD), Nosé-Hoover and Berendsen thermostats for a system with 8000 Lennard-Jones particles (Reprinted from ref. [161]).

In order to evaluate the behavior of the thermostat, Hess on his thesis [165] compared the Nosé-Hoover, Berendsen and Langevin thermostats in a system consisting of 8000 Lennard-Jones particles, as shown in Figure 3.5. This study reports the oscillatory behavior of the Nosé-Hoover thermostat to reach the equilibrium, while the Berendsen and Langevin, proceed with a smooth exponential decay. The Nosé-Hoover thermostat is therefore much less suitable to reach the equilibrium but is reliable to generate a canonic ensemble at equilibrium [161]. In addition, the oscillating behavior of the Nosé-Hoover thermostat [163,165] and the deviation of time-dependent properties in the stochastic thermostats [157,158], suggest that the Berendsen thermostat is well suited to impose nonequilibrium conditions due to the direct coupling of velocities [154].

The Grand Canonical Ensemble

The third ensemble to be discussed is the *grand canonical* ensemble. This ensemble permits the fluctuations on the number of particles at constant *chemical potential* μ. This ensemble is introduced to describe situations where the particle number varies, such as the liquid-vapor equilibrium, vapor condensation or adsorption phenomena [166, 167].

The thermodynamic control variables in this ensemble are the chemical potential μ, volume V and temperature T. Similar to the canonical ensemble, the grand canonical is explained as two coupled NVE configurations but with exchange of energy and particles. In computational terms, because of the inherently discrete nature of particle fluctuations, the grand canonical ensemble does not easily fit into the continuous molecular dynamics framework. Therefore, the discussion of computational approaches to the grand canonical ensemble is referred to the literature [129, 138].

3.2.7 Nonequilibrium Molecular Dynamics

Molecular dynamics is a powerful technique to perform studies of thermodynamics properties such as a liquid-vapor equilibrium, heat capacity, surface tension or average structures [168, 169]. Moreover, molecular dynamics has also been used to calculate transport properties, like thermal conductivity or shear viscosity of fluids, by subjecting the system to an external perturbation of some kind [170, 171]. Hence, in general terms molecular dynamics can be classified into two categories:

- Equilibrium Molecular Dynamics simulations, which are the simulation setups performed in equilibrium ensembles such as the microcanonical (by simply integrating the Newton's equations), or the canonical ensemble (by rescaling the velocities of the particles and solving the Newton's equations).

- Nonequilibrium Molecular Dynamics (NEMD) simulations, where the system is subjected to a constant external perturbation while the Newton's equations are integrated. It represents a nonequilibrium state in the sense that, due to the presence of an external perturbation, the system at the steady state will be in a state of lower entropy. Upon removing the external field, the system will return to the equilibrium state or maximum entropy state [172].

The perturbations in a NEMD simulation can be imposed in two ways. (i) The boundaries of the system are subjected to a constant perturbation, in terms of velocity or force, and the system (or the subsystem of interest) is solved by integrating the equations of motion. The simulations of this type are known as *boundary-driven* NEMD [173–175]. (ii) The equations of motion are reformulated to include an external force [172, 176] and solved in time. In relation of heat transport studies, this type of simulations are known as *synthetic* NEMD [173, 176, 177] thus, for a general comparison, this type of simulations will be regarded as synthetic NEMD.

A practical and straightforward comparison between the boundary-driven and the synthetic NEMD is observed in studies wherein MD simulations are used to compute the shear viscosity of fluids confined between two parallel plates. The boundary-driven NEMD describes the case where the plates are subjected to a constant velocity, and in consequence the fluid will be moved by the shear of the fluid, i.e. Couette flow. In this case, the particles in the fluid are treated within the classic Newton's equation of motion. The synthetic NEMD, on the other hand, describe the case where a force is introduced in the equations of motion of the fluid by,

$$\dot{\mathbf{p}}_i = \mathbf{F}_i + f\hat{\mathbf{e}}_x \tag{3.35}$$

where, $\hat{\mathbf{e}}_x$ is a unit vector in the x direction and f is the magnitude of the external force. These two cases lead to different velocity profiles with the same behavior in viscosity of the fluid. It is important to note that boundary-driven NEMD intrinsically includes inhomogeneities in the system due to the interface with the boundary, while in the synthetic NEMD the relationship between flux and force is indirect. In general, the choice between these two techniques of NEMD will depend on the phenomenon under study and the system to analyze. For example, an interesting comparison between NEMD techniques and MD simulations was performed by Arya et al. in 2001 by analyzing the diffusion in porous media [178]. For further details of Nonequilibrium Molecular Dynamics the reader is referred to the literature [138, 172, 179].

3.2.8 Limitations of Molecular Dynamics

The main advantage of Molecular Dynamics along with the Force Field Methods is to reduce the computational cost associated in the computation of molecular systems in comparison with Schrödinger-based methods [127]. Furthermore, it allows the investigation of problems related with transport phenomena that it cannot be implemented in the time-independent *ab initio* methods.

However, this advantage it also reveals the clear limitations of Molecular Dynamics based on Force Field methods: Force Fields doesn't account for a sub-atomic description of the molecules, then ommiting sub-atomic behaviors that, depending on the parametrization and the phisical property to analyze, could influence the final results. For example, recent studies with *ab initio* calculations have suggested the preferred orientation of adsorbed water on graphene, with hydrogen pointing towards the grapehene layer, the so called $H \cdots \pi$ interaction or π-hydrogen bonding [180–182]. Similarly, the curvature in the sp^2 hybridization of carbon nanotubes induce an static dipole moment across the CNT walls. Hence, due to the Force Field nature, Molecular Dynamics cannot account for this behaviors accurately, which could have some influence in the study with ionic solutions. In general, Force Field methods are good for predicting properties for classes of molecules where a lot of information already exists. For unusual molecules, their use is limited and validations are required.

Finally, validations of Molecular Dynamics simulations are always demanded and strong arguments are always required in any investigation. This kind of discussion was recently addresed by van Gunsteren et al. [183]. In that Review, the authors discuss the general issues presented in molecular simulations with emphasis on the validation tools for those simulations. From that text is important to recall one quote: *Any model or theory used in a computer simulation involves choices (type of interaction or method). All involve assumptions and approximations.*

Chapter 4

Early Regimes of water capillary flow in slit silica nanochannels

Parts of this chapter have been published in: Elton Oyarzua, Jens H. Walther, Andrés Mejía and Harvey A. Zambrano. Early regimes of water capillary flow in slit silica nanochannels. *Phys. Chem. Chem. Phys.*, 2015, 17(22), 14731-14739.

4.1 Introduction

Over millions of years, nature has optimized nanoscale biomachinery to work efficiently in an aqueous environment. [4, 184]. Therefore, a molecular level understanding of fluid transport is critical to pursue novel opportunities in biochemistry, drug delivery technology and medical diagnostic devices. Indeed, fabrication techniques have evolved dramatically over the past two decades, [5, 185–187] allowing us to conceive integrated systems on length scales comparable to the size of intra-cellular structures [5, 188–190], opening the door to mimic the highly efficient natural fluidic processes in different technological areas [191–194]. Nevertheless, the study of flows confined inside nano-structures presents challenges to the application of macroscopic theories of fluids due to the fact that the extremely large surface to volume ratio and the short time and length scales (inherent to the nanoscale confinement) dominate the fluid transport. Therefore, an important bottleneck in the design and fabrication of integrated nanodevices arises from predicting the flows throughout nanoscopic conduits.

In nanofluidics, an important transport mechanism is capillary action. [6,57]. The fundamentals of the current understanding of capillarity are based on the early 19th century contributions made by Young [35] and Laplace [36]. The Young-Laplace theory of capillarity relates the pressure difference across a curved interface (Laplace pressure) to the surface tension acting on the interface as a result of its curvature. At the dawn of the 20th century, the studies carried out by Bell and Cameron [195] and later by Washburn [46] and Lucas [45], found capillary filling to be a square root dependent of time. The Lucas-Washburn (LW) equation relates the Laplace pressure across the capillary meniscus to the Hagen-Poiseuille equation for a fully developed viscous flow. Hence, the LW equation [46] describes the capillary filling assuming the no-slip boundary condition and considers the liquid penetration as being determined by a force balance between the capillary force and the viscous drag force. In the case of water invasion in a slit channel with the width much larger than the height, the LW equation results in:

$$l(t) = \sqrt{\frac{\gamma H \cos\theta}{3\mu}}\sqrt{t} \tag{4.1}$$

where l is the imbibition length, t is time, H is the channel height, μ is the dynamic viscosity (for the SPC/E water used herein: $\mu = 0.729\,\mathrm{mPa\ s}$ at $298\,\mathrm{K}$ [196]), γ is the surface tension (for SPC/E water: $\gamma \cong 0.064\,\mathrm{N\,m^{-1}}$ at $300\,\mathrm{K}$ [197, 198]), and θ is the static contact angle of the liquid on the channel wall. In this purely viscous flow model, the position of the meniscus relates with time as $l \propto \sqrt{t}$. Despite the fact that considerable effort has been devoted to develop more sophisticated models of capillarity [51, 55, 59, 68, 72, 73, 199–201] it has been certainly possible, in many technological applications, to assume a scenario where the LW equation predicts the capillary filling with sufficient accuracy. Nevertheless, in experiments of capillarity performed in sufficiently long nanoscale conduits, the imbibition kinetics qualitatively follows the LW model [11, 62, 63, 65, 66, 202, 203], reporting a slower filling rate than that predicted by the LW equation. In fact, during the last decade different explanations have been proposed for the observed reduction in the capillary filling speed. Tas et al. [62] attributed the slower capillary rates to the electroviscous effect. Persson et al. [63] extended the results reported by Tas et al. [62] and concluded that other effects, different from the electroviscosity, also contribute to the observed deviations in the imbibition rates. In the same context, Mortensen and Kristensen [76] found that the contribution of the electroviscous effect to the apparent viscosity is less than 1% and therefore concluded that the electroviscous effect is not sufficiently strong to account for the observed deviations. Subsequently, Thamdrup et al. [11] showed that the slower rates could be related to the formation of gas nanobubbles. However, van Honschoten et al. [6] pointed out that the Washburn model is derived for filling without bubbles and should therefore only be applied when no bubbles are present. Moreover, Chauvet et al. [79] found that slower capillary filling rates cannot be explained by enhanced viscous resistance due to nanobubbles. Specifically, Chauvet et al. [79] inferred that in sub 100 nm channels, the enhanced hydrodynamic resistance induced by the presence of nanobubbles, is compensated by the effect of the reduced volume to fill induced by the same gas nanobubbles. An alternative explanation to the filling deviations was presented by Haneveld et al. [66]. They proposed that water ordering near the channel walls due to strong liquid–surface interaction could be the origin of an interfacial region with enhanced viscosity which could explain the observed reduced capillary rates in nanochannels. The explanation proposed by Haneveld et al. [66] seems to correspond to the negative velocity slip length in silica pores reported by Gruener et al. [204] in experiments of water filling in networks of nanopores. Nevertheless, other detailed studies have not found such an interfacial layer with enhanced viscosity [205–208]. Furthermore, open questions remain about the role of line tension [209, 210], molecular roughness [211, 212], precursor films [200, 213], dynamic contact angle [72, 201, 214], and air displaced by the advancing meniscus [78, 79]. Therefore, a comprehensive explanation to the slower than expected capillary rates observed in the filling of nanochannels compared to the LW equation predictions remains an open question [6, 215]

The LW equation is an asymptotic model for long times of filling; when considering filling at short time and length scales, the LW model predicts an infinite imbibition velocity at $t = 0$. This singularity in the LW model has been attributed to the absence of the inertial drag related to the accelerating mass of fluid [50, 52, 53, 57, 61, 78, 199, 216]. In 1923 Bosanquet [61] incorporated the contributions of inertial drag and viscous resistance counteracting the capillary pressure. The Bosanquet equation, modified to describe the present capillary filling in a rectangular cross-section channel of width much greater than the height is:

$$l(t)^2 = \frac{2A_I^2}{B}\left[t - \frac{1}{B}(1 - \exp(-Bt))\right] \tag{4.2}$$

with,

$$A_I = \sqrt{\frac{2\gamma\cos\theta}{\rho H}} \tag{4.3}$$

$$B = \frac{12\mu}{\rho H^2} \tag{4.4}$$

where ρ is the liquid density (here $\rho = 997\,\mathrm{kg\ m^{-3}}$). The terms A_I and B represent the contributions to the capillary force balance from the inertial drag and from the viscous friction losses, respectively. In order to derive solutions to the momentum balance equation, Bosanquet assumed a particular scenario where the initial momentum of the liquid is zero. The derived solution depicts two cases. A visco-inertial regime for imbibition times sufficiently long, where the capillary filling can be described under the assumption of a developing viscous flow with a vanishing inertial drag effect ($A_I \to 0$). In this case, the Bosanquet model gradually converges into the LW model. In the opposite limiting situation, where the viscous force is much weaker than the inertial drag and the capillary force, the Bosanquet solution of the momentum balance equation gives:

$$l(t) = A_I t \tag{4.5}$$

where the A_I factor represents a constant initial velocity corresponding to the inertial term in the Bosanquet equation (eqn (4.2). Mathematically, the A_I velocity is a singular point of the Bosanquet equation, obtained by applying boundary conditions as limits on the imbibition velocity and the position of the capillary front (see section 2.1.4). Certainly, by taking into account the inertial drag, the methodology used by Bosanquet effectively overcomes the infinite velocity problem in the LW equation at $t = 0$. Nevertheless, it leaves open questions about the physical sense of the initial conditions at the beginning of the liquid uptake. Moreover, as pointed out by Kornev and Neimark [217] and Andrukh et al. [218] Bosanquet did not consider important phenomena affecting the imbibition dynamics at early times. Indeed, the Bosanquet equation neglects the relation between the initial velocity (A_I) and the momentum associated with the liquid moving towards the capillary entrance. When a liquid approaches a hydrophilic solid, once it enters the range of action of intermolecular forces, the adhesion effect gives rise to a start up impulse which affects the initial velocity of the liquid invasion. Therefore, quantitatively, the Bosanquet model cannot describe the initial kinetics of the capillary filling [216–218]. Moreover, in nano-confinement, the capillary filling speeds are typically high [50, 52, 218], therefore incorrect values of the velocity in the initial inviscid regime may result in significant deviations for predicting flow rates in short nano-slits.

Recently, the role of displaced gas in the capillary imbibition in closed-end [219–221] and open-end nanochannels [78, 79] has been addressed. In particular, Hultmark et al. [78] considered the role of viscous resistance from the displaced air on the kinetics of capillary filling, while Chauvet et al. [79] studied the effect on the imbibition rates of the transient pressurization of the air ahead of the capillary front.

In this study, we report molecular simulations performed to analyze the wetting kinetics in nano-confined fluids [17, 20, 52, 208, 222, 222–226]. Providing an atomistic description of the

capillary filling process on its earliest time stage and during the subsequent transition towards a fully developed flow regime, our study allows a complete characterization of the kinetics of liquid imbibition in nanodevices. Moreover, since the time scale associated to the diffusion of air throughout nanochannels is much larger than the time scale associated to the advancing capillary front, we examine the effect of air ahead of the moving meniscus as it is displaced by the liquid filling a slit channel at different air pressures.

4.2 Simulation details

To study the spontaneous capillary imbibition of water in an amorphous silica slit, a series of all-atom MD simulations are conducted using the simulation package FASTTUBE [139,148,226,227]. We use the potentials previously developed for modeling silica, water and air. [228]. In this force field, the potentials have been calibrated using dedicated criteria such as the contact angle of a water droplet on a silica surface ($\theta = 15°$), and the solubility of air in water at different pressures. The model is based on the simple point charge SPC/E model [133], and molecular nitrogen and oxygen. For the SPC/E water model [133], the O-H bond and the H-O-H angle are constrained using the SHAKE algorithm.

The silica is described by the TTAMm model developed by Guissani and Guillot [168]. For details of the potential we refer the reader to Zambrano et al. [228] To create an amorphous silica channel, cristobalite cells are replicated to build two parallel crystalline slabs. An annealing procedure is implemented [228,229], wherein the two silica slabs are coupled to a Berendsen heat bath with a time constant of 0.1 ps. The cristobalite is heated to 3000 K keeping the temperature constant during 10 ps, and subsequently, quenching the system from 3000 K to 300 K by imposing a cooling rate of 70 K ps^{-1} until the equilibrium state is reached.

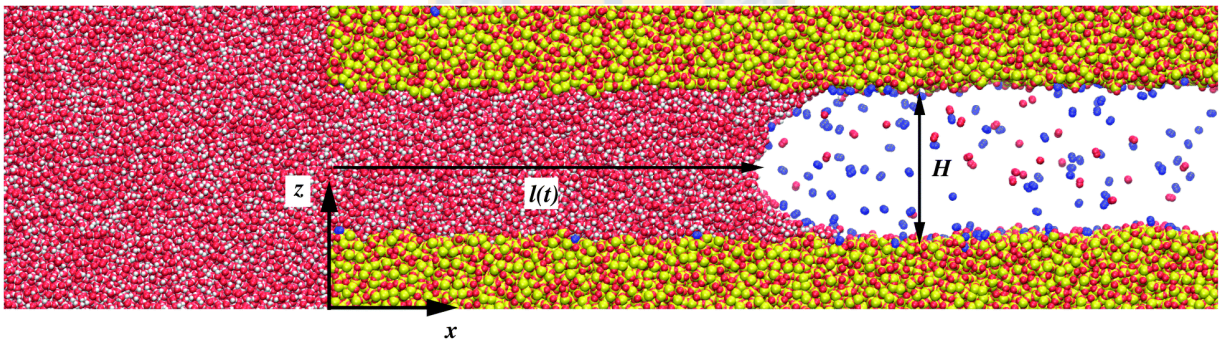

Figure 4.1: Capillary filling of water in a nano-slit silica channel. H denotes the height of the channel and $l(t)$ the time dependent penetration length. Source: Own elaboration.

The MD simulations are conducted to study the water imbibition in channels of different heights (H = 4, 6, 8, and 10 nm) surrounded by an air atmosphere at 0, 5, 10, 20 and 250 bar. The system consists of two slabs of amorphous silica with a size of 31.6 × 2.5 × 3.4 representing the channel walls. The slabs are aligned parallel to the x-y plane, while the height (H) of the channel is defined along the z-axis cf. Fig. 4.1. The simulations are conducted in a periodic orthorhombic box, the dimensions of the box are adjusted according to the size of each system and the corresponding air pressure to be reproduced. More details of the systems are listed in Table 4.1. In the simulations, using a time step of 2 fs, a water slab of 32000 molecules is coupled to a Berendsen thermostat [154] at 300 K during 0.5 ns; then, the thermostat is disconnected and

Table 4.1: List of the MD simulations of water imbibition. H and L are the height and the length of the silica slit channels as illustrated in Fig. 4.1. P is the corresponding gas pressure. The dimensions of the computational box are along the x, y and z directions, respectively. Source: Own elaboration.

Case	H (nm)	L (nm)	P (bar)	Box dimensions (nm)
1	4	31.6	0	$74 \times 2.5 \times 18.4$
2	6	31.6	0	$74 \times 2.5 \times 18.4$
3	6	31.6	5	$74 \times 2.5 \times 18.4$
4	6	31.6	10	$74 \times 2.5 \times 18.4$
5	8	31.6	0	$68 \times 2{,}5 \times 22.4$
6	8	31.6	5	$68 \times 2.5 \times 22.4$
7	8	31.6	10	$68 \times 2.5 \times 22.4$
8	10	31.6	0	$64 \times 2.5 \times 26.4$
9	10	31.6	5	$64 \times 2.5 \times 26.4$
10	10	31.6	10	$64 \times 2.5 \times 26.4$
11	6	50.6	0	$110 \times 2.5 \times 18.4$
12	6	50.6	20	$110 \times 2.5 \times 18.4$
13	6	50.6	250	$110 \times 2.5 \times 18.4$

the simulations are conducted in the microcanonical ensemble (NVE) until the system is equilibrated. Subsequently, the water slab is released from the rest to move spontaneously towards the silica channels. In the systems with air, after the silica-water interactions are equilibrated, the air molecules are released in the NVT ensemble at 300 K during 0.6 ns, then the thermostat is disconnected and the simulations are conducted in the NVE ensemble for 25 ns to ensure proper equilibration of the water and the air molecules. Afterward, the water molecules are constrained to move toward the channel at low velocity ($\approx 0.5\,\mathrm{nm\,ns^{-1}}$) until the water enters the region of action of intermolecular forces. The low velocity is chosen to ensure that the imbibition kinetics is not affected by the imposed velocity. Moreover, in order to explore the effects of air on the later stage of imbibition, three systems consisting of a water slab with 55000 molecules filling slits with a length of 50.6 nm are studied as listed in Table 4.1.

4.3 Results and discussion

In the present study, we conduct molecular dynamics (MD) simulations to investigate the spontaneous capillary imbibition of water in silica slit nanochannels as illustrated in Fig. 4.1. The slit channels studied here have heights and lengths in the sub-100 nm range as listed in Table 4.1. The penetration lengths of water spontaneously filling slit channels are computed by tracking the instantaneous positions of the advancing capillary front. The axial velocity profiles are computed by implementing a static binning procedure using a bin size of 0.2 nm along the z-axis. In order to estimate the effect on imbibition induced by gas molecules displaced by the advancing meniscus, density profiles of air ahead of the capillary front are computed using a dynamic binning with a reference frame attached to the center of the capillary meniscus. An example of the meniscus is

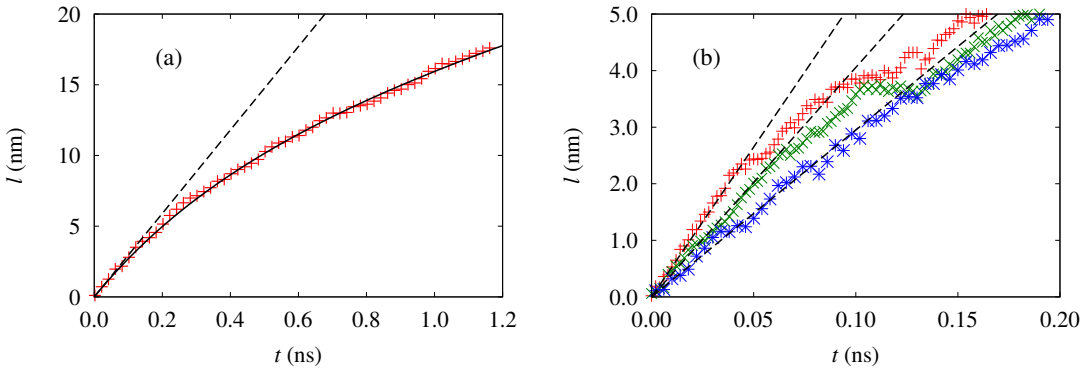

Figure 4.2: Position of capillary front as a function of time. (a) The red points (+) depict the imbibition length as a function of t for a slit channels of 10 nm. The black dashed line are visual guides to indicate the $l(t) = A_I t$ regime and the black solid line depicts the visco-inertial filling regime. (b) The red (+), green (×) and blue (∗) points depict the imbibition length as a function of t for channels of 6, 8, and 10 nm, respectively. The dashed lines are visual guides indicating the linear least-squares fit to the constant velocity regime. Source: Own elaboration.

shown in Fig. 4.1.

In Fig. 4.2a, we plot the temporal evolution of the imbibition length as a function of time for a channel with of height of 10 nm. The imbibition for channels of 6 and 8 nm are presented in Appendix A.1. In Fig. 4.2a the dashed line represents a constant velocity regime of imbibition. The results indicate that at the beginning of the imbibition, the capillary front moves at constant velocity. Subsequently, at $t = 0.13$ ns the filling kinetics departs from being linear in time and follows a visco-inertial regime (eqn. 4.2) depicted by the black solid line in Fig. 4.2a. Moreover, Fig. 4.2b shows the capillary filling length as a function of time during the first 0.2 ns of the imbibition process for slit channels of 6, 8, and 10 nm. The time histories confirm that during the early time of capillarity, the progression of the meniscus position displays a linear dependence of time, which indicates a capillary flow with a constant velocity for all the channels. The slopes of the linear fits represent velocities of ca. 52, 41, and 30 nm ns^{-1} for slits of 6, 8, and 10 nm, respectively. The decrease in velocity for increasing channel height is consistent with eqn. 4.3 and previous studies [50, 57, 216, 218]. Moreover, the results indicate that the duration of the inviscid regime is height dependent. Therefore, the transition times (t_I), between the filling regimes, are 0.05, 0.07 and 0.13 ns for the channels of 6, 8, and 10 nm cf. Fig. 4.2b.

Fig. 4.3 shows the axial velocity profiles computed at different stages of the capillary filling in a slit channel of 6 nm. In order to compute the axial velocities, atomic trajectory data have been collected every 10 fs. The solid blue line depicts the flow velocity profile computed between $t = 0.010$ ns and $t = 0.045$ ns. The profile exhibits a plug shape which indicates that during the corresponding period the flow is inviscid. Hence during this period the capillary force is counteracted exclusively by inertial effects. The flow velocity of the solid blue line in Fig. 4.3 is consistent with the fitted velocity in the 6 nm height channel in Fig. 4.2.b at early times, a velocity of ca. 52 nm ns^{-1}. In agreement with previous investigations [57, 217, 218], the magnitude of the initial constant velocities of capillarity computed here do not correspond quantitatively to the velocities predicted by the Bosanquet inertial solution. Indeed, for a slit channel with a height of 6 nm, the initial constant velocity predicted by the Bosanquet solution is $A_I = 143.8$ nm ns^{-1}, which is ca. 180% higher than the initial velocity computed in this study (see also Appendix A.2).

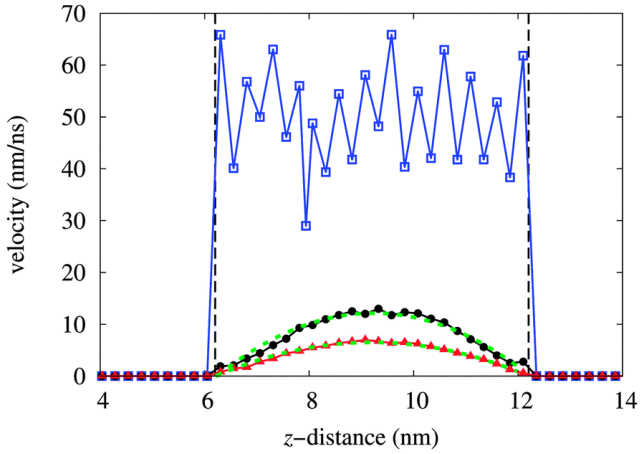

Figure 4.3: Axial velocity profiles for a slit channel with height of 6 nm. The reference position ($z = 0$) is located at the boundary of the computational domain. The profiles are computing extracting trajectories every 10 fs. The vertical dashed black lines represent the position of the channel walls. The solid blue (□), black (•), and red (▲) lines are velocity profiles sampled at $t \in [0.010,\ 0.045]$ ns, $t \in [2.200,\ 3.200]$ ns, and $t \in [4.100,\ 5.000]$ ns, respectively. The dotted green lines depict the fit to a parabolic flow profile. Source: Own elaboration.

In order to analyze the influence of the factors such as the pre-history of the wetting and the formation of the meniscus on the initial velocity of capillary imbibition we perform MD simulations of a water slab moving towards the entrance of the slit channels with heights of 6 nm and 10 nm. In these simulations we impose different initial velocities. Specifically, the water slabs are released 1 nm away from the channel entrance at velocities between 0 and 40 nm ns^{-1}. Fig. 4.4 shows the instantaneous position of the water free-surface during the pre-wetting period and, subsequently, the position of the capillary front during the beginning of the water uptake process for different imposed initial velocities: 0, 10, 20, 30, and 40 nm ns^{-1}, respectively. The results indicate that the velocity of imbibition during the inviscid regime of capillarity is not affected by the particular initial momentum. Moreover, we find that the capillary meniscus completes its formation at different distances depending on the particular channel height. For channels of 6 nm, we compute a dynamic contact angle of ca. 80° during the entire inviscid regime of imbibition (see Karna et al. [230]). In fact, as we introduce the computed value of the initial dynamic contact angle in the Bosanquet inertial solution (eqn. 4.3), the constant velocity, A_I, becomes equivalent to the corresponding velocity directly computed from the MD trajectories (ca. 52 nm ns^{-1}). It confirms that the process of formation of the capillary meniscus is part of the explanation to the quantitative deviations in the initial velocity of imbibition previously reported [57, 217, 218]. Nevertheless, we regard that more studies are required to determine the complex relation between the initial velocity of capillarity and coupled phenomena such as the hydrodynamic losses at the channel entrance [226], the specific dynamic features of the imbibing flow, and the interfacial viscoelasticity [231] associated with the transfer of momentum at the beginning of the capillary uptake.

During the later stages of the capillary filling, viscosity can no longer be neglected. Fig. 4.2 shows that the inviscid constant velocity regime is followed by a subsequent period wherein the capillary filling kinetics departs from being linear in time. The velocity profile depicted by the solid black line in Fig. 4.3 is computed in a channel with a height of 6 nm. The axial velocities are

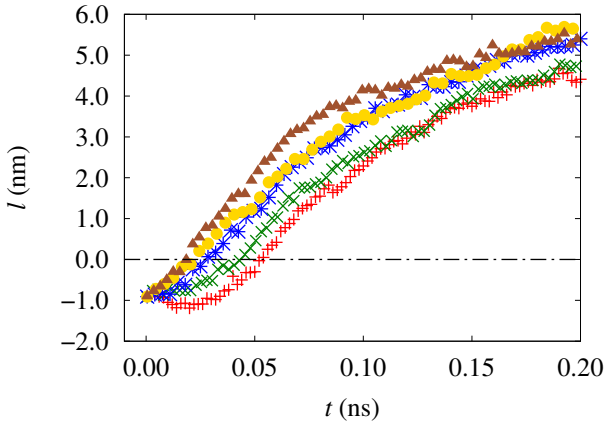

Figure 4.4: Pre-history of the capillary imbibition process for the channel of 6 nm. The red (+), green (×), blue (∗), yellow (•) and brown (▲) points depict the temporal evolution of the position of the liquid–vacuum interface for imposed initial velocities of 0, 10, 20, 30, and 40 nm ns^{-1} respectively. The dashed black line indicates the position of the channel entrance. For all the imposed initial velocities, it could be observed a filling regime with constant velocity $l(t) = A_I t$ regime immediately after the water uptake. Source: Own elaboration.

averaged between t = 2.2 ns and t = 3.2 ns. The flow profile displays a significant velocity gradient in a direction normal to the wall which confirms that viscous losses have to be taken into account. We infer that after the transition time, e.g., for a channel of 6 nm, $t_I = 0.05$ ns, the Laplace force driving the filling is balanced by a competition between inertial and viscous drags. We regard this stage of capillarity as the visco-inertial regime. Theoretical studies [53] of capillary filling have found that this visco-inertial stage, following directly the purely inviscid-inertial regime, corresponds to the visco-inertial regime described by the Bosanquet equation [61, 216] as term $B \neq 0$ (eqn. 4.4). In this work we compute the temporal position of the meniscus during the capillary filling of slit nanochannels and find good agreement to the Bosanquet model (eqn. 4.2). Indeed, Fig. 4.2.a and Fig. 4.5.a show that the capillary filling kinetics follows the Bosanquet model for channels of 10 nm and 6 nm, respectively, with a deviation of ca. 2.5%. We attribute this deviation to the molecular roughness of the silica walls of the nanochannels. It should be noted that as the liquid imbibition evolves inside the channel, progressively the viscous flow losses will dominate the inertial drag. At the moment, when the viscous friction losses dominate the force due to the Laplace pressure, the Bosanquet filling regime converges into a regime dominated by the viscous friction drag where inertial effects can be neglected. Indeed, Fig. 4.5 shows that the filling kinetics displays a $l(t) \propto \sqrt{t}$ after ca. 3.5 ns for a channel of 6 nm and after ca. 0.6 ns for a channel of 4 nm, respectively, which indicates that the capillary filling has reached the purely viscous regime. It should be noted that the filling kinetics for the channels of 4 and 6 nm deviates ca. 20% from quantitative prediction using the LW equation (eqn. 4.1).

We study systematically the influence of air on the imbibition kinetics of water in nanochannels by performing simulations of capillary filling at different air pressures. The density profiles shown in Fig. 4.6 for the 6 nm channel subject to air pressures of 10 and 20 bar clearly demonstrate an accumulation of gas in front of the meniscus of ca. 4.0 kg m^{-3} corresponding to at least an overpressure of 3.5 bar. Similarly, the 10 nm channel subject to a gas pressure of 10 bar experiences a gas accumulation of ca. 1.7 kg m^{-3} and an overpressure of 1.5 bar (Fig. 4.6). The

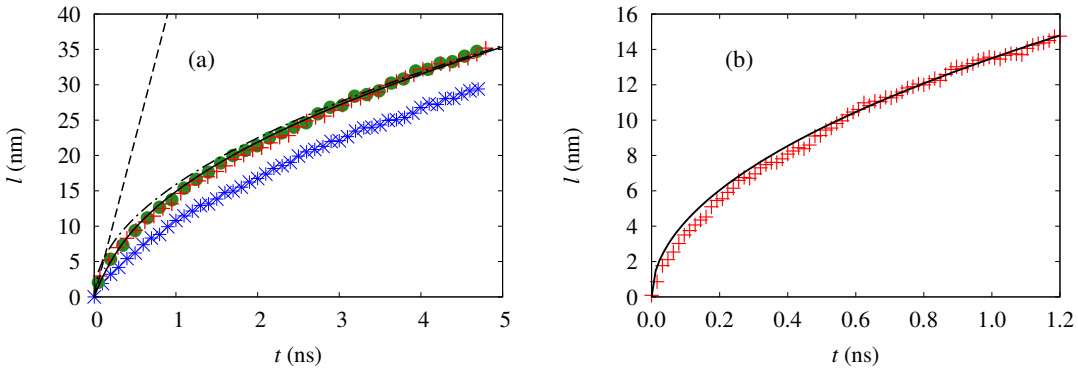

Figure 4.5: Imbibition length as a function of time. (a) The green (•), red (+) and blue (∗) points depict the position of the meniscus as a function of time for a channel of 6 nm in vacuum, at 20 and at 250 bar, respectively. The dashed lines correspond to a linear regression in the constant velocity regime. The solid and dashed-dotted black lines are a visual help to indicate the visco-inertial and LW ($l(t) \propto \sqrt{t}$) imbibition regimes, respectively. (b) The red (+) points show the position of the meniscus as a function of time for a channel of 4 nm in vacuum. The solid black line shows the filling regime following $l(t) \propto \sqrt{t}$. Source: Own elaboration.

computed overpressure values suggest that the accumulation of gas is size-dependent; higher overpressures are computed for channels with smaller height. In order to extend the study of the effect of displaced air on the capillary filling rates, a simulation of a channel of 6 nm subjected to an air pressure of 250 bar is conducted. In Fig. 4.6, the density profile of air for the channel of 6 nm at 250 bar reveals an accumulation of gas in front of the meniscus of ca. 39.5 $\mathrm{kg\,m^{-1}}$ corresponding to an overpressure of at least 34 bar. Fig. 4.5a shows that the capillary filling kinetics qualitatively follows the Bosanquet model for a channel of 6 nm in the presence of air at 20 and 250 bar. Moreover, Fig. 4.5a shows that the filling rate for the case of 250 bar deviates ca. 30% from the filling rate computed under vacuum. It demonstrates that air occupying nano-meter long slit channels does offer a mechanical resistance to the capillary penetration of the water. Furthermore, the results of the present study suggest that the accumulative effect of the gas viscous friction and the pressurization on the meniscus could be part of the explanation for the slower than expected capillary filling rates observed in experiments of long (> 100 nm) channels [11, 62, 65, 66, 202].

4.4 Conclusions

In this study, we present an investigation of the early stage of capillarity in slit nanochannels in the nanoscale range. Performing all-atom large-scale MD simulations, we confirm that the spontaneous capillary filling of slit silica channels follows a purely inviscid flow regime with constant velocity during the very first stage of imbibition. Subsequently, the capillary filling kinetics evolves in a developing flow where the capillary force is balanced by contributions from inertia and viscous drag losses. As the filling length becomes sufficiently large, the inertial effect on the imbibition dynamics becomes negligible with regard to the viscous drag and a fully developed Poiseuille flow is attained. Furthermore, the effect of the influence of air on the imbibition is systematically investigated. We predict a gas overpressure in front of the

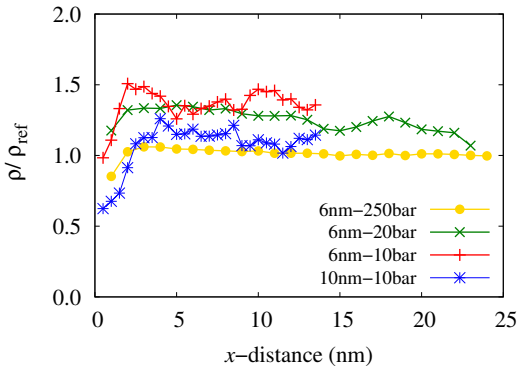

Figure 4.6: Transient accumulation of gas computed ahead of the capillary front. The reference densities (ρ_{ref}) are 9.8 kg m^{-3} for the channels of 6 nm and 10 nm at 10 bar, 16 kg m^{-3} for the channel of 6 nm at 20 bar and 262 kg m^{-3} for the channel of 6 nm at 250 bar. The green ($\times$) and yellow ($\bullet$) lines are the air densities for a channel with height of 6 nm at 20 and 250 bar respectively, as a function of the distance from the advancing meniscus. The red ($+$) and blue ($*$) lines depict the air density at 10 bar as a function of the distance from the advancing meniscus for channels with heights of 6 nm and 10 nm, respectively. Source: Own elaboration.

advancing meniscus as the capillary action takes place. Moreover, our results indicate that in slit channels the air displaced by the imbibing water is found to have an important effect on the capillary filling kinetics. In this study we provide an approach to extend the applicability of the Bosanquet model of capillarity to describe nanoscale imbibition of water. The approach consists of a modified Bosanquet equation with the initial constant velocity computed directly from atomistic simulations. The proposed model is suitable for describing the entire capillary filling process in nanoscopic slit channels in the presence of air.

Chapter 5

Water thermophoresis in Carbon Nanotubes: the interplay between thermophoretic and friction forces

Parts of this chapter have been published in: Elton Oyarzua, Jens H. Walther and Harvey A. Zambrano. Early regimes of water capillary flow in slit silica nanochannels. *Phys. Chem. Chem. Phys.*, 2018, 20, 3672-3677.

5.1 Introduction

Thermophoresis is a directed motion of particles caused by the presence of an externally imposed thermal gradient. In particular, thermophoretic movement of a particle suspended in a molecular media is the consequence of a thermally rectified Brownian motion [85, 232]: molecules in the hotter region of the media collide with the particle, transferring a greater momenta as compared to the molecules in the colder regions. During more than a century, theoretical and experimental studies have been conducted to understand the factors governing the termophoretic transport and elucidate its complex underlying physics [91, 233, 234]. One of these pioneer investigations was made by Epstein in 1929 [92], who derived the first expressions for the thermophoretic force and velocity. Thereafter, motivated by its important practical consequences in the field of aerosol technology [235], numerous investigations of thermophoresis of particles in gases have been conducted [94,96,97,236,237]. Thermophoresis of suspended particles in liquids was first studied by McNab and Meisen [93], who found thermophoretic motion of a particle to be independent of the particle size. More recently, and motivated for potential applications of nanofluid solutions, this phenomenon has also been studied in dispersions of nanoscale particles immersed in fluids [103–105]. Thermophoresis is fundamentally related with the phenomenon of thermodiffusion in liquid solutions [100, 233], also called the Ludwig-Soret effect [233, 237] after Carl Ludwig [238] and Charles Soret [239] who independently studied this phenomenon in the 19th century.

Nowadays, the advent of extremely accurate nanofabrication techniques has led to envision novel integrated nanofluidic devices wherein the functional stations are connected by nanoconduits [23,240,241]. In this context, thermophoresis may play a critical role as an enabling technology for achieving controlled transport of fluids in nanoscale devices. Recently, carbon nanotubes (CNTs) [242] have emerged as ideal conduits for ultra-efficient water transport [243–246] due to their molecularly smooth graphitic walls [247], well controlled diameter, spatial nanoconfine-

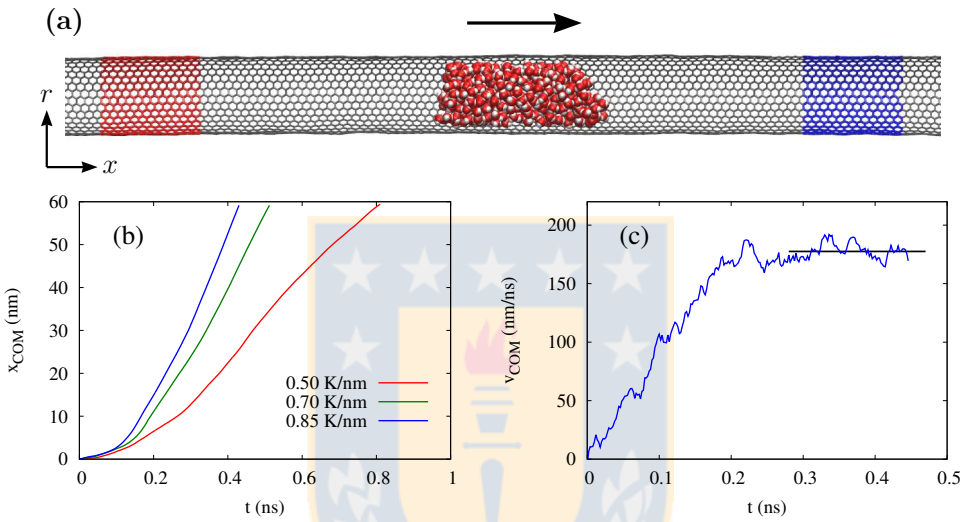

Figure 5.1: (a) Schematic of the studied system. The droplet inside the CNT moves from the high temperature side towards the cooler side of the CNT. The thermostat is applied directly to the carbon atoms, the red zone represents the high temperature section while the blue zone represents the low temperature section. (b) Time evolution of the center of mass position of the droplet consisting of 800 water molecules under different imposed thermal gradients. (c) History of the velocity of the center of mass of the droplet consisting of 400 water molecules under a imposed thermal gradient of 0.50 K/nm. The solid line depicts the constant velocity regime. Source: Own elaboration.

ment and outstanding thermal and mechanical properties [244, 248]. Hence, the thermophoretic transport of fluids through the inner-core of CNTs has considerable technological and scientific implications. In fact, the practical use of thermophoresis in future CNT-based nanofluidic devices requires the feasibility of achieving predictable and controllable thermophoretic water transport inside CNTs. To date, despite the important efforts that have been devoted to investigate thermophoresis inside and outside CNTs [106, 107, 110, 111, 249–252] [20, 253–256], the interplay between applied thermal gradient, thermophoretic velocity, solid-liquid friction [247, 257–259] and thermophoretic force [110, 250, 252] in a water/CNT system, has not been studied. In this chapter, we present an atomistic study of the kinetics associated with thermophoresis of water nanodroplets confined inside single wall carbon nanotubes and its interplay with the solid-liquid friction force.

5.2 Methodology

To carry out this investigation, we employ both constrained and unconstrained Molecular Dynamics simulations of nanodroplets confined in CNTs which are subjected to a constant axial thermal gradient. The axial thermal gradient is applied by coupling two Berendsen thermostats [154] at different temperatures to the carbon atoms at the respective ends of the CNT cf. Fig. 5.1a. As demonstrated in previous studies, a Berendsen thermostat is suitable for imposing proper nonequilibrium conditions in CNTs [161, 260], and also exhibit correct mechanical responses at relatively constant temperature during CNT compression [261]. The MD simulations are performed using the parallel MD package FASTTUBE [17, 20, 106, 139]. The equations of motion are integrated in time using the leapfrog scheme with a time step of 2 fs. Periodic boundary conditions are considered in the direction parallel to the CNT axis and with free space conditions in the normal directions. The carbon-carbon intramolecular interactions of the CNT are described by a Morse bond, a harmonic cosine of the bending angle, and a torsion potential [20, 106, 110, 139]. The water is modeled using the rigid SPC/E water model [133] with the O-H bond and the H-O-H angle constrained using the SHAKE algorithm. The water-CNT interactions are described by a 12-6 LJ potential calibrated to reproduce a water contact angle of 81° as described by Werder et al. [148] and Zambrano et al. [20]. The van der Waals and Coulomb interactions are truncated at 1.0 nm with the Coulomb potential smoothly truncated to ensure energy conservation [20, 139]. The MD package and the force fields have been extensively validated in previous studies of thermophoresis [20, 106, 110, 148, 252, 262]. For details of the potentials and setup of the simulations, we refer the reader to Zambrano et al. [20].

In the unconstrained MD simulations of thermophoresis [20, 106, 111, 250–253, 256], a constant thermal gradient is applied along the axis of the CNT. The imposed thermal gradient induces a thermophoretic motion of the confined nanodroplet in the opposite direction of the thermal gradient. Moreover, in line with the results presented by Shiomi and Maruyama [256], two regimes in the movement of the nanodroplet are observed: first an acceleration regime wherein the thermophoretic force is larger than the friction force, and then, a constant velocity regime, wherein the thermophoretic force balances the friction force and the droplet reaches its terminal velocity. Furthermore, to gain insight in the kinetics of the droplet motion, constrained MD simulations are conducted. This set of simulations consists of setting the center of mass velocity (v_{com}) every time step to a target value, forcing the droplet to move with a constrained velocity without affecting the velocity distribution of the molecules in the droplet. Constrained MD simulations are performed with and without imposed thermal gradients. The MD simulations

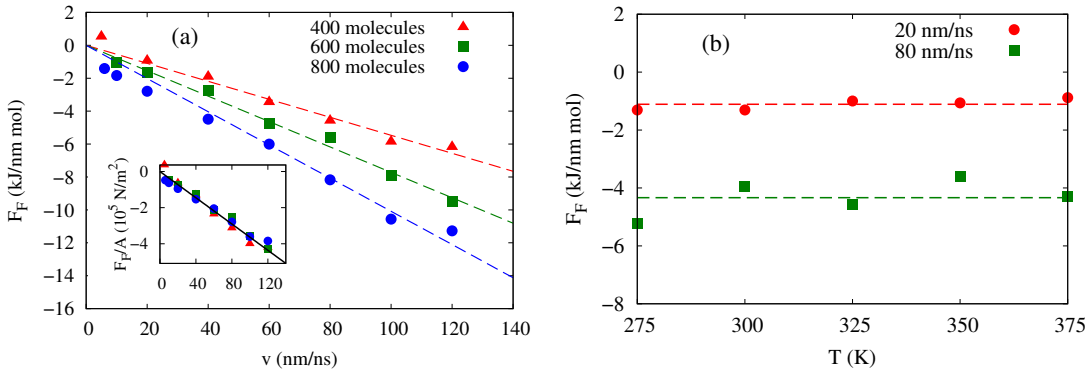

Figure 5.2: (a) Friction force as a function of the velocity of center of mass (v_{com}) for droplet sizes 400(▲), 600(■) and 800(●) water molecules at 325 K. The dashed lines are fits to the data. Inset: Friction forces divided by the respective solid-liquid contact area. (b) Friction force as a function of temperature with imposed v_{com} of 20 nm/ns and 80 nm/ns with a droplet of 400 water molecules. The dashed lines are fits to the data. Source: Own elaboration.

with constrained velocity were introduced by Schoen et al. [106] and then, in a similar context, reported by Zambrano et al. [252]. Further details of this technique are provided in Appendix B.1.

5.3 Results and discussion

In this study, an armchair CNT with chirality (17,17) and length of 75 nm is considered for all cases. Thermal gradients of 0.2, 0.5, 0.7 and 0.85 K/nm are imposed along the axis of the CNT wherein water nanodroplets of different sizes are confined. The nanodroplets confined in the CNTs consist of 400, 600 and 800 water molecules. A schematic of the system is shown in Fig. 5.1a. From the atomistic trajectories, the temporal evolution of both position and velocity of the center of mass of the droplets are extracted. In line with previous studies [20,106,252,256], a directed displacement of the droplet is observed from the high temperature zone towards the low temperature zone. Moreover, for all cases we observe higher center of mass velocities as higher thermal gradients are imposed along the CNT cf. Fig. 5.1b. Furthermore, as shown in Fig. 5.1c, during the droplet displacement two dynamic regimes can be identified: first a regime with increasing velocity in time and subsequently, a constant velocity regime as depicted by the solid line. We notice that in this set of simulations, the only forces acting on the droplet are the thermophoretic force (F_T) which is the force exerted by the thermal gradient, and the retarding friction force (F_F) acting at the solid-liquid interface, hence, the resulting net force is

$$F_N = m \cdot a = F_T - F_F \tag{5.1}$$

where m is the mass of the droplet and a is the instantaneous acceleration. Figure 5.1c infers that within the first regime the magnitude of the thermophoretic force acting on the droplet is higher than the magnitude of the friction force, conversely, during the constant velocity regime, the retarding friction force balances the thermophoretic force, i.e., the droplet reaches its maximum velocity at zero net force. The behavior exhibited by the droplet motion suggests that the instantaneous magnitude of the friction force and/or the thermophoretic force must be dependent on

the instantaneous velocity of the droplet. In order to analyze the relationship between the droplet speed and the thermophoretic and friction forces, sets of isothermal and non-isothermal MD simulations are performed at different constrained velocities. From the constrained simulations with an imposed thermal gradient, the instantaneous net force (F_N), i.e., the force instantaneously accelerating the droplet is computed from the simulations, similar to the analysis performed by Schoen et al. [106] and Zambrano et al. [252]. Furthermore, the instantaneous retarding friction force (F_F) is computed from the constrained simulations at constant temperature. The thermophoretic force (F_T), which is the force exerted on the droplet by the imposed thermal gradient, is calculated by adding the friction force (F_F) to the net force (F_N) at the respective velocity, according eqn. (5.1). We notice that the center of mass velocity (v_{com}) of the droplet is assumed to be equivalent to the slip velocity considering the ultra-high slippage inherent in the water-CNT interface, in line with Falk et al. [257]. In fact, previous investigations [246, 263, 264] reported water slip length over 75 nm for a CNT of 2 nm in diameter, leading to a plug-like velocity profile for water confined in CNTs [20, 247]. Furthermore, Chen et al. [265] found that water droplets spontaneously slip inside CNTs owing to thermal fluctuations of water at room temperature.

The friction force as a function of the constrained center of mass velocity is shown in Fig. 5.2a. In line with the previous studies [257, 258, 266], the magnitude of the friction force increases for higher velocities of the droplet. Indeed, the magnitude of the friction force is linearly proportional to the droplet velocity. Note that the negative values in the magnitude of the friction force are due to the force direction opposite to the displacement of the nanodroplet. In Fig. 5.2a, each point is computed from the atomic trajectories obtained from independent 3 ns MD simulations at constant temperature, the red, green and blue dashed lines are fits to the data assuming $F_F = 0$ for $v = 0$ [265]. Moreover, the dashed lines in Fig. 5.2a. display different slopes because each nanodroplet (400, 600 and 800 molecules) has different liquid-solid contact areas. In fact, if the magnitudes of the computed friction forces presented in Fig. 5.2a are divided by the respective contact area, all the data converge to a single slope, as shown in the inset of Fig. 5.2a, where the magnitude of the slope corresponds to a friction coefficient of $3631\,\text{Ns/m}^3$. Moreover, as the temperature imposed along the CNT is systematically varied in each isothermal simulation, the friction force is found to be independent of the imposed temperature in the range considered (see Fig. 5.2b). Thus, in non-isothermal simulations we assume that the magnitude of the friction force does not change as different thermal gradient are imposed along the CNT.

The net force (F_N) acting on the nanodroplets is computed from constrained MD simulations with imposed thermal gradients. Constant velocities ranging from 3 m/s to 120 m/s are imposed to the center of mass of the droplet while thermal gradients of 0.20, 0.50 and 0.70 K/nm are applied along the axis of the CNT. For the case of a water droplet of 400 molecules, the net force as a function of the imposed velocity is depicted in Fig. 5.3a. For all the imposed thermal gradients, we observe that the instantaneous net force decreases linearly with the imposed velocity, starting from a positive value at zero velocity and decreasing until it vanishes when the droplet achieves its terminal velocity. Moreover, it should be noted in Fig. 5.3a that the slope of the blue, green and red dashed lines is equivalent to the slope for the corresponding dashed red line in Fig. 5.2a, which is the friction coefficient times the solid-liquid contact area. The dashed red line in Fig. 5.2a shows the friction force versus velocity for the same droplet consisting of 400 water molecules, therefore, the decrease in the net force is due to the growth of the friction force with higher velocities. Since $F_N = m \cdot a$, the thermophoretic motion of the droplet is associated with a decreasing acceleration during the first regime (see Figure B.4 in Appendix B), before the terminal velocity is reached, showing no evidence of a constant acceleration regime during the

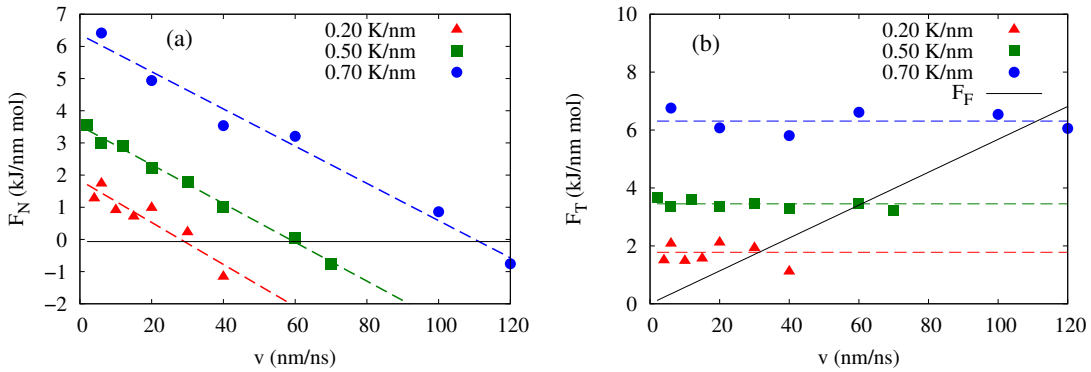

Figure 5.3: Net force and thermophoretic force of the 400 water molecules case under thermal gradients of 0.20 K/nm (▲) 0.50 K/nm (■) and 0.70 K/nm(●). (a) Net force as a function of the velocity of center of mass. The solid black line is a guide for $F_N = 0$. (b) Thermophoretic force as a function of the velocity of center of mass. The dashed lines are fits to the data. The solid black line is the absolute value of the friction force for the 400 water molecules case (Fig 2.a). Source: Own elaboration.

thermophoretic motion as inferred by previous authors [256, 267].

From the computed friction and the instantaneous net forces, the thermophoretic force is calculated. In Fig. 5.3b the thermophoretic force for the 400 water molecules case is presented, wherein each point is obtained from the sum of the net force (F_N) computed from the constrained simulations (Fig. 5.3a) and the friction force (F_F) (Fig. 5.2a) at the corresponding velocity, according to Eq. (7.1). As depicted in Fig. 5.3b, the thermophoretic force displays no dependency on the droplet velocity, i.e., the droplet is subjected to a constant thermophoretic force during the motion. Moreover, Fig. 5.3b shows that for higher imposed thermal gradients, the thermophoretic force increases as observed in previous studies [106, 250, 252, 256]. We note that the relation between velocity and thermophoretic force has been studied for systems consisting of motile coaxial CNTs [252] wherein a decreasing thermophoetic force has been observed for higher velocities of the inner CNT. Conversely, in the present study for a solid-liquid interface, we find that the thermophoretic force is not velocity dependent while the friction force increases linearly with the droplet speed.

It is also interesting to evaluate the effect of the size of the droplets on the thermophoretic and net force. The net force as a function of the constrained center of mass velocity is shown in Fig. 5.4a for droplets consisting of 400 (red triangles), 600 (green squares) and 800 (blue circles) molecules under an imposed thermal gradient of 0.50 K/nm. The dashed lines in Fig. 5.4a are linear fits for each case, with the slopes depicting the friction coefficient times the respective solid-liquid contact area. Note that the solid-liquid contact area is larger for droplets with higher number of water molecules. Therefore, Fig. 5.4a indicates that all the nanodroplets move with a decelerated motion, slowed down with a rate that is directly proportional to the size of the particular nanodroplet (See Fig. 5.2a), i.e., at the same instantaneous speed, droplets with a larger solid-liquid contact area experience a higher retarding friction. Indeed, as shown in Fig. 5.4a for an imposed thermal gradient of 0.50 K/nm, the magnitude of the terminal velocity is higher for droplets with smaller number of water molecules. The same behavior is observed for different imposed thermal gradients as shown in Figure B.5 in Appendix B. Furthermore, the thermophoretic force is computed from the net force values presented in Fig. 5.4a. In Fig. 5.4b,

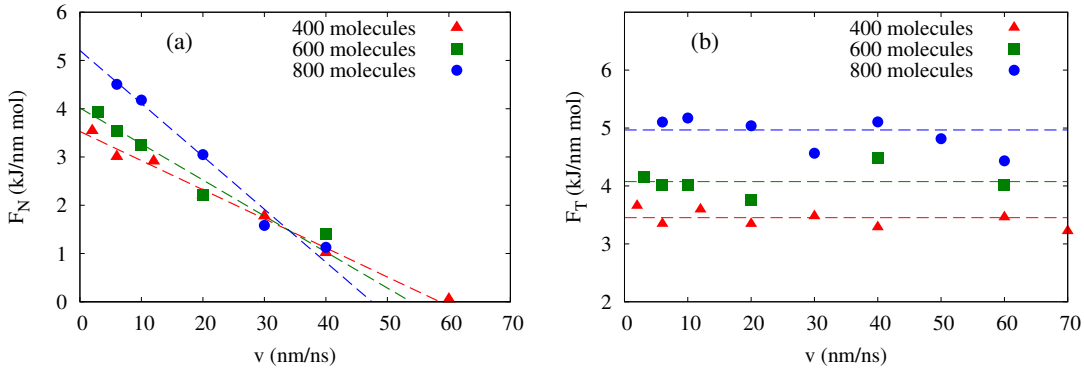

Figure 5.4: Net force and thermophoretic force for droplet sizes of 400(▲), 600(■) and 800(●) water molecules under an applied thermal gradient of 0.50 K/nm. (a) Computed Net force as a function of the velocity of the center of mass. The dashed lines are fits to the data. (b) Thermophoretic force as a function of the velocity of center of mass. The dashed lines are fits to the data. Source: Own elaboration.

for an imposed thermal gradient of 0.50 K/nm, higher thermophoretic forces are computed for longer water droplets, which shows that the magnitude of the thermophoretic force is directly related to the droplet size (or the droplet length due to the constant CNT cross-section). It should be noted that there is no consensus about the relation between the thermophoretic force and the size of the motile particle. For example, the thermophoretic force has been found to be dependent of particle size for distributions of particles in gas media [99, 268] and for particles inside CNTs [269]. On the other hand, a non-size dependence of the thermophoretic force has been found for solid particles in liquid media [93], oil droplets in liquid mixtures [270] and double-walled CNTs [250]. Here, to gain insight into the relationship between the thermophoretic force and the particular size of the water nanodroplet, Fig. 5.5 depicts the thermophoretic force as a function of the thermal gradient for droplets consisting of 400, 600 and 800 water molecules. The results indicate that the magnitude of the thermophoretic force acting on the droplet is directly related to both the magnitude of the imposed thermal gradient and the particular length of the droplet. Therefore, in line with previous studies [107,110,111], we infer that the thermophoretic force acting on the droplet is generated by the net current of phonons induced by the imposed thermal gradient, i.e., the rectified thermal vibrations of the carbon atoms provide the effective force to drive the water droplet through the CNT. Nevertheless, we notice further investigation is required to find the precise relationship between the interfacial phonon scattering dynamics and the thermophoretic force acting on nanodroplets confined in CNTs. We believe that this investigation provides deeper understanding of liquid transport driven by temperature gradients in nanodevices and will be useful for the development of nanofluidic applications.

5.4 Conclusions

In summary, by using molecular dynamics we studied in detail the interplay between thermophoretic and friction forces which govern the thermophoretic transport of water nanodroplets through CNTs. The results indicate that the thermophoretic force is not velocity dependent while the friction force increases linearly with the droplet speed. Moreover, we find that the magnitude of the thermophoretic force is determined by the imposed thermal gradient and the

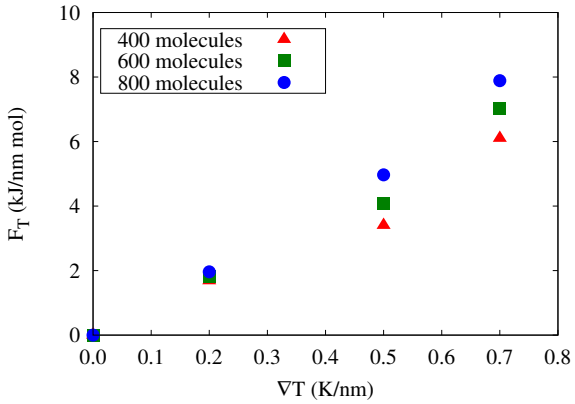

Figure 5.5: Thermophoretic force as a function of the thermal gradient for droplet sizes of 400 (▲), 600 (■) and 800 (●) water molecules. Source: Own elaboration.

particular length of the droplet. In general, the thermophoretic motion of a nanodroplet exhibits two kinetic regimes: (i) an initial regime wherein the droplet moves with decreasing acceleration, i.e., the friction force is linearly proportional to the droplet velocity whereas the thermophoretic force has a constant value defined by the thermal gradient and the droplet length, and (ii) a subsequent regime wherein the droplet moves at constant velocity due to balance between the thermophoretic force and the retarding friction force. The results presented in this thesis contribute to gain insight in the transport of liquids driven by thermal gradients and have practical implications for the design of CNT-based nanofluidic devices.

Chapter 6

Thermal Brownian Motor Concepts

6.1 Introduction

As discussed in section 2.3 of this thesis, in order to perform a useful work from the Brownian motion, two conditions need to be satisfied in the design of a device: (i) the breaking of spatial symmetry and (ii) the breaking of thermal equilibrium [25, 26, 118]. Therefore, in the quest to develop an apparatus that meet these conditions and provides useful work, three types of spatial asymmetries are proposed and studied in this thesis. The three spatial asymmetry concepts for thermal Brownian motors are shown in Fig. 6.1. For all these concepts, the thermal symmetry is broken by applying two different temperatures at particular locations along the device.

In this Chapter, the Brownian motor concepts of Fig. 6.1.a and 6.1.b are discussed, whereas in Chapter 7 a full description and analysis of the third concept (Fig. 6.1.c) is presented. The Brownian motors proposed in this thesis are based in carbon nanotubes and the fluid to be transported is water. Due to the ultrasmoothness of the CNT walls [247, 271] and their high thermal conductivity [244], CNTs arise as the perfect candidate of a Brownian motor device for water transport.

The concept of conical junction connecting two carbon nanotubes of different cross section has been theoretically studied [272–274] and experimentally fabricated [275, 276]. Since then, the concept of conical junction between carbon nanotubes has served as inspiration for different nanotechnological applications [273, 277–280]. Carbon nanotubes capsules have also been investigated in the last decade [281–283], and have been used for linear motors with an outer CNT [252, 284]. A description and analysis of the Brownian motor concepts of Fig. 6.1.a and 6.1.b are presented in the following sections.

6.2 Methodology

The simulations of the Brownian Motors are performed using the molecular dynamic package FASTTUBE [139]. The equations of motion are integrated in time using the leapfrog scheme with a time step of 2 fs. All the Brownian motor designs are simulated in an orthorhombic box with periodic boundary conditions in the axial direction of the CNTs and free space conditions in the radial direction. The carbon-carbon intramolecular interactions of the CNT are described by a Morse bond, a harmonic cosine of the bending angle, and a torsion potential [20,110,139]. For the carbon-carbon intermolecular interaction between the capsule and the outer CNT (Fig. 6.1.b), a Lennard-Jones potential with parameters of ϵ_{CC}= 0.4396 kJ/mol and σ_{CC}= 0.3851 nm is im-

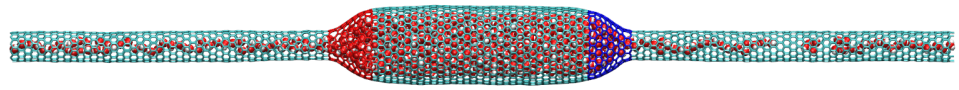

(a)

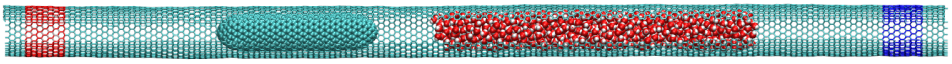

(b)

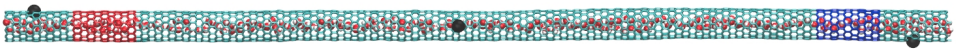

(c)

Figure 6.1: Representations of the thermal Brownian motors proposed in this thesis wherein each case makes use of a different type of spatial asymmetry. The thermal symmetry in all the cases is broken by applying two different temperatures as depicted by the red zone (high temperature) and the blue zone (low temperature) on each case. (a) Conic junction concept. In this device, the momentum transfer in the high temperature zone is expected to be higher than the momentum transfer in the low temperature zone. In this example, two carbon nanotubes (CNTs) with chiralities of (12,0) and (32,0) are joined by a conical junction. (b) Straight CNT with an inner CNT capsule and a portion of fluid. (c) Straight CNT filled with water and three fixed points (black dots) along the CNT. This last concept is fully discussed in Chapter 7. Source: Own elaboration.

plemented to describe the van der Waals interactions [20, 252]. Water is modeled by the rigid SPC/E model [133] and the water-CNT interactions are described by a 12-6 LJ potential calibrated for a 81° contact angle [20, 148]. The van der Waals and Coulomb interactions are truncated at 1 nm, while the Coulomb potential is smoothed to ensure energy conservation (see section 3.2.3) [20, 139]. For further details of the potentials, the reader is referred to Zambrano et al. [20].

In order to break the thermal symmetry of the system, two temperatures are imposed at different locations on the CNT. To achieve this, two Berendsen thermostats [154] are applied to the carbon atoms in the heated zones as depicted in Fig. 6.1, where the high temperature thermostat is applied to the carbon atoms in the red zone and the low temperature thermostat is applied to the carbon atoms in the blue zone. It is important to note that the thermostats are not applied to the water molecules during the nonequilibrium molecular dynamics simulations.

The conical junctions fabricated in this work, as the one depicted in Fig. 6.1.a, are computationally created by introducing pentagon and heptagon carbon rings as defects in the honeycomb lattice, as can be seen in detail in Figure 6.2.a. The pentagons and heptagons in cone-like carbon nanotubes were first observed by Iijima et al. in 1992 [285] by means of transmission electron microscopy. These defects are related with the pentagons and heptagons found in fullerenes or buckyballs, as pointed out by Iijima et al. [285]. The conical junctions created in this work are based in the investigation of Saito et al. [272] who used a projection method from a graphene sheet by following the chiral angles of the CNTs. The work of Saito et al. [272] was replicated in the investigations of Hanasaki et al. [277] and Wu & Li. [273], which also served as inspiration in

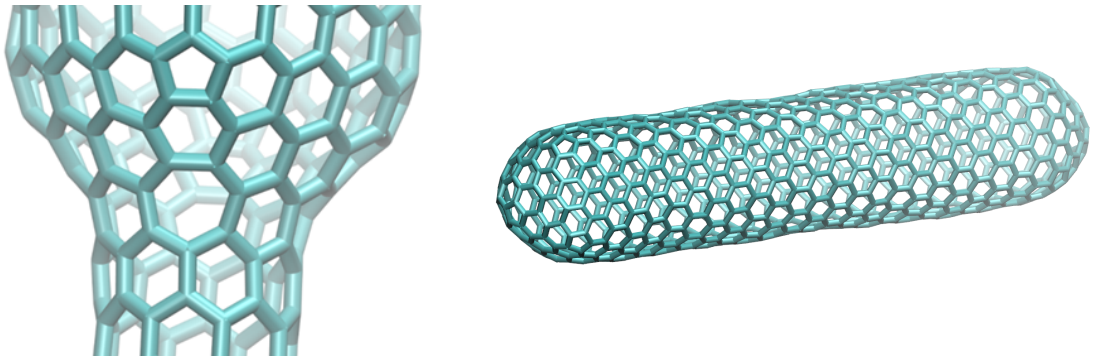

(a) (b)

Figure 6.2: (a) Representation of a conic junction of two CNTs with chiralities of (8,0) and (12,0). The pentagon and heptagon defects are introduced to connect two CNTs. (b) Representation of the CNT capsule used in the Brownian motor concept depicted in Fig. 6.1.b. Source: Own elaboration.

the fabrication of our conical junctions. Similarly, the CNT capsule used in the Brownian motor concept depicted in Fig. 6.1.b also includes the pentagons and heptagons defects, following the fullerene concept [286]. The capsule presented in this work (see Figure 6.2.b) consists of a central CNT with chirality of (16,0) and the caps corresponding to the half of a C_{188} fullerene. The total length of the capsule is 6 nm and the diameter is 1.25 nm.

The introduction of pentagons and heptagon defects in carbon nanotubes induce a decrease in the thermal conductivity locally [274, 287]. Likewise, a conical junction between two CNTs also decrease the thermal conductivity locally [274, 288]. Therefore, in order to avoid any drawback in the functioning of the thermal Brownian motor, the thermostats are applied in the carbon atoms of the conic junctions, as shown in Fig. 6.1.a.

6.3 Results and discussion

6.3.1 Spatial asymmetry by conic junctions

The first spatial asymmetry concept to be analyzed for a Brownian motor is depicted in Fig. 6.1.a. In this device, the spatial symmetry is broken by changing the cross section of a straight CNT and joining two CNTs of different diameters. The created conic junction imposes a diagonal interface connecting the two CNTs, similarly to a curved interface of a liquid drop in a hydrophobic pore or like the caps of a CNT capsule. The application of a thermal gradient (i.e. thermal asymmetry) would induce a higher momentum transfer between the heated carbons and the water molecules in the high temperature zone (red junction in Fig. 6.1.a) compared to the zone of low temperature (blue junction in Fig. 6.1.a), producing a rectified and continuous water flow, hypothetically. In order to study this Brownian motor concept, three devices with different combinations of diameters are analyzed, which are summarized in Table 6.1. It should be noted that all the devices are completely filled with water.

In order to evaluate the feasibility of this water pump on its extreme working condition, the highest possible temperature difference considering the phase change of water is applied in the three studied cases [289]. The imposed temperatures are 400 K in the high temperature zone and 260 K in the low temperature zone, producing different thermal gradients in the studied

Table 6.1: Brownian motor concept with conical junctions. In these devices the spatial asimmetry is imposed by breaking the cross section and joining two CNTs of different diameters. Source: Own elaboration.

Case	CNT chiralities	Diameters (nm)	Temperatures (K)	Thermal Gradient (K/nm)	Mean velocity (m/s)
1	(40,0) - (24,0)	3.13 - 1.88	400 - 260	5.8	0.0
2	(32,0) - (20,0)	2.50 - 1.57	400 - 260	5.2	0.0
3	(32,0) - (12,0)	2.50 - 0.94	400 - 260	5.8	0.0

configurations (see Table 6.1 and Fig. 6.3.b). The simulation time of the cases presented in Table 6.1 is 40 ns for each case. However, as indicated in Table 6.1, none of the three cases studied produce a rectified water flow. The radial velocity profile and the axial temperature profile for case 1 in Table 6.1 are shown in Fig. 6.3. From the radial velocity profile (Fig. 6.3.c) it is observed that the proposed Brownian motor does not produce a water flow velocity. Similar profiles are obtained for cases 2 and 3 of Table 6.1.

Several causes are suggested in order to explain the failure of the proposed Brownian motor; however, a further study is required to fully understand the non-functioning of this device. The first cause is attributed to the thermal resistance between carbons and water (Kapitza effect) [290], which significantly reduces the heat exchange between them, thus reducing the momentum transfer between the solid wall and the fluid. The second cause is attributed to the hydrodynamic resistance inherent in a conical outlet or contraction [4, 291], neglecting any small thrust produced in the high temperature zone, if any. Overcoming the last suggested cause is a dead end. For example, if the diameter difference between the CNTs is increased, in order to increase the momentum transfer in the hot side, that change in the diameter difference results in an increase in the hydrodynamic resistance at the conical outlet [4, 291]. These combined causes lead to an energy exchange between the carbon atoms of the CNT and the water molecules as a thermal exchange only, making any rectification of the water movement impossible.

6.3.2 Spatial asymmetry by an inner capsule

The second spatial asymmetry concept for a Brownian motor to be discussed is depicted in Fig. 6.1.b. The operating mechanism of this device consists in the use of an internal CNT capsule [284] to drive the confined fluid similar to a piston. Thereby, under an applied thermal gradient in the outer CNT (thermal asymmetry), the inner capsule will be moved with a thermophoretic motion [252], pushing the portion of water continuously. In this case the spatial asymmetry of this Brownian motor is found in the interface between the solid caps of the capsule and the solid wall of the CNT.

In the device studied here, an outer CNT of 38 nm long with a chiral vector of (25,0) is used. The inner capsule consists of a central CNT with a chiral vector of (16,0) and caps corresponding to the half of a C_{188} fullerene, obtaining a capsule with a total length of 6 nm and a diameter of 1.25 nm (see Figure 6.2.b).

First, we evaluate the Brownian motor concept without water, testing the feasibility of the thermophoretic motion of the capsule following the investigation of Zambrano et al. [252]. Unlike the linear motor proposed by Zambrano et al. [252], the present capsule includes caps in both ends, as shown in Figure 6.2.b. In order to track the motion of the capsule, we compute the

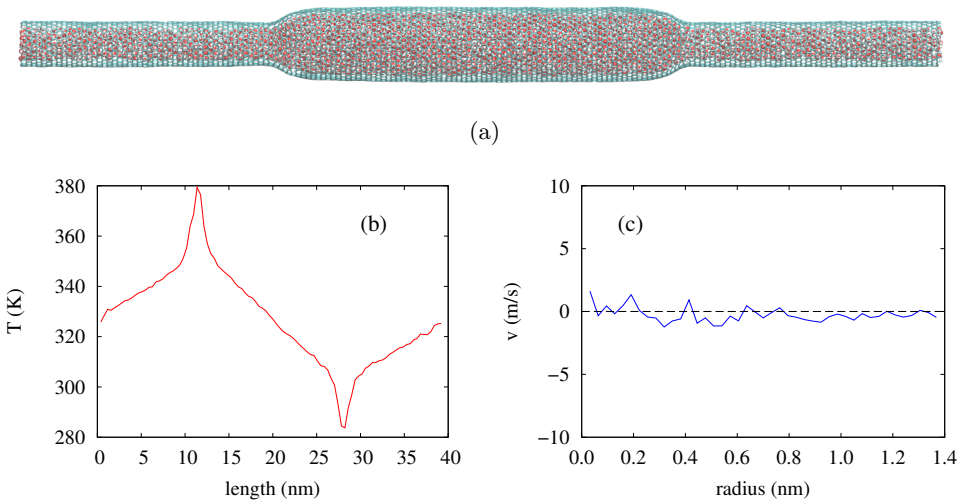

Figure 6.3: Simulation of the Brownian motor with conical junctions consisting of CNTs with chiralities of (40,0) and (24,0), corresponding to case 1 in Table 6.1. (a) Representation of the device. (b) Temperature profile along the device. (c) Radial velocity profile of water inside the device. Source: Own elaboration.

center of mass (CoM) position of the capsule in time. By applying temperatures of 340 K and 260 K at the respective ends of the outer CNT (see Fig. 6.4.b), we observe a direct motion of the capsule as shown in Fig. 6.4.c. After 20 ps of thermophoretic motion, the capsule undergoes a movement with constant velocity of 170 m/s, wherein the thermophoretic force balances the friction force [252] (see also Chapter 5). The magnitude of the thermophoretic velocity is in the same order of the velocities reported by Zambrano et al. [252].

As a next step, the outer CNT was filled with water molecules in order to test the Brownian motor (see Table 6.2). By introducing 1500 water molecules and applying temperatures of 350 K and 260 K at the respective ends (case 3 in Table 6.2), we do not observe any direct motion of the capsule therefore, a rectified motion of the fluid was not observed. Next, by assuming that the origin of the non-functioning of this device is due to the lack of free space inside the CNT, the amount of fluid was reduced by half. Thereby, by introducing 750 water molecules and applying temperatures of 350 K and 260 K (case 2 in Table 6.2), a rectified motion of water was not observed. Nevertheless, in this case we observe a very short thermophoretic motion of the capsule which collides with the fluid. However, the amount of momentum gained by the capsule was not enough to push the fluid. Considering that the capsule and water droplets can be transported by thermal gradients [20, 252, 256], it is expected that this system will work using longer CNTs. However, the hypothesis of a continuous water pump driven by the thermophoretic energy gained by the capsule alone is not feasible.

6.4 Conclusions

Using MD simulations, we have investigated the feasibility of two thermal Brownian motor concepts based in CNTs for water transport. The Brownian motor concepts are based in the Smoluchowski-Feynamn ratchet, wherein the thermal symmetry is broken by imposing a thermal gradient. The first thermal Brownian motor consist of two CNTs of different diameters joined

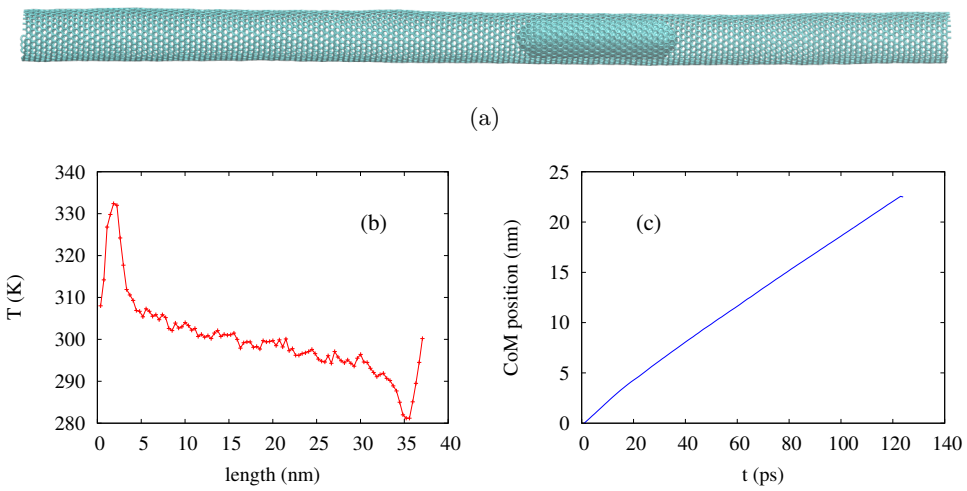

Figure 6.4: Simulation of the linear motor based in the work by Zambrano et al. [252] consisting of a confined CNT capsule and an outer CNT with zigzag chirality of (25,0) and 38 nm long. This simulation corresponds to case 1 in Table 6.2. This simulation does not have water and the applied thermal gradient is ca. 1.6 K/nm. The capsule is described in the methodology section, Figure 6.2.b. (a) Representation of the linear motor with the capsule. (b) Temperature profile along the outer CNT. (c) Center of mass position of the capsule during the thermophoretic motion. Source: Own elaboration.

Table 6.2: Resume of the simulated cases for the Brownian motor concept with an inner capsule. In this device, the capsule is moved by the action of the thermophoretic force, with the goal of driving the portion of water in front of it. Source: Own elaboration.

Case	N° of water molecules	Temperatures (K)	Thermal gradient (K/nm)	CoM velocity (m/s)
1	0	340 - 260	1.6	170.0 (capsule)
2	750	350 - 260	2.2	0.0
3	1500	350 - 260	2.2	0.0

by a conic junction. In this device, the spatial symmetry is broken by changing the cross section of a straight CNT. The second thermal Brownian motor concept is based in the introduction of an inner capsule that works as a piston imparting motion to the fluid. In this device, the capsule is moved by the action of the thermophoretic force. By evaluating these Brownian motor concepts on their extreme conditions, it was found that none of these devices work as a rectifier of water motion. Further investigation is required to fully understand the non-functioning of these devices.

Chapter 7

Carbon Nanotubes as Thermally Induced Water Pumps

Parts of this chapter have been published in: Elton Oyarzua, Jens H. Walther, Constantine M. Megaridis, Petros Koumoutsakos and Harvey A. Zambrano. Carbon Nanotubes as Thermally Induced Water Pumps. *ACS Nano*, 2017, 11(10), 9997-10002.

7.1 Introduction

Recent developments in nanotechnology are enabling the fabrication of devices such as nano Lab-On-a-Chip (LOC) units [190, 292]. These integrated systems hold the promise of combining in a single nanochip and with molecular level resolution, the complete sequence of all technical stages found in traditional clinical laboratories. Nanochannels are an essential part of such systems, as conduits are needed to integrate the functional network components. The development of nanoscale LOC (nLOC) units relies on the rational design of nanochannels conducting the fluids and require a pumping mechanism for driving the flows. Flows in nanoconfinement are known to behave differently than flows at the macro- and micro-scale due to dramatic increases of the surface-to-volume ratio. It has been reported that water transport through carbon nanotubes is one to five orders of magnitude faster than predicted by continuum models [17, 245, 246]. In addition to inducing fast water flow, CNTs possess extraordinary mechanical, electronic, thermal and chemical properties, [149] making them attractive candidates as conduits of nanofluidic devices. At the same time, the mechanisms required to drive water flow in nanoconfined geometries remain the subject of intense research [293]. It has been reported that large pressure gradients are required to induce flow in CNT based nanomembranes, [17,294] while electrokinetic flows rely on single-file transport of water molecules in a CNT [99, 295, 296] and capillarity is not a means to deliver continuous flow. Finally, due to the ultra-smoothness of the CNT walls [247] and their high thermal conductivity [244], mass transport inside CNTs (as driven by imposed thermal gradients) has received considerable attention over the past decade [20, 21, 106, 107, 111, 249–255].

In this chapter, molecular dynamics (MD) simulations are employed to investigate the continuous flow of water inside a CNT, as driven by an imposed constant thermal gradient. We propose a nanomotor based on the thermal Brownian ratchet concept [297] to enable fast and continuous water flow through a nanoconduit. The device consists of a single-wall CNT filled with water. The CNT is fixed at three points, as shown in Figure 7.1, with the central fixed point working as a pivot. Two heating zones near the ends impose a thermal gradient along the

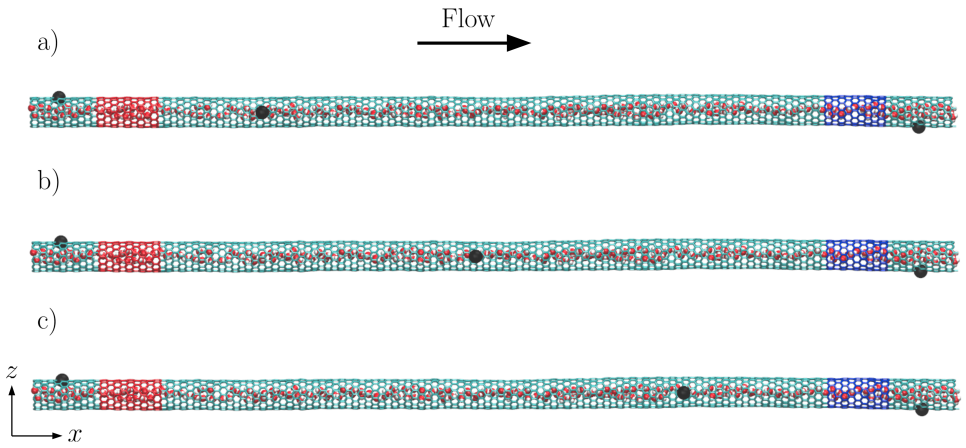

Figure 7.1: Illustration of the different CNT configurations studied in this work. The black filled circles indicate the fixed points along each CNT. The red and blue zones represent the heated sections of the CNT. The lengths of the CNTs were either 30 nm or 60 nm. Source: Own elaboration.

CNT. The spatial symmetry of the system is broken by the specific position of the fixed points, as depicted in Figure 7.1. The thermal excitation of the carbon atoms induces oscillations along the CNT with peak amplitudes directly associated to the local temperature. We find that differences in oscillation amplitudes between the higher and lower temperature zones lead to a net water flow opposite to the thermal gradient (along declining temperature). Using this configuration, we systematically investigate the flow dependence on the magnitude of the imposed thermal gradient and the influence of the position of the central fixed point, which breaks the symmetry of the system.

7.2 Methods

To study the rectified flow of water driven by thermal gradients inside the CNT, we perform a series of all-atom MD simulations. The simulations are performed using the MD package FASTTUBE [139]. The equations of motion are integrated in time using the leapfrog scheme with a time step of 2 fs. All simulations are conducted in an orthorhombic box with periodic boundary conditions in the axial direction of the CNT and free space conditions in the radial direction. The carbon-carbon intramolecular interactions of the CNT are described by a Morse bond, a harmonic cosine of the bending angle, and a torsion potential [20, 110, 139]. Water is modeled by the rigid SPC/E model [133] and the water-CNT interactions are described by a 12-6 Lennard-Jones potential calibrated for a 81° contact angle [20, 148]. The van der Waals and Coulomb interactions are truncated at 1 nm, while the Coulomb potential is smoothed to ensure energy conservation [20, 139]. The MD package and the force fields have been extensively validated in previous works [20, 106, 110, 139, 148, 252, 262]. For details of the potentials, we refer the reader to Zambrano et al. [20]

We first equilibrate the system at 300 K in the NVT ensemble for 0.5 ns. Then, using nonequilibrium molecular dynamics (NEMD) simulations, we impose a thermal gradient along the CNT axis. The thermal gradient is imposed by applying two different temperatures at the respective

ends of the CNT, as depicted in Figure 7.1. Specifically, the carbon atoms in each heated zone are coupled to Berendsen thermostats [154]. It is important to note that the water molecules are not connected to the thermostat in the NEMD simulations. Previous studies have demonstrated that the Berendsen thermostat is suitable to impose proper nonequilibrium conditions [161,260], and is optimal for mechanical responses at relatively constant temperature during CNT compression [261]. In order to remove spurious effects of the thermostat, the mean velocity of the heated carbon atoms is subtracted, and subsequently added, when the thermostat is applied. We conduct the NEMD simulations during 100 ns to reduce thermal noise, and ensure a steady water flow rate. From the atomic trajectories, the CNT vibrations are analyzed by a FFT algorithm, measuring the amplitudes and frequencies of the different vibrational modes. This FFT method was previously proposed by Pine et al. [298] Further details on the simulations and FFT analysis are presented in Appendix C.1 and C.4.

7.3 Results and discussion

We study first a reference case, which consists of a CNT with fixed points at its two ends and its geometric center, as depicted in Figure 7.1b. The fixed carbon in the middle restricts the position of the CNT without significantly altering the temperature profile along the CNT (see Appendix C.3). Here, we use a 30 nm long zig-zag (12,0) CNT, completely filled with water. The CNT is subjected to axial thermal gradients of either 1.6, 2.3 or 3.3 K/nm. Upon imposing a thermal gradient, we observe the water molecules inside the CNT flow toward the low-temperature zone. Furthermore, by systematically increasing the imposed thermal gradient, we note that the water axial velocity (likewise flow rate) increase linearly, as shown in Figure 7.2a, with a rate following

$$v = -1.49\nabla T \tag{7.1}$$

which is consistent with prior studies of thermophoresis in CNTs. [20, 106, 252]

The computed net water flow in the CNT is attributed to the thermal oscillations induced in the CNT according to the imposed thermal gradient. We find that the particular position of the central fixed point is key to rectify the water motion in a preferential direction, which results in a constant net flow of water. In order to quantify the oscillations of the system, we perform a fast Fourier transform (FFT) analysis to determine the amplitudes and frequencies of the thermally-induced vibrational modes of the CNTs. In particular, for the system illustrated in Figure 7.1b, we perform the FFT analysis at a point located between the left fixed point and the center point of the CNT, i.e. 7 nm from the left periodic border, at different imposed thermal gradients. The amplitude values of the first four vibrational modes as functions of the imposed thermal gradients are shown in Figure 7.2b. We note that the frequencies of the vibrational modes are associated directly with the size of the system, displaying no relation to the imposed thermal gradients. For example, for the 30 nm-long CNT filled with water, the first four vibrational modes have frequencies of 0.0925, 0.2100, 0.3750 and 0.4825 THz respectively. Figure 7.2b shows that an increase in the imposed thermal gradient results in larger amplitudes in the vibrational mode 1. For modes 2, 3 and 4 no change is observed when different thermal gradients are imposed. Therefore, as a thermal gradient is imposed, the induced flow rates depend on the amplitude of the thermal oscillations exclusively in vibrational mode 1. Indeed, the amplitudes in vibrational mode 1 along the CNT for different imposed thermal gradients are shown in Figure 7.2c, which shows that the high-temperature zone (left) acquires larger oscillations compared to the low-temperature zone (right) for all imposed thermal gradients. Specifically, our results indicate

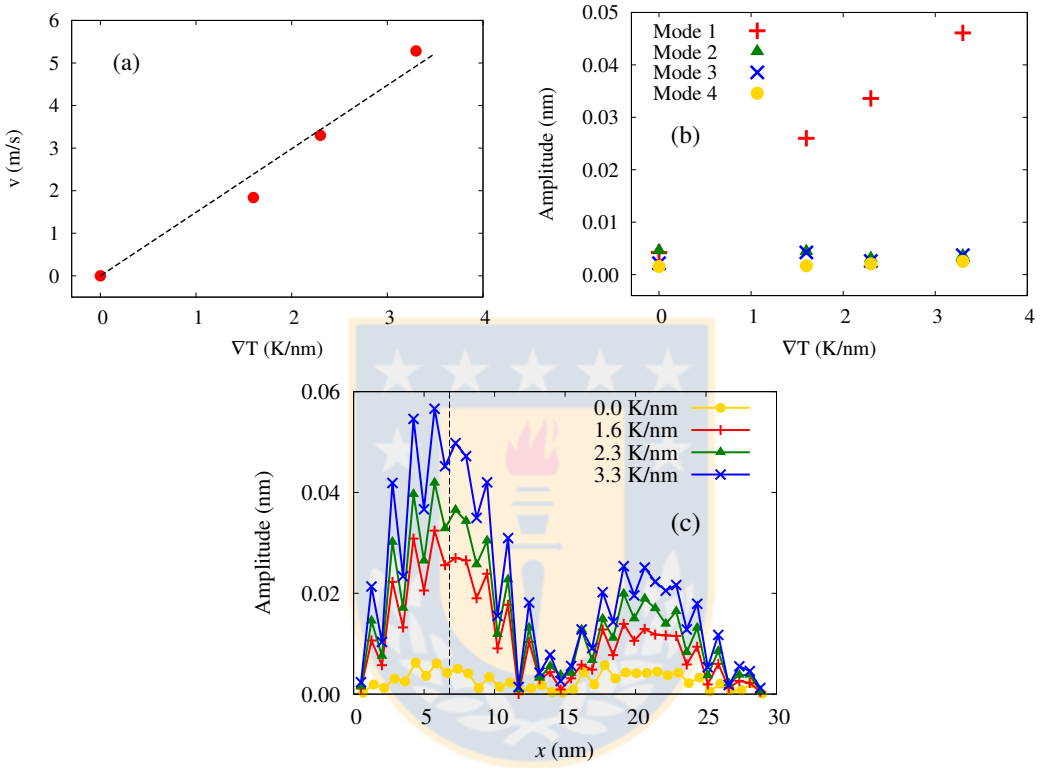

Figure 7.2: Mean velocities and FFT analysis for the 30 nm-long (12,0) CNT with fixed points as shown in Figure 7.1b. **(a)** Mean flow velocities of water for imposed thermal gradients of 0, 1.6, 2.3 and 3.3 K/nm. The dashed line corresponds to a linear fit of the data, under the condition $v_{(\nabla T=0)} = 0$ m/s. **(b)** Amplitudes of the vibrational modes 1–4 computed at 7 nm from the left end of the CNT. This position is depicted by the vertical dashed line in Figure 7.2c. **(c)** Amplitudes measured for the first mode at three different imposed thermal gradients along the axial direction of the CNT. The zero thermal gradient case (330 K) is also shown in this figure. Source: Own elaboration.

that the water flow in the CNT is induced by a continuous whip-like effect generated by the difference in the oscillations of the CNT in the two heated zones. Moreover, as the imposed thermal gradient is increased, the amplitude of the oscillations increases, inducing higher flow rates.

Previous studies [299,300] have shown that a net flow can be induced inside a CNT imposing traveling waves. In fact, Insepov et al. [299] imposed Rayleigh traveling waves in a single-walled CNT to transport gas. They observed a time-dependent flow rate with time decay. Likewise, Qiu et al. [300] noted that by applying a periodic force in a cantilever CNT, a water net flow was produced. Moreover, at higher applied forces, greater amplitudes at the free end of the CNT were observed, leading to higher water flow rates. In terms of performance, our Thermal Brownian Motor (TBM) converts thermal energy directly into water flow with an efficiency of ca. 0.2%, similar to the nanopump proposed by Qiu et al. [300] or the nanomotor studied by Hou et al. [250] and previously studied Brownian motors [116, 122, 301]. The calculation details of the efficiency associated with our TBM/CNT pump are described in Appendix C.6. Furthermore, we propose that the mechanism reported in the present study corresponds to a thermally-rectified motion, as previously observed by Becton and Wang [108], who showed that a graphene nanoribbon mounted on a thermalized graphene sheet moved toward the low-temperature zone of the sheet. We infer that the mechanism driving the ribbon on the graphene sheet was the thermally-induced oscillations on the graphene sheet generated by the imposed temperature gradient.

In order to gain insight into the mechanism driving the water flow in the CNT and investigate further the role of the fixed central point, we vary systematically its position as shown in Figure 7.1. We also conduct simulations for 60 nm-long (12,0) CNTs filled with water under an imposed thermal gradient of 2 K/nm and positions of the fixed middle point as shown in Figure 7.1. Further details of the distances and dimensions used in each simulation are provided in the Table C.1 in Appendix C. For the three different cases, velocity profiles with radial position are shown in Figure 7.3a. The position of the fixed middle point only slightly modifies the water flow rate. For example, for case (a) (configuration shown in Figure 7.1a), a lower flow rate is observed. This confirms that the axial flow rate is not exclusively thermal-gradient dependent; there is also strong dependence on the vibrational behavior in the CNT. In order to quantify the vibrational modes for the different cases, a FFT analysis was performed.

The amplitudes measured for the three cases and the vibrational modes in the CNT are shown in Figure 7.3b, c and d. These figures show that the position of the middle point strongly affects the amplitudes of the first three vibrational modes under the same thermal gradient. Considering the reference case, i.e., the CNT with fixed end points and a fixed point in the middle, the corresponding amplitudes of the three vibrational modes are shown in Figure 7.3c. From this figure, we observe the same behavior as in Figure 7.2c, i.e., a direct impact of the thermal gradient on mode 1, with a greater amplitude in the high-temperature zone compared to the low-temperature zone. On the other hand, mode 2 is not affected by the imposed gradient, while mode 3 shows a slight increase in the amplitudes on the high-temperature zone relative to the low-temperature zone. In the case with the lowest flow rate measured, i.e. case (a), the amplitudes are presented in Figure 7.3b. This figure shows how the vibrational modes of the CNT are distorted with respect to the case with the central fixed point (Figure 7.3c); here the CNT acquires a greater freedom of movement in the low-temperature zone, leading to an increase of the amplitude of mode 1 in this zone. However, due to the particular direction of the flow, it follows that the third mode does drive the fluid. In fact, the effect of mode 3 on driving the fluid is the most significant when the CNT is restricted at 1/3 of its length. Here, the frequency of mode 3 is 0.065 THz, which is more than four times the frequency of mode 1 (0.015 Thz),

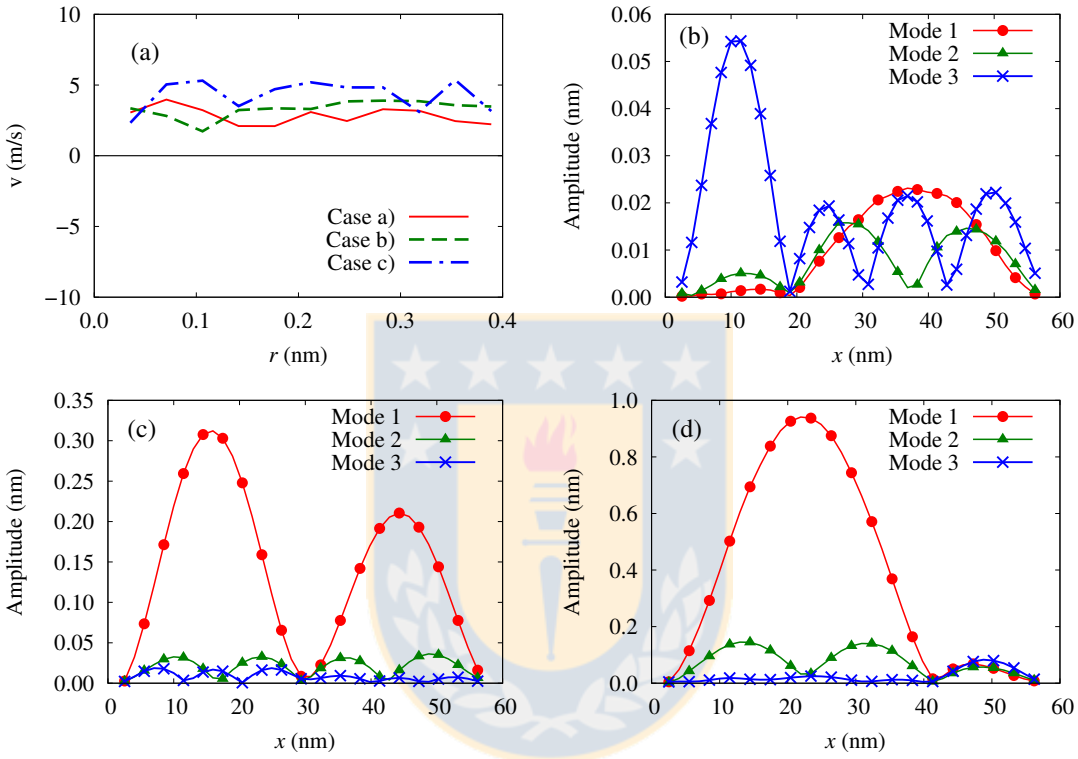

Figure 7.3: Velocity profiles and FFT analysis in a 60 nm-long (12,0) CNT with fixed points as shown in Figure 7.1a, b and c. All CNTs had an imposed thermal gradient of 2 K/nm. **(a)** Radial distribution of axial velocity for the three different cases of Figure 1 (case a, b, c respectively) with mean velocities of 2.8 m/s (red), 3.3 m/s (green) and 4.5 m/s (blue). **(b)** Amplitudes for vibrational modes 1–3 for CNT as shown in figure 7.1a (central fixed point at 1/3 of the length). **(c)** Amplitudes for vibrational modes 1–3 for CNT as shown in Figure 7.1b (central fixed point at half the length), and **(d)** Amplitudes for vibrational modes 1–3 for CNT as shown in Figure 7.1c (central fixed point at 2/3 of the length). Source: Own elaboration.

leading to oscillations with a higher frequency and amplitude in the high-temperature zone as compared to the oscillations in the low-temperature zone. Finally, the amplitudes measured in the case with higher flow rate, i.e. case (c), are depicted in Figure 7.3d. This figure shows how the amplitude of mode 1 is strongly increased, more than twice compared to the peak amplitude of the corresponding mode in Figure 7.3c. Similar to Figure 7.3b, modes 2 and 3 are distorted by modifying the central fixed point, leading to a greater amplitude in the high-temperature zone for mode 2, and in the low-temperature zone for mode 3. The results for the three cases, indicate that the water flow is driven by an association between the frequencies and amplitudes of "activated" vibrational modes [302] due to the particular fixed position of the point between the two ends. To confirm this driving mechanism, two additional cases of the 60 nm-long (12,0) CNT were simulated, with restrictions at 1/4 and 1/5 of the length, respectively. In both cases, a water flow with mean velocity of ca. 3.5 m/s was calculated. Moreover, in the high-temperature zone, a higher amplitude of mode 4 was computed for the case restricted at 1/4 length, and similarly, a higher amplitude of mode 5 was computed in the case restricted at 1/5 length (see Appendix C.4; Fig. C.7 and Fig. C.8). This indicates that the position of the pivotal fixed point with respect to the total length of the CNT determines the magnified harmonic vibrational mode driving the flow. Similar to the mechanism proposed by Qiu et al. [300], we infer that a centrifugal force is propelling the water molecules. In our device, the magnitude of the centrifugal force is a consequence of the amplitudes and the frequency of a specific vibrational mode induced by the imposed thermal gradient and the particular position of the fixed middle point.

The feasibility of inducing continuous water flow in a CNT by imposing an external temperature gradient has not been widely investigated. In a recent study, Zhao and Wu [21] showed that by keeping two reservoirs at different temperatures and connecting them with short aligned carbon nanotubes, net flow of water towards the low-temperature reservoir was observed. They reported significant higher flow rates for longer CNTs connecting the reservoirs, while keeping the end-to-end temperature difference constant (i.e. lower temperature gradient). This disagrees with the present results, since we compute lower flow rates for longer CNTs subjected to the same temperature difference (see Fig. C.9 in Appendix C.5). This discrepancy is mainly related to the different treatment of the carbon atoms in the simulations, while Zhao and Wu [21] imposed a harmonic restraining force to all the carbon atoms in the nanotube, in the present study, the nanotube vibrations are controlled without suppressing substantially the thermal oscillations of the nanotube. Additionally, the finite length of the CNT membrane in the study of Zhao and Wu [21] leads to a higher energy barrier at the entrance, which is not taken into account in the present study.

To further explore this TBM, we evaluated the thermal pumping for CNTs with different diameters. Simulations of water in CNTs with diameters of 1.4 nm and 2.0 nm, chirality vectors (18,0) and (26,0) respectively, were conducted. In both systems, a fixed thermal gradient of 3 K/nm was imposed along the CNTs. Water velocity profiles along the axial direction for the (18,0) and (26,0) CNTs are shown in Figure 7.4. For both cases, the water flow displays a plug-like velocity profile with mean velocity of ca. 3 m/s. It is interesting to note that the exhibited independence of flow velocity on CNT diameter indicates that the proposed pump configuration (Figure 7.1b) may be, in principle, scalable to larger diameters. However, further investigation is required to confirm this hypothesis.

We believe that the present results provide valuable insight in the field of nanofluidic devices and also open the door to potential practical exploitation of thermal gradients for driving flow in nanoconduits. It should be noted that large thermal gradients are used in this study in order to increase the signal-to-noise ratio in our simulations, allowing us to extract measurable flow

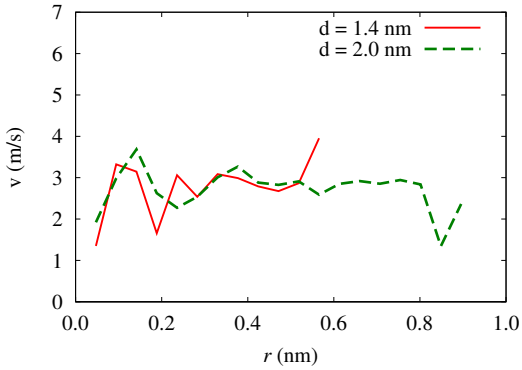

Figure 7.4: Radial distribution of axial velocity of water inside CNTs of 1.4 nm and 2.0 nm in diameter. The chiralities are (18,0) and (26,0), respectively. The applied thermal gradient is 3 K/nm in both cases. Source: Own elaboration.

data without requiring prohibitively-long simulation times. In fact, for practical applications in nanofluidic devices wherein the typical distances are in the order of hundreds of nanometers, the relatively high temperature differences required to impose such large gradients in the CNT conduits, could give rise to some concern about the boiling temperature of water. Nevertheless, recent studies have reported that water phase transitions under nanoconfinement may deviate from classical behavior [14,289]. Specifically, the temperature for liquid-vapor transition of water confined in CNTs with similar diameters used in the present study is substantially raised above 100 °C due to nanoconfinement. Therefore, we infer that if a net water flow can be produced imposing a gradient of 0.5 K/nm (see Figure C.15 in Appendix C.9) and assuming the boiling temperature is significantly higher inside the CNT then, the system proposed here could pump liquid water through CNTs with lengths of ca. 500 nm. Moreover, nanofabrication techniques currently allow the fabrication of ultrathin membranes connecting two reservoirs separated only by 100 nm [303]. This type of ultrathin membranes can be used in combination with vertically-oriented CNTs [304] for molecular sieving applications or for separation of analytes immersed in water solutions, wherein the flow is driven by thermal gradients, as in the present work.

7.4 Conclusions

Using MD simulations, we have investigated the capability of CNTs subjected to a thermal gradient, to sustain continuous and fast water transport in their interior. This study provides the basis for developing a thermal pump based on single-wall carbon nanotubes. The device is able to pump continuous flows with average velocity up to 5 m/s. The mechanisms driving the fluid flow are thermally-induced asymmetric oscillations along the CNT, which propel the fluid in a constant, whip-like motion. Flow rate control is achieved by the direction and magnitude of the imposed temperature gradient and by modifying the position of the pivotal fixed point along the CNT. The interplay between relative positions of the fixed points and the applied thermal gradient produce greater amplitudes in the high-temperature zone compared to the low-temperature zone for specific vibrational modes. We envision that CNTs with thermal gradients could assist the design of nano-chips that require fast water transport between their components.

Chapter 8

Conclusions

This thesis addresses the study of different physical transport mechanisms for driving water flow in nanoconduits, relevant to the performance and design of foreseeable technological applications. To perform the studies presented in this thesis, molecular dynamics simulations are conducted, which provide a complete description of the transport mechanisms with an atomistic detail.

In the first investigation presented in this thesis, the capillary filling of water in silica nanochannels is analyzed. This study confirms that the spontaneous imbibition follows a purely inviscid flow regime with constant velocity during the very first stage of imbibition. Thereafter, the capillary filling kinetics evolves to a developing flow where the capillary force is balanced by contributions from inertia and viscous drag losses. Additionally, a gas overpressure in front of the advancing meniscus is predicted. The results provide a description of the dynamics behavior of capillary filling relevant for the design of potential applications based in silica nanoslits Furthermore, the results suggest that the accumulative effect of the gas viscous friction and the pressurization on the meniscus could be part of the explanation for the slower than expected capillary filling rates.

Additionally, the kinetics associated in the thermophoretic motion of water droplets in carbon nanotubes is also studied within this thesis. The results indicate that the thermophoretic force is not velocity dependent while the friction force increases linearly with the droplet speed. Moreover, we find that the magnitude of the thermophoretic force is determined by the imposed thermal gradient and the particular length of the droplet. These findings provide a deeper understanding of liquid transport driven by thermal gradients in nanoconfined geometries, contributing to the practical design of CNT-based nanofluidic devices. Finally, the capability of CNTs subjected to a thermal gradient to sustain continuous and fast water transport is investigated. To accomplish, three thermal Brownian motors are proposed, corresponding to three different spatial asymmetries concepts. Among the proposed devices, just one concept is able to pump a continuous water flow. The mechanisms driving the fluid flow are thermally-induced asymmetric oscillations along the CNT, which propel the fluid in a constant whip-like motion. The results of this investigation indicate that the CNT-based thermal motor can provide a controllable and robust system for delivery of continuous water flow with potential applications in integrated nanofluidic devices.

The work developed in this thesis has presented results that contribute to the fundamental knowledge of the transport of fluids in nanoscopic devices. However, in the development of this thesis, and as all scientific progress, new inquires were appearing, that due to the limited time of this project, they were not answered. Thus leaving the door open to new studies in the area of fluid transport, which could potentially address some of these questions. For example, because

of the proposed thermal motor in Chapter 7 displays a very low efficiency, improvements can be made in order to increase the efficiency of the pump. In this sense, considering the very high conductivity of the carbon nanotubes, it is expected that most of the heat is flowing along the walls of the carbon nanotube and only an small amount is transformed into mechanical work to the fluid. Hence, improvements could be focused on testing nanotubes of other materials with lower conductivity or by imposing some kind of insulation along the carbon nanotubes. Furthermore, the investigation of the interplay between the water-solid friction and the efficiency of this pump is also required. Additionally, in terms of the use of thermal gradient in water-solid system, there is a lack of knowledge regarding the impact of the use of thermal gradients in the static and dynamic properties of fluids, i.e, in the water-solid friction. In the context of capillary action, due to the complexity of the phenomenon of capillarity, several assumptions were made in order to reduce the computational cost of that study. Therefore, it is expected in the near future to perform new studies that account the complex relation between the species involved in the capillary problem, such as the complex silica-water interaction and its dynamic in capillarity or the water and air potential that account the induced dipoles/quadrupoles.

Finally, with this thesis I wish to contribute to the advance of the understanding of some fundamental concepts necessary for the development and design of nanofluidic devices and to encourage the future exploitation of molecular dynamics simulations for the investigation of thermally driven phenomena related with the development of nanodevices.

Appendix A

Supporting material for "Early regimes of water capillary flow in slit silica nanochannels" (Chapter 4)

A.1 Transition Regime

Following the discussion about Figure 4.2A in Chapter 4, the imbibition length as a function of time for a channel with heights of 6 and 8 nm are presented here in Figure A.1. The dashed line represents the constant velocity regime during the early stage of imbibition. As discussed in Chapter 4, the results indicate that in the beginning of the imbibition, the capillary front moves at constant velocity. Subsequently, the filling kinetics departs from being linear in time and follows a visco-inertial regime (eqn. 4.2) depicted by the blue solid line.

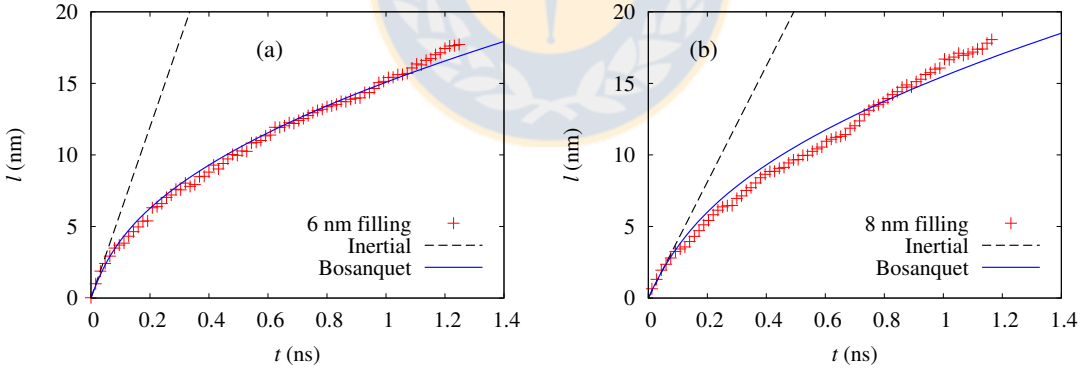

Figure A.1: Position of capillary front as a function of time for channels heights of 6 nm (a) and 8 nm (b). The dashed line depicts the linear regime while the solid blue line depicts the visco-inertial regime. Source: Own elaboration.

A.2 Inertial regime

As discussed in Chapter 4, a capillary flow with constant velocity for all the channels is observed at very short times (Figure 4.2.b of Chapter 4). The inertial velocities during the water uptake are shown in Figure A.2 in logarithmic scale, along with the theoretical velocity according to eqn. 4.3. The same velocities are presented in Table A.1.

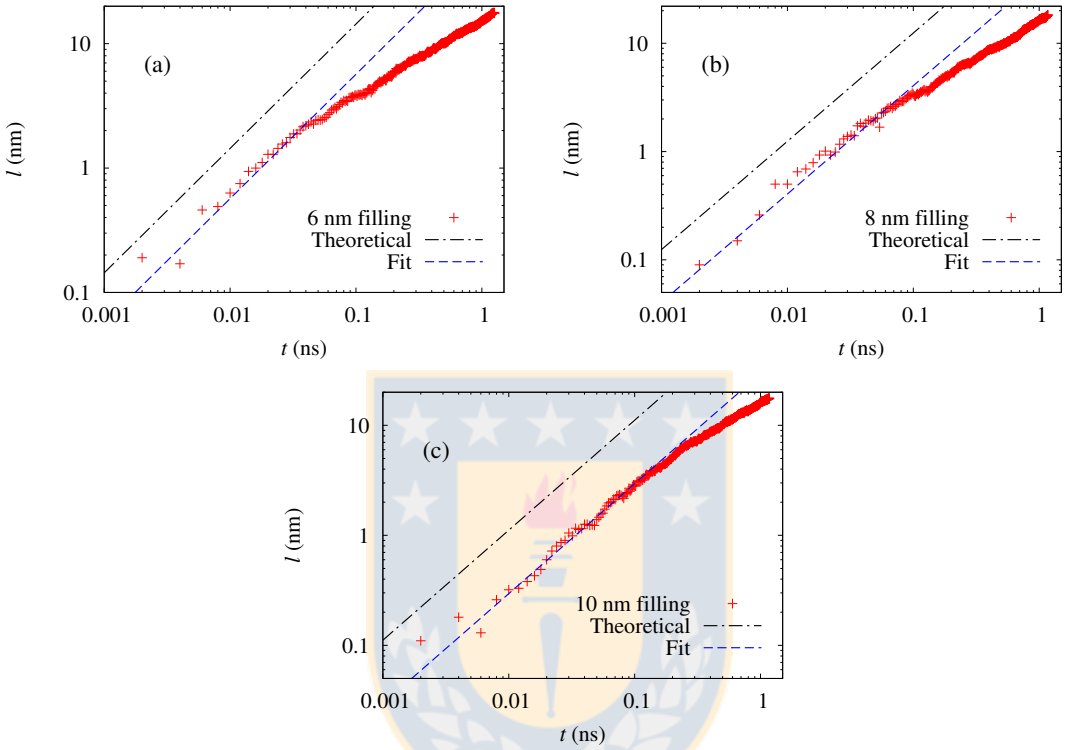

Figure A.2: Position of capillary front as a function of time at vacuum for channel heights of 6 nm (a), 8 nm (b) and 10 nm (c). The dashed-dotted line is the theoretical value from eqn. 4.3 and the dashed blue line is the linear fit solution at short times of the Bosanquet equation (eqn. 4.2). The plots are in logarithmic scale. Source: Own elaboration.

Table A.1: Inertial velocities for channels of 6, 8 and 10 nm. The theoretical value is computed from eqn. 4.3 and the fitted value is depicted in Figure A.2. Source: Own elaboration.

	6 nm	8 nm	10 nm
A_I eqn. 4.3 (nm ns^{-1})	143.76	124.5	111.36
A_I fitted (nm ns^{-1})	52.0	40.5	29.5

Appendix B

Supporting material for "Water thermophoresis in carbon nanotubes" (Chapter 5)

B.1 Simulation details

In this section the setup and details of the conducted Molecular Dynamics (MD) simulations are explained. As stated in Chapter 5, water droplets of 400, 600 and 800 water molecules and a CNT with chirality vector of (17,17) is used. For all the cases, we perform the simulations in three consecutive stages. First, each system is equilibrated in the NVT ensemble at 300 K during 0.5 ns using the Berendsen thermostat. Subsequently, the cases are conducted in the NVE ensemble for 1.5 ns. And third, the constrained or unconstrained simulation are conducted for 3 ns.

The constrained velocity simulation are MD simulations that allows the study of the dynamics of a motile particle at constant velocity. The technique consists of computing the center of mass velocity (v_{com}) at the end of every time step, next, this v_{com} is subtracted to the instantaneous velocity of each water molecule in the droplet, and then, the target velocity or constrained velocity (v_{const}) value is added. Thereby, we are forcing the droplet to move with a target velocity value v_{const}, without affecting the velocity distribution of the molecules in the droplet. Therefore, in the constrained simulations during each time step, the velocity of the droplet center of mass is stored, and the difference between the computed v_{com} and the constrained velocity v_{const} over the time step determines the force acting on the droplet, as defined in eqn. (B.1),

$$F_N = m \cdot a = m \cdot \frac{dv}{dt} \approx m \cdot \frac{(v_{com} - v_{const})}{\delta t} \tag{B.1}$$

where m is the total mass of the droplet and δt is the time step of the simulations (2 fs). In the cases with no applied thermal gradient (constant temperature) the acting force corresponds to the friction force ($F_N = F_F$), and in the cases with imposed thermal gradient, the force acting on the droplet is a combination of the thermophoretic force and the friction force, as described in eqn. 5.1 of Chapter 5 ($F_N = F_T - F_F$).

It is important to note that the relation between the friction force (F_F) and the constrained velocity (v_{const}) is valid due to the very large slippage at the water-CNT interface [246, 263, 264]. Here, the slip velocity v_s and the center of mass velocity v_{com} are assumed to have the same value, in line with Falk et al. [257]. Moreover, due to this very large slippage of water in CNTs,

the viscous dissipation through the fluid layers is negligible. In fact, previous investigations [246, 263, 264] reported water slip lengths over 75 nm for a CNT of 2 nm in diameter, leading to a plug-like velocity profile for water confined in CNTs [20, 247]. Furthermore, Chen et al. [265] found that water spontaneously slip inside CNTs due to thermal fluctuations at room temperature.

Finally, recall that the unconstrained simulations are Nonequilibrium Molecular Dynamic simulations with an imposed thermal gradient along the CNT and free motion of the droplet.

B.2 Thermal gradient

In order to impose a thermal gradient along the CNT, two different temperatures are applied at the ends of the nanotube (see Figure 5.1.a in Chapter 5). These two temperatures produce a temperature profile along the CNT as shown in Figure B.1. The thermal gradient is represented by the slope of the linear fit measured at the center of the CNT. In the example of Figure B.1, for imposed temperatures of 370 K and 280 K the obtained thermal gradient is 0.70 K/nm. In Table B.1 the applied temperatures and the resulting thermal gradients are presented. The mean temperature for all the cases studied is 325 K.

Due to the trend displayed by the temperature profiles (Figure B.1), the force computation is performed between the 20 nm and 60 nm along the axial direction of the CNT.

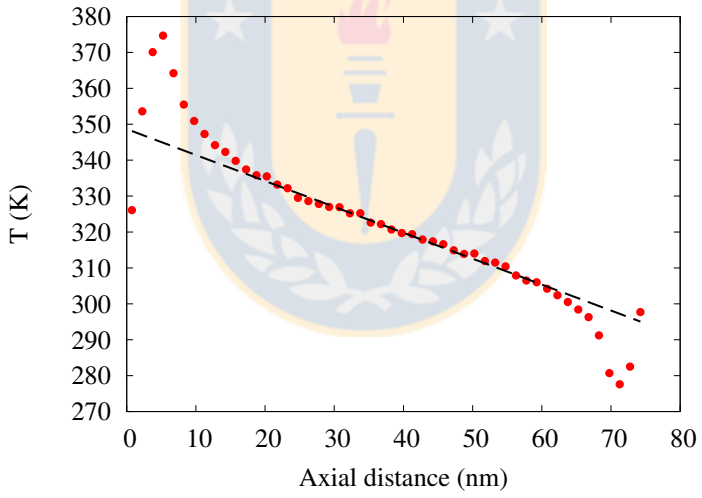

Figure B.1: Temperature profile along the carbon nanotube. The applied temperatures are 370 K and 280 K. The resulting slope (dashed line) represents the thermal gradient of 0.70 K/nm. Source: Own elaboration.

Table B.1: Thermal gradient obtained from the applied temperatures. Source: Own elaboration.

Temperatures (K)	Thermal gradient (K/nm)
340 - 310	0.20
360 - 290	0.50
370 - 280	0.70

B.3 Friction Force

As discussed in Chapter 5, the friction force acting on the motion of the droplet depends on the contact area between the droplet and the CNT. The contact area of each droplet is calculated as,

$$A = 2\pi r_{eff} L \tag{B.2}$$

where r_{eff} is the effective radius defined as,

$$r_{eff} = R - \frac{1}{2}\sigma_{CO} \tag{B.3}$$

where R is the radius of the CNT and σ_{CO} is the Lennard Jones C-O parameter. The L in equation (B.2) is the length of the droplet in contact with the CNT. To measure this length, a tracking of the droplet during the thermophoretic motions is performed, as shown in Figure B.2. Here, all the positions of the outermost water molecules in the liquid-vapor interface in the direction of the radius are saved, and from all these molecules, the one closest to the center is plotted, for both meniscus (back and front). From equation B.2 and B.3, the resulting contact area for the 400, 600 and 800 molecules are 24.3 nm^2, 36.8 nm^2 and 48.7 nm^2 respectively. The ratio between the friction force and the respective contact area as a function of the velocity of the center of mass is depicted in Figure B.3, which is a zoom of the inset in Figure 5.2.a in Chapter 5. In Figure B.3 the slope between the F_F/A ratio and velocity v [257] corresponds to the friction coefficient of the CNT(17,17) and water. This friction coefficient is 3631.3 $\pm$ 89.7 Ns/m^3.

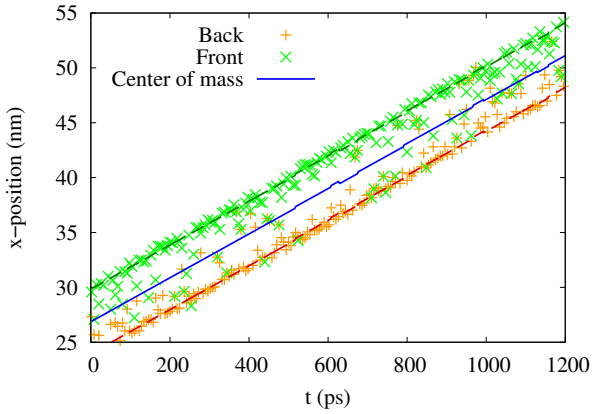

Figure B.2: Tracking of the 600 water molecule droplet. The average length is 5.88 nm. Source: Own elaboration.

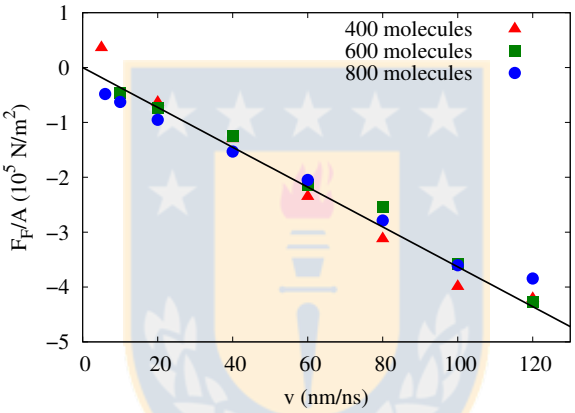

Figure B.3: Friction force divided by the solid-liquid contact area as a function of the mean velocity. The solid black line is a linear fit of the data and the slope corresponds to the friction coefficient. Source: Own elaboration.

B.4 Acceleration of the droplet

As discussed in Chapter 5 (Fig 5.3.a), a decrease in the net force F_N is observed as the velocity of the droplet increases. This result indicates that in the first regime of increasing velocity, while the thermophoretic force is constant and the friction force increases with velocity, the droplet motion occurs with a decreasing acceleration. Since $F_N = m \cdot a$, the acceleration as a function of the velocity can be computed. This is shown in Figure B.4 for thermal gradients of 0.50 K/nm (Fig B.4.a) and 0.70 K/nm (Fig B.4.b)

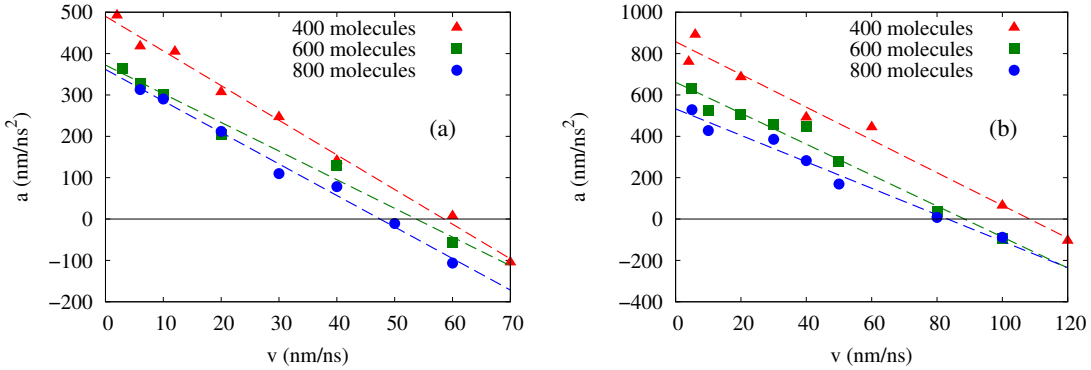

Figure B.4: Acceleration of the droplet obtained from the computed net force (F_N). The solid line is a guide for $a = 0$ and the dashed lines are fits to the data. (a) Acceleration as a function of the velocity of the center of mass (v_{com}) under a thermal gradient of 0.50 K/nm (b) Acceleration as a function of the velocity of the center of mass (v_{com}) under a thermal gradient of 0.70 K/nm. Source: Own elaboration.

B.5 Net force for different droplet sizes

In Chapter 5 we analyze how the net force F_N decreases in magnitude as the velocity of the center of mass increases for different droplet sizes (Figure 5.4.a). In Figure 5.4.a of Chapter 5, the slopes of the linear fits for each droplet size corresponds to the friction coefficient times the solid-liquid contact area. The same behavior is also observed for a thermal gradient of 0.70 K/nm, as depicted in Figure B.5.

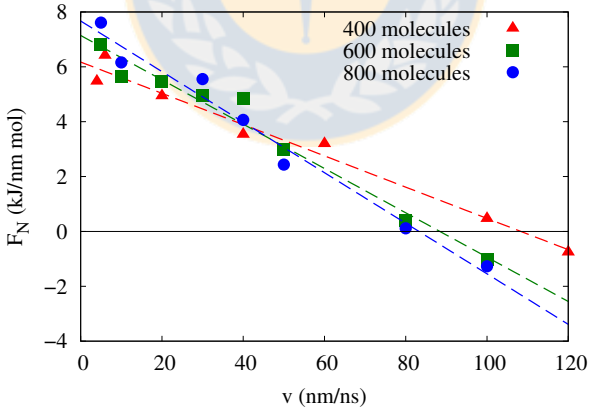

Figure B.5: Net force computed from the simulations as a function of the velocity of the center of mass. The applied thermal gradient is 0.70 K/nm. The solid line is a guide for $F_N = 0$ and the dashed lines are fits to the data. Source: Own elaboration.

Appendix C

Supporting material for "Carbon Nanotubes as Thermally Induced Water Pumps" (Chapter 7)

C.1 Simulation Protocol

In this section, the setup and details of the conducted simulations are presented. Since the density of water inside carbon nanotubes at the subcontinuum level is a topic of current debate, [294, 305–307] we implement a conical junction connecting two CNTs: one with small diameter (0.9 nm) and chirality vector (12,0), where the water density profile is unknown, and another one with a larger diameter (2.5 nm) with chirality vector (32,0), wherein the density profile is known [262, 305]. The system is shown in Figure C.1. We conducted the simulation in the NVT ensemble at 300 K for 0.5 ns and subsequently for 1.5 ns in the NVE ensemble. Next, the number of water molecules were systematically varied into the junction system until the known density profile of the CNT(32,0) was attained. The density profiles are shown in Figure C.2. In the present work, all CNTs with a chirality vector of (12,0) were filled with the number of molecules reproducing the density profile in Figure C.1. The CNT cases of (18,0) and (26,0) were filled with the density known from the literature [262, 305, 306].

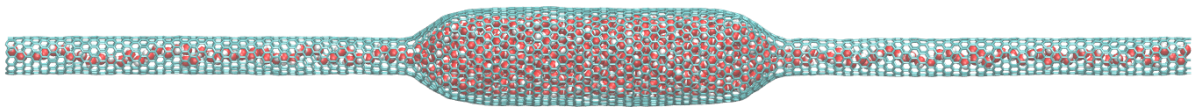

Figure C.1: Depiction of the junction between a CNT with chirality (12,0) and a CNT with chirality (32,0). This system was needed to determine the density in the (12,0) CNTs studied in this work. Source: Own elaboration.

The present simulations are performed in three stages; first an equilibration at 300K in the NVT ensemble, then a simulation in the NVE ensemble, and third a nonequilibrium simulation with an imposed thermal gradient. The thermal gradient is achieved by connecting two Berendsen thermostats with different temperatures to the carbon atoms located at the CNT ends. In a 100 ns nonequilibrium simulation, the first 20 ns are simulated for thermal gradient equilibration, and the subsequent simulation time is used for data extraction. Additionally, a 0.5 ns simulation with

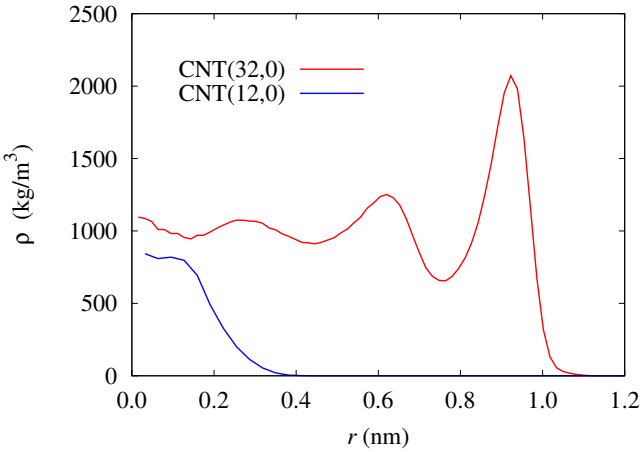

Figure C.2: Water density profiles inside the CNT(32,0) and the CNT(12,0). The density profiles are measured in the system shown in Figure C.1 at the corresponding CNT. Source: Own elaboration.

extracted data every 20 fs is conducted for the FFT analysis.

C.2 Simulated Cases

In this study each system consists of a CNT completely filled with water. The CNT had three fixed points, one each at either end (near the periodic boundaries) and one in between the two ends, as shown in Figure 7.1 of Chapter 7. For all these systems, the applied temperatures and computed mean velocities are listed in Table C.1.

Table C.1: Summary of the thermal pumps analyzed in this study. Source: Own elaboration.

Case	Length (nm)	Diameter (nm)	Applied Temperatures (K)	Effective Gradient (K/nm)	Fixed Middle Position (nm)	Mean Velocity (m/s)
1	30	0.94	320-270	1.6	14.3	1.8
2	30	0.94	340-270	2.3	14.3	3.3
3	30	0.94	360-260	3.3	14.3	5.3
4	30	0.94	330-330	0.0	14.3	0.0
5	60	0.94	330-300	0.5	30.0	1.26
6	60	0.94	360-260	2.0	30.0	3.3
7	60	0.94	360-260	2.0	18.4	2.8
8	60	0.94	360-260	2.0	41.0	4.5
9	60	0.94	360-260	2.0	15.0	3.6
10	60	0.94	360-260	2.0	13.4	3.4
11	60	0.94	340-340	0.0	30.0	0.0
12	60	0.94	340-340	0.0	18.4	0.0
13	60	0.94	340-340	0.0	41.0	0.0
14	35	1.41	320-270	1.3	17.6	1.02
15	35	1.41	340-270	1.9	17.6	1.10
16	35	1.41	360-260	3.0	17.6	2.90
17	35	2.04	320-270	1.3	18.0	2.4
18	35	2.04	340-270	1.9	18.0	2.0
19	35	2.04	360-360	3.0	18.0	3.03

C.3 Temperature Profile

The different temperatures imposed at each CNT end induce an axial temperature profile along the CNT, similar to the ones shown in Figure C.3. In the simulated cases, the main goal of the middle-fixed point was to restrain the CNT position without distorting significantly the temperature profile along the tube axis. To provide an explanation, we studied two cases including simulations of CNTs with and without the middle-fixed point. For the two cases, a 30 nm long CNT (12,0) with imposed temperatures of 360 K and 260 K at each CNT end, was used. The corresponding temperature profiles are shown in Figure C.3; the red line corresponds to the case with 3 fixed points; the blue line is the temperature profile in the case with 2 fixed points, one at each end. According to this figure, the central fixed point modifies the conductivity locally, whereas the temperature profile is not altered significantly.

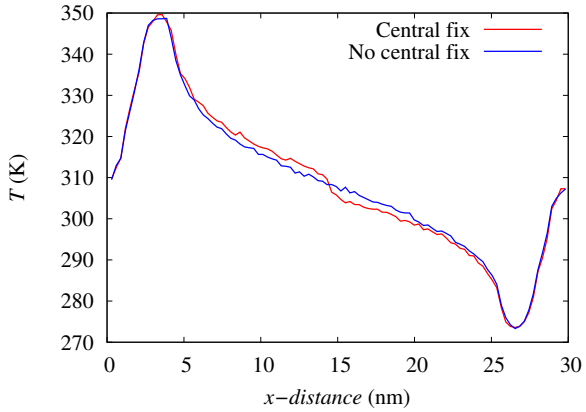

Figure C.3: Temperature profile through the 30 nm-long CNT with and without the central fixed point. The blue line (−) is the typical temperature profile in a single-wall CNT. The red line (−) is the temperature profile for the CNT with the central point fixed. Source: Own elaboration.

C.4 Vibrational Analysis

In order to describe the vibrations and the resulting oscillations of the CNT, the vibrational modes of the system were computed. Vibrational modes are described by particular frequencies in the sinusoidal oscillation of the CNT which are called natural frequencies. A complete analysis is performed by computing the amplitudes and frequencies on each system of CNTs filled with water. In this investigation, we used the procedure developed for CNTs by Pine et al. [298] to extract the amplitude and frequencies in the simulated cases.

This method consists of the following subsequent steps: first, the computational domain is divided into several bins along the axial direction (z) of the CNT and then, within each bin, the instantaneous position of the center of mass of the carbon atoms is computed. Subsequently, with the extracted signal of the center of mass, a Fast Fourier Transform (FFT) is applied to the data. For example, considering the 60 nm-long CNT(12,0), the signal at 23 nm is shown in Figure C.4. By applying a FFT to the data, the corresponding FFT spectrum is shown in Figure C.5. Here, three vibrational modes are clearly recognized.

A comparison between the FFT signal and the original signal is presented in Figure C.6. In this figure, the red line denotes the data extracted from the simulation (Figure C.4), the blue line represents the FFT solution signal using the entire frequency range, and the green line is the FFT solution signal computed from the frequencies and amplitudes of the three vibrational modes only. This FFT analysis is performed for all bins in each case studied in this work.

To further investigate the driving mechanism discussed in Chapter 7, we conducted two additional simulations of the 60 nm-long (12,0) CNT. Additional fixed points at 1/4 and 1/5 along the CNT length were studied. The purpose of this study was to analyze the "activated" vibrational mode due to the restricted position of the carbon atom along the CNT. The vibrational analysis of the cases restricted at 1/4 and 1/5 length are shown in Figures C.7 and C.8, respectively. These cases are listed as numbers 9 and 10 in Table C.1, respectively.

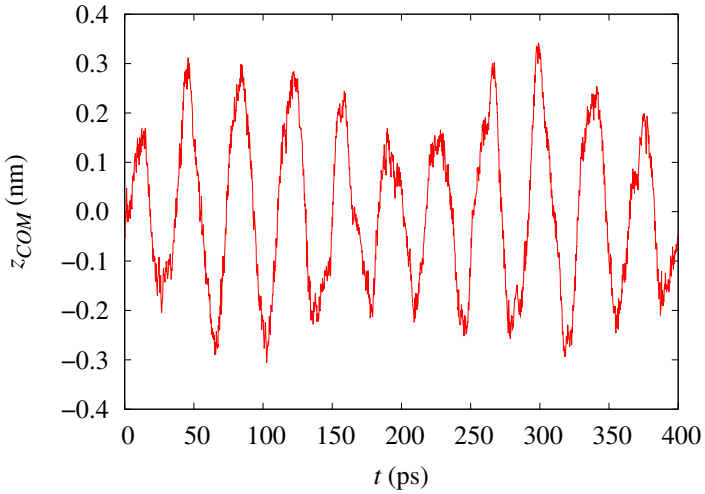

Figure C.4: Temporal oscillation signal of the 60 nm-long (12,0) CNT at 23 nm along the axis. Source: Own elaboration.

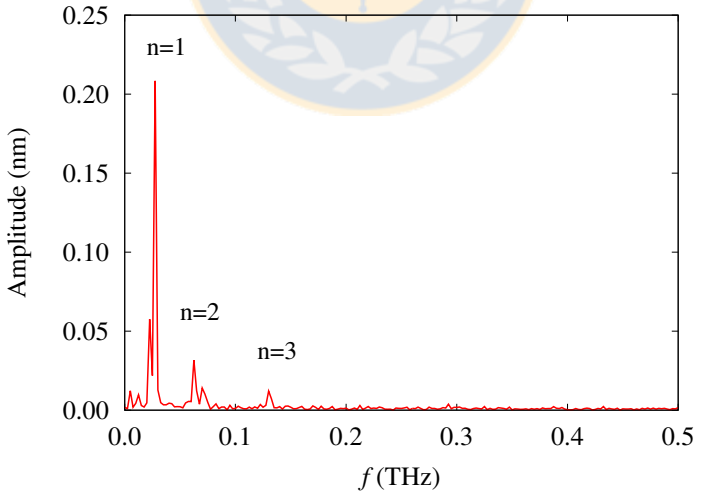

Figure C.5: FFT spectrum of the 60 nm-long, (12,0) CNT at 23 nm along the axial direction. The frequencies for the 1-3 vibrational modes are 0.0275, 0.0625 and 0.130 THz, respectively. Source: Own elaboration.

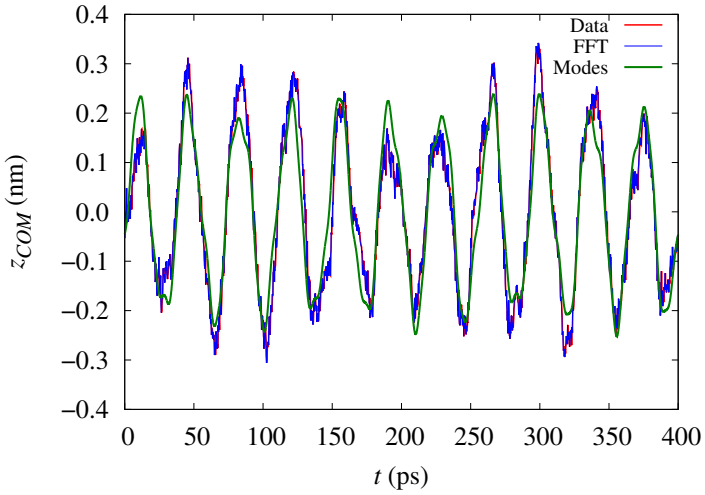

Figure C.6: Oscillation signals of the 60 nm-long (12,0) CNT at 23 nm in the axial direction. The red line (−) shows the data extracted from the simulations, the blue line (−) is the FFT signal over the entire frequency range, and the green line (−) depicts the FFT signal when using the frequencies and amplitudes of only the first three vibrational modes. Source: Own elaboration.

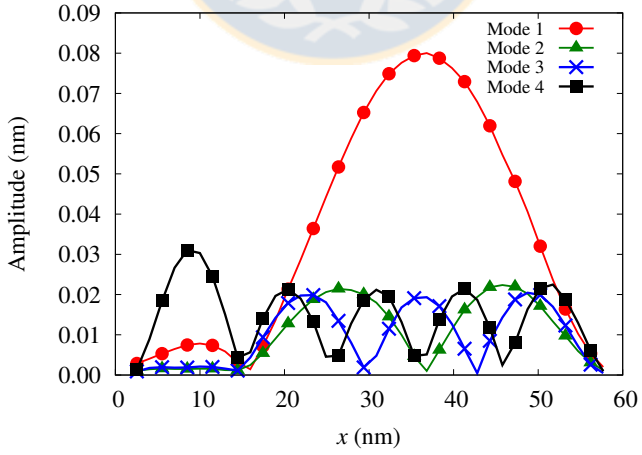

Figure C.7: Vibrational analysis of the 60 nm-long (12,0) CNT with middle-fixed point at 1/4 of its overall length. The applied thermal gradient is 2 K/nm. This case corresponds to case 9 in Table C.1. Source: Own elaboration.

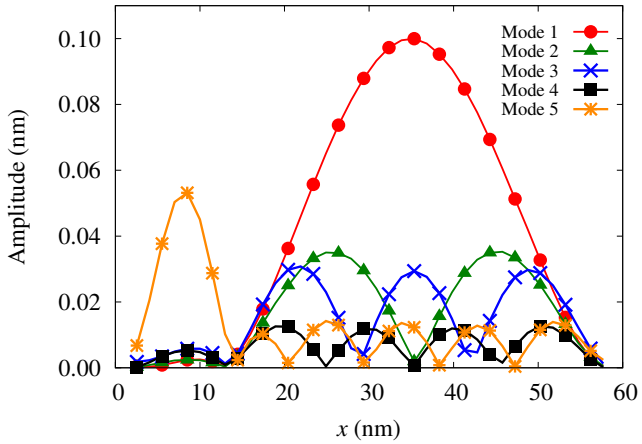

Figure C.8: Vibrational analysis of the 60 nm-long (12,0) CNT with fixed point at 1/5 of its overall length. The applied thermal gradient is 2 K/nm. This case corresponds to case 10 in Table C.1. Source: Own elaboration.

C.5 Water Flow at Different CNT Lengths

The cases wherein the temperature difference is maintained while the particular CNT length varies (distance between the heated zones) are discussed in the following. In this context, the thermal gradient decreases as the CNT length increases. Previous works [20, 106], which studied thermally-driven mechanisms to transport liquids and solids, have reported that as the thermal gradient decreases the net velocity of the motile particle is lower. Therefore, the water flow rate is expected to decline as the system length is increased for the same temperature difference applied. Here, we compare two cases with the same CNT diameter and applied temperatures, but different CNT lengths. In both cases, the middle-fixed point is located at the corresponding geometric center (halfway along the CNT length). The cases are listed as 3 and 6 in Table C.1, and the corresponding water velocity profiles are shown in Figure C.9; these profiles confirm that a shorter CNT (higher temperature gradient) displays a higher water flow rate.

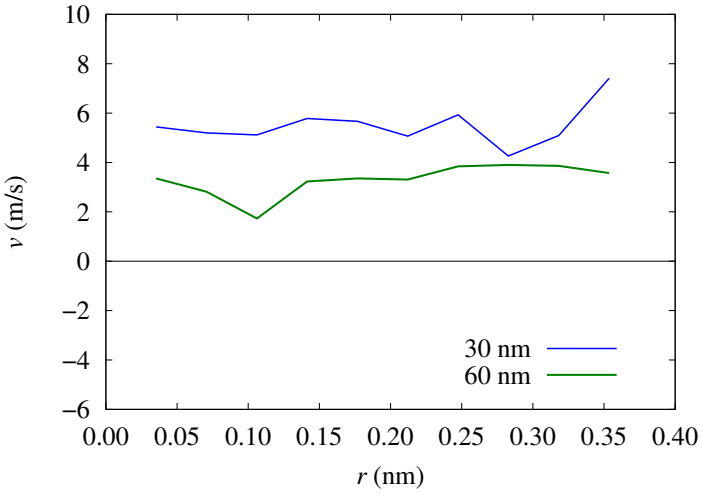

Figure C.9: Radial velocity profiles for water flow in CNT with lengths of 30 and 60 nm and the same applied temperatures at the end points. In both cases, the diameter is 0.94 nm, the chirality vector is (12,0), and the applied temperatures are 360 K and 260 K. The blue line (−) denotes the radial velocity profile of the 30 nm-long CNT with a thermal gradient of 3.3 K/nm and mean velocity of 5.3 m/s. The green line (−) is the radial velocity profile of the 60 nm-long CNT case with a corresponding thermal gradient of 2.0 K/nm and mean velocity of 3.3 m/s. Source: Own elaboration.

C.6 Efficiency

To estimate the efficiency of the thermal motor, a CNT with chiral vector (12,0) and length of 30 nm was used. The efficiency is computed by

$$\eta = \frac{E_{out}}{E_{in}} \tag{C.1}$$

where E_{out} is the output energy, which, in our study is defined as the useful energy to overcome the solid-liquid friction, and E_{in} is the input energy defined here as the thermal energy coming from the thermostat. The energy required by the fluid to overcome the friction (useful or net energy) during one time step is computed as

$$E_{out} = F_F v_{com} \delta t \tag{C.2}$$

where F_F is the friction force, v_{com} is the velocity of the center of mass of water and δt is the time step of the simulations (2 fs). Due to the very large slippage inherent in the flow of water in CNTs [246, 263, 264], the viscous dissipation in the fluid is negligible. In fact, previous investigations [246, 263, 264] reported water slip length over 75 nm for a CNT of 2 nm in diameter, leading to a plug-like velocity profile for water confined in CNTs [20, 247], similar to those measured here (see Figure 7.3a of Chapter 7 and Figure C.9). Furthermore, Chen et al. [265] found that water spontaneously slip inside CNTs due to thermal fluctuations at room temperature.

At low velocities, the relation between the friction force and the slip velocity is

$$F_F/A = -\lambda v_s \tag{C.3}$$

where A is the contact area, λ the friction coefficient and v_s the slip velocity. From equation C.3, the slope of F_F/A vs. v_s is the friction coefficient λ.

In order to compute the friction coefficient, a new set of simulations were conducted. These simulations imposed the velocity of the center of mass v_{com} of water every time step, and then, by integrating the equations of motion, the force acting on the water molecules was computed every time step [106, 252]. The relation between the friction force (F_F) and the constrained velocity (v_{com}) is possible due to the very large slippage in the water-CNT interface [246, 263, 264], assuming an equivalent value between the slip velocity v_s and the mean velocity v_{com}, in line with Falk et al. [257].

The output energy (E_{out}) at the corresponding mean velocity (v_{com}) was computed as

$$E_{out} = -A\lambda v_{com}^2 \delta t \tag{C.4}$$

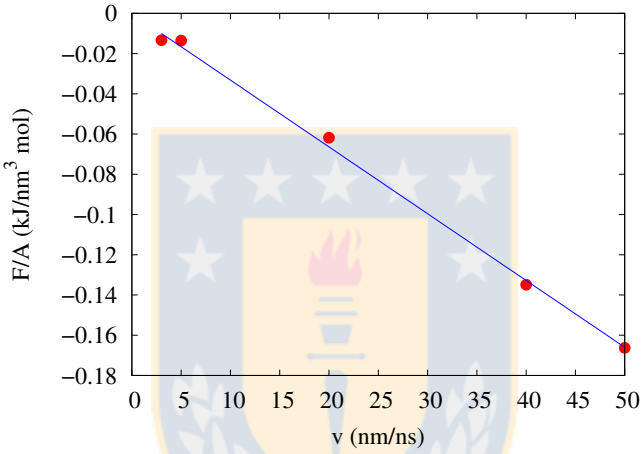

Figure C.10: Friction force divided by the solid-liquid contact area as a function of the mean velocity, at 300 K. Each point is obtained from independent simulation of 5 ns. The solid line (−) is a fit to the data obtained by imposing v=0 and F=0. The slope, which corresponds to the friction coefficient, is -0.00331981 $\frac{kJ\,ns}{nm^4\,mol}$. Source: Own elaboration.

The friction coefficient λ was obtained from the slope of F_F/A vs. v_{com}, as shown in Figure C.10. From the linear fit, the friction coefficient is

$$\lambda = -0.00331981 \frac{kJ\,ns}{nm^4\,mol}$$

or the same

$$\lambda = -5512.7 \frac{Ns}{m^3}$$

The contact area was calculated as

$$A = 2\pi r_{eff} L \tag{C.5}$$

where r_{eff} is the effective CNT radius defined as

$$r_{eff} = R - \frac{1}{2}\sigma_{CO} \tag{C.6}$$

Table C.2: Efficiency of the studied Brownian ratchet under different conditions. Different applied temperatures and two coupling constants of the Berendsen thermostat were considered. The listed v_{com} is the mean velocity extracted from the simulation of 5 ns conducted to study the energy balance in the system. The listed v_{com} is different from the mean velocity extracted from the ∼80 ns long simulations. Source: Own elaboration.

Applied T (K)	Coupling (ps)	$\mathbf{E_{in}}$ (10^{-3} kJ/ mol)	v_{com} (nm/ns)	$\mathbf{E_{out}}$ (10^{-3} kJ/ mol)	η
360-260	0.01	22.0135	4.54478	0.0079734	0.00036
	0.1	1.224	2.01429	0.0015662	0.0012
340-270	0.01	20.931	5.43903	0.0114198	0.00055
	0.1	0.821	2.48268	0.00237936	0.00290
320-270	0.01	19.737	2.86917	0.00317782	0.00016
	0.1	0.6244	3.13438	0.0037924	0.00607

In our system the area of contact is A=58.14 nm^2.

The input energy (E_{in}) is calculated from the difference between the kinetic energy coming from the high temperature thermostat and the kinetic energy removed at the low-temperature thermostat. An example of the kinetic energy behavior for a thermal gradient of 3.3 K/nm during 1 ns is shown in Figure C.11. The efficiency of the motor under different thermal conditions is presented in Table C.2. Each energy simulation is conducted for 5 ns.

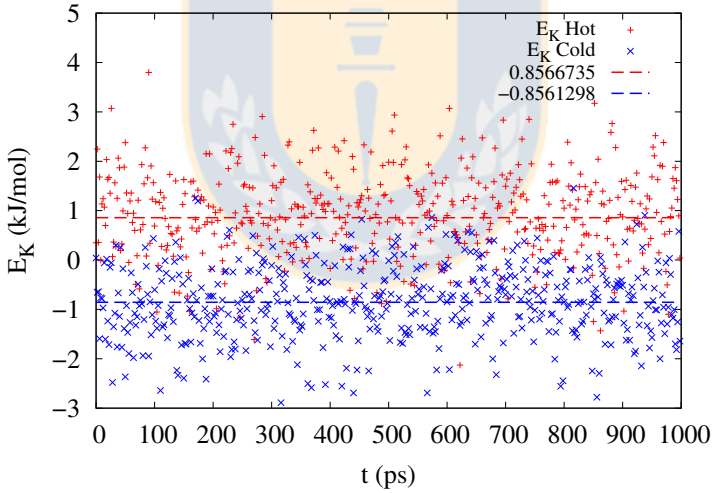

Figure C.11: Kinetic energy input (red) and kinetic energy output (blue) from the thermostats in a case with an applied thermal gradient of 3.3 K/nm. The dashed lines are the mean value of the respective kinetic energies. The difference between the two kinetic energies corresponds to the energy input (E_{in}) in the Brownian ratchet. Source: Own elaboration.

C.7 Removing Fixed Points

In the proposed thermal pump, we find that there is no net water flow when all fixed points are removed. In order to confirm this fact, two additional simulations with no fixed points were conducted, consisting of zig-zag CNTs with chiral vector (26,0) and imposed thermal gradients of 3 K/nm and 5 K/nm; these simulations showed no net water flow, as depicted in Figure C.12. In summary, our results indicate that the asymmetry induced by the thermal gradient alone is not sufficient to produce flow.

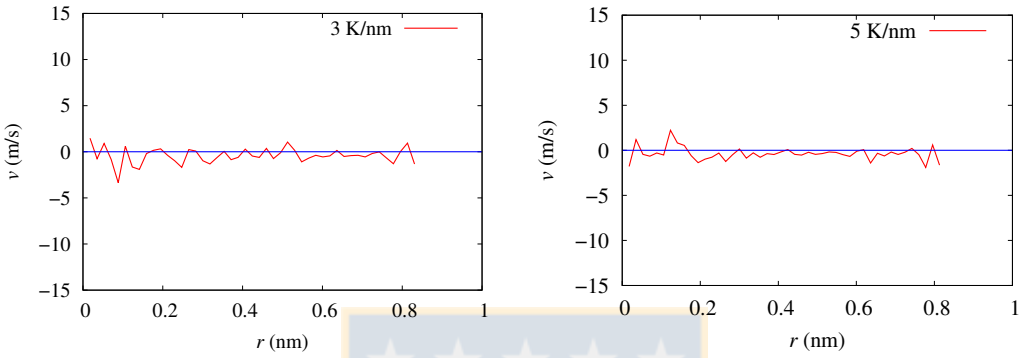

Figure C.12: Radial velocity profiles of water inside a CNT with diameter of 2 nm. The chirality vector is (26,0) and the imposed thermal gradients are 3 K/nm and 5 K/nm, as marked. These simulations had no fixed points. Source: Own elaboration.

We noted that if only the central fixed point is removed, the spatial asymmetry is not completely removed. Indeed, as inferred from Figure C.13, irrespectively of the central fixed point being present or not, the fixed points at the left and right ends of the CNT and their specular images, still impose a spatial asymmetry along the CNT. Indeed, a lower water flow is measured in the CNT when the central fixed point is absent in comparison to the CNT with the central fixed point present. Specifically, for applied temperatures of 360-260 K ($\sim$3 K/nm), a water flow velocity of 4.5 m/s was measured in the 30 nm-long (12,0) CNT, less than the 5.3 m/s measured for the case with the central fixed point. Further systematic modification of the position of the heaters and the two fixed positions should be evaluated, which we will address in a future work.

Figure C.13: Illustration of the system periodicity when using a computational cell with periodic boundary condition along the axial direction of the CNT. Two periodic computational cells are depicted in this image. The black spots indicate the fixed points along the CNT. The red and blue zones depict the differentially-heated sections of the CNT. Source: Own elaboration.

C.8 Central Fixed Point Position vs Flow Rate

The flow rate follows a non-monotonic relation with the position of the central fixed point, as shown in Figure C.14. For a 60 nm-long CNT(12,0), we observe that the higher flow rate is attained when the position of the fixed point is located at ca. 40 nm from the left end of the CNT. Nevertheless, in the nanopump presented here, the flow rates are determined by a complex relation between the imposed thermal gradient, the size of the CNT and the particular position of the central fixed point. Therefore, more studies are required to explore the existence of an optimal position of the central fixed point to maximize the flow rate for different CNT sizes. Optimizing the pumping mechanism presented here is beyond the scope of the present study, which is focused on demonstrating the phenomenon and the main parameters affecting it.

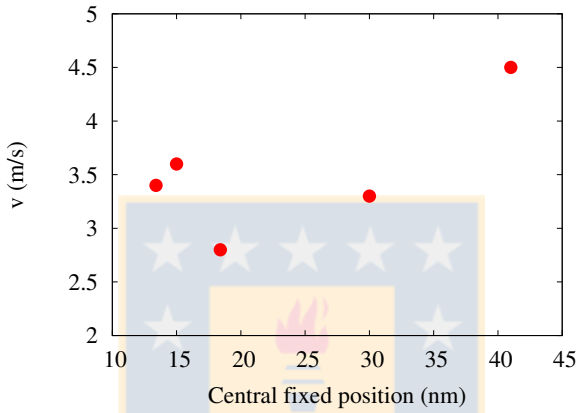

Figure C.14: Water flow velocity as a function of the position of the central fixed point. The position is measured from the left end of the CNT. The applied thermal gradient is 2 K/nm in a 60 nm-long (12,0) CNT. Source: Own elaboration.

C.9 Lowest Applied Thermal Gradient

We conducted an additional case in order to evaluate the performance of the thermal pump at low gradients. For that, a thermal gradient of 0.5 K/nm is imposed in a 60 nm long (12,0) CNT filled with water, applying temperatures of 330 K and 300 K respectively on the two heaters. To remove the thermal noise we conducted this simulation over 120 ns with a time step of 2 fs. As in previous cases, in order to impose the spatial asymmetry, three carbon atoms are immobilized on the nanotube, at its two ends and its geometric center (Figure 7.1.b of Chapter 7). From the atomic trajectories, a net water flow velocity of 1.3 m/s is measured. The temperature and velocity profiles are depicted in Figure C.15.

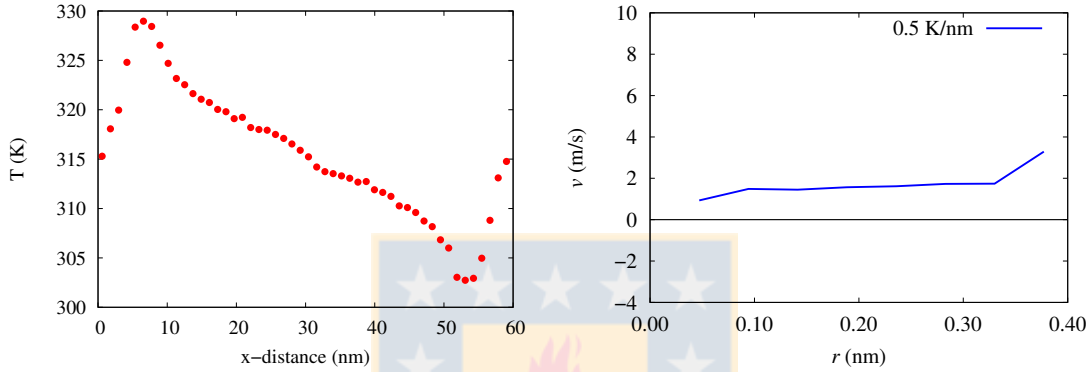

Figure C.15: Temperature and velocity profiles of a 60 nm long CNT with an imposed thermal gradient of 0.5 K/nm. Left: Axial temperature profile along the CNT. Right: Radial velocity profile of water. This case is listed as number 5 in Table C.1. Source: Own elaboration.

Publications and Conferences

First author publications

1. Elton Oyarzua, Jens H. Walther, Andrés Mejía and Harvey A. Zambrano. Early regimes of water capillary flow in slit silica nanochannels. *Phys. Chem. Chem. Phys.* 17(22):14731-14239, 2015.

2. Elton Oyarzua, Jens H. Walther, Constantine M. Megaridis, Petros Koumoutsakos and Harvey A. Zambrano. Carbon Nanotubes as Thermally Induced Water Pumps. *ACS nano.* 11(10):997-10002, 2017.

3. Elton Oyarzua, Jens H. Walther and Harvey A. Zambrano. Early regimes of water capillary flow in slit silica nanochannels. *Phys. Chem. Chem. Phys.* 20:3672-3677, 2018.

Co-author publications

1. Nabin Kumar Karna, Elton Oyarzua, Jens H. Walther and Harvey A. Zambrano. Effect of the meniscus contact angle during early regimes of spontaneous imbibition in nanochannels. *Phys. Chem. Chem. Phys.* 18(47):31997-320011, 2016.

2. Enrique Wagemann, Elton Oyarzua, Jens H. Walther and Harvey A. Zambrano. Slip divergence of water in graphene nanochannels: the role of chirality. *Phys. Chem. Chem. Phys.* 19(13):8646-8652, 2017.

Conferences

1. Elton Oyarzua, Harvey A. Zambrano, Jens H. Walther and Andrés Mejía. Early regimes of water imbibition in nanoslit silica channels. In 67th Annual Meeting of The American Physical Society – DFD, San Francisco, California USA. 2014.

2. Elton Oyarzua, Jens H. Walther and Harvey H. Zambrano. Atomistic study of a nanometer-scale pump based on the thermal ratchet concept. In 68th Annual Meeting of The American Physical Society – DFD, Boston, Massachusetts USA. 2015.

3. Elton Oyarzua, Jens H. Walther and Harvey H. Zambrano. CNT based thermal Brownian motor to pump water in nanodevices. In 69th Annual Meeting of The American Physical Society – DFD, Portland, Oregon USA. 2016.

4. Elton Oyarzua, Jens H. Walther and Harvey H. Zambrano. Thermophoretic transport of water nanodroplets confined in carbon nanotubes: the role of friction. In 70th Annual Meeting of The American Physical Society – DFD, Denver, Colorado USA. 2017.

Bibliography

[1] Michael F. Hochella Jr. There's plenty of room at the bottom: Nanoscience in geochemistry. *Geochim. Cosmochim. Acta*, 66(5):735–743, 2002.

[2] Hui-Hai Liu and Jens Birkholzer. On the relationship between water flux and hydraulic gradient for unsaturated and saturated clay. *J. Hydrology*, 475:242–247, 2012.

[3] Jun Gao, Yaping Feng, Wei Guo, and Lei Jiang. Nanofluidics in two-dimensional layered materials: Inspirations from nature. *Chem. Soc. Rev.*, 46(17):5400–5424, 2017.

[4] Simon Gravelle, Laurent Joly, François Detcheverry, Christophe Ybert, Cécile Cottin-Bizonne, and Lydéric Bocquet. Optimizing water permeability through the hourglass shape of aquaporins. *Proc. Natl. Acad. Sci. USA*, 110(41):16367–16372, 2013.

[5] Michelle L. Kovarik and Stephen C. Jacobson. Attoliter-scale dispensing in nanofluidic channels. *Anal. Chem.*, 79(4):1655–1660, 2007.

[6] Joost W. Van Honschoten, Nataliya Brunets, and Niels R. Tas. Capillarity at the nanoscale. *Chem. Soc. Rev.*, 39(3):1096–1114, 2010.

[7] Michelle L. Kovarik and Stephen C. Jacobson. Nanofluidics in lab-on-a-chip devices. *Anal. Chem.*, 81(17):7133–7140, 2009.

[8] Chao Wang, Sung-Wook Nam, John M. Cotte, Christopher V. Jahnes, Evan G. Colgan, Robert L. Bruce, Markus Brink, Michael F. Lofaro, Jyotica V. Patel, and Lynne M. Gignac. Wafer-scale integration of sacrificial nanofluidic chips for detecting and manipulating single DNA molecules. *Nat. Commun.*, 8:14243, 2017.

[9] Jianping Fu, Reto B. Schoch, Anna L. Stevens, Steven R. Tannenbaum, and Jongyoon Han. A patterned anisotropic nanofluidic sieving structure for continuous-flow separation of DNA and proteins. *Nature Nanotechnol.*, 2(2):121, 2007.

[10] Longhua Hu, Anthony G. Vecchiarelli, Kiyoshi Mizuuchi, Keir C. Neuman, and Jian Liu. Brownian ratchet mechanisms of ParA-mediated partitioning. *Plasmid*, 92:12–16, 2017.

[11] Lasse Højlund Thamdrup, Fredrik Persson, Henrik Bruus, Anders Kristensen, and Henrik Flyvbjerg. Experimental investigation of bubble formation during capillary filling of sio 2 nanoslits. *Appl. Phys. Lett.*, 91(16):163505–163505, 2007.

[12] Keliu Wu, Zhangxin Chen, Jing Li, Xiangfang Li, Jinze Xu, and Xiaohu Dong. Wettability effect on nanoconfined water flow. *Proc. Natl. Acad. Sci. USA*, 114(13):3358–3363, 2017.

[13] Ling Liu, Jianbing Zhao, Patricia J. Culligan, Yu Qiao, and Xi Chen. Thermally responsive fluid behaviors in hydrophobic nanopores. *Langmuir*, 25(19):11862–11868, 2009.

[14] Kumar Varoon Agrawal, Steven Shimizu, Lee W. Drahushuk, Daniel Kilcoyne, and Michael S. Strano. Observation of extreme phase transition temperatures of water confined inside isolated carbon nanotubes. *Nature Nanotechnol.*, 12(3):267–273, 2017.

[15] Mehdi Neek-Amal, Francois M. Peeters, Irina V. Grigorieva, and Andre K. Geim. Commensurability effects in viscosity of nanoconfined water. *ACS Nano.*, 10(3):3685–3692, 2016.

[16] Truong Quoc Vo and BoHung Kim. Transport phenomena of water in molecular fluidic channels. *Scientific Reports*, 6:33881, 2016.

[17] Jens H. Walther, Konstantinos Ritos, Eduardo R. Cruz-Chu, Constantine M. Megaridis, and Petros Koumoutsakos. Barriers to superfast water transport in carbon nanotube membranes. *Nano Lett.*, 13(5):1910–1914, 2013.

[18] Winarto, Daisuke Takaiwa, Eiji Yamamoto, and Kenji Yasuoka. Separation of water–ethanol solutions with carbon nanotubes and electric fields. *Phys. Chem. Chem. Phys.*, 18(48):33310–33319, 2016.

[19] Laurent Joly, François Detcheverry, and Anne-Laure Biance. Anomalous ζ potential in foam films. *Phys. Rev. Lett.*, 113(8):088301, 2014.

[20] Harvey A. Zambrano, Jens H. Walther, Petros Koumoutsakos, and Ivo F. Sbalzarini. Thermophoretic motion of water nanodroplets confined inside carbon nanotubes. *Nano Lett.*, 9(1):66–71, 2009.

[21] Kuiwen Zhao and Huiying Wu. Fast water thermo-pumping flow across nanotube membranes for desalination. *Nano Lett.*, 15(6):3664–3668, 2015.

[22] Cameron L. C. Smith, Anil H. Thilsted, Jonas N. Pedersen, Tomas H. Youngman, Julia C. Dyrnum, Nicolai A. Michaelsen, Rodolphe Marie, and Anders Kristensen. Photothermal transport of DNA in entropy-landscape plasmonic waveguides. *ACS Nano.*, 11(5):4553–4563, 2017.

[23] L. H. Thamdrup, N. B. Larsen, and A. Kristensen. Light-induced local heating for thermophoretic manipulation of DNA in polymer micro- and nanochannels. *Nano Lett.*, 10:826–832, 2010.

[24] Yuhui He, Makusu Tsutsui, Ralph H. Scheicher, Fan Bai, Masateru Taniguchi, and Tomoji Kawai. Thermophoretic manipulation of DNA translocation through nanopores. *ACS Nano.*, 7(1):538–546, 2013.

[25] Peter Reimann. Brownian motors: Noisy transport far from equilibrium. *Phys. Rep.*, 361(2):57–265, 2002.

[26] Z. C. Tu and Z. C. Ou-Yang. A molecular motor constructed from a double-walled carbon nanotube driven by temperature variation. *Journal of Physics: Condensed Matter*, 16(8):1287, 2004.

[27] Albert Van Den Berg, Harold G. Craighead, and Peidong Yang. From microfluidic applications to nanofluidic phenomena. *Chem. Soc. Rev.*, 39(3):899–900, 2010.

[28] Wouter Sparreboom, Albert van den Berg, and Jan CT Eijkel. Principles and applications of nanofluidic transport. *Nature Nanotechnol.*, 4(11):713, 2009.

[29] Pierre-Gilles de Gennes, Francoise Brochard-Wyart, and David Quere. *Capillarity and Wetting Phenomena:Drops, Bubbles, Pearls, Waves*. Springer-Verlag New York, 2004.

[30] David Brewster. *The Edinburgh Encyclopedia*, volume 15. Joseph and Edward Parker; William Brown, printer, 1832.

[31] Peter Rowlands. *Newton-Innovation And Controversy*. World Scientific, 2017.

[32] Yves Pomeau and Emmanuel Villermaux. Two hundred years of capillarity research. *Phys. Today*, 59(3):39, 2006.

[33] I. Newton, W., and J. Innys. *Opticks: Or, A Treatise of the Reflections, Refractions, Inflections and Colours of Light. ...* Opticks: Or, A Treatise of the Reflections, Refractions, Inflections and Colours of Light. W. and J. Innys, printers to the Royal Society, at the Prince's-Arms in St. Paul's Church-Yard., 1718.

[34] James Jurin. An account of some experiments shown before the royal society; with an enquiry into the cause of the ascent and suspension of water in capillary tubes. by james jurin, md and r. soc. s. *Philosophical Transactions (1683-1775)*, 30:739–747, 1717.

[35] Thomas Young. Iii. an essay on the cohesion of fluids. *Philosophical transactions of the royal society of London*, 95:65–87, 1805.

[36] Pierre Simon de Laplace. *Théorie de l'action capillaire*. Courcier, 1806.

[37] Jacob N. Israelachvili. *Intermolecular and surface forces: Revised third edition*. Academic press, 2011.

[38] John G. Kirkwood and Frank P. Buff. The statistical mechanical theory of surface tension. *J. Chem. Phys.*, 17(3):338–343, 1949.

[39] Gabriel V. Lau, Ian J. Ford, Patricia A. Hunt, Erich A. Müller, and George Jackson. Surface thermodynamics of planar, cylindrical, and spherical vapour-liquid interfaces of water. *J. Chem. Phys.*, 142(11):114701, 2015.

[40] Nicolas Bruot and Frédéric Caupin. Curvature dependence of the liquid-vapor surface tension beyond the tolman approximation. *Phys. Rev. Lett.*, 116(5):056102, 2016.

[41] M. J. P. Nijmeijer, C. Bruin, A. B. Van Woerkom, A. F. Bakker, and J. M. J. Van Leeuwen. Molecular dynamics of the surface tension of a drop. *J. Chem. Phys.*, 96(1):565–576, 1992.

[42] Richard C. Tolman. The effect of droplet size on surface tension. *J. Chem. Phys.*, 17(3):333–337, 1949.

[43] Antonin Marchand, Joost H. Weijs, Jacco H. Snoeijer, and Bruno Andreotti. Why is surface tension a force parallel to the interface? *Am. J. Phys.*, 79(10):999–1008, 2011.

[44] Henrik Bruus. *Theoretical microfluidics*, volume 18. Oxford University Press, 2008.

[45] Richard Lucas. Ueber das zeitgesetz des kapillaren aufstiegs von flüssigkeiten. *Kolloid-Zeitschrift*, 23(1):15–22, 1918.

[46] Edward W. Washburn. The dynamics of capillary flow. *Phys. Rev.*, 17(3):273, 1921.

[47] Emanuel Elizalde, Raúl Urteaga, and Claudio L. A. Berli. Precise capillary flow for paper-based viscometry. *Microfluid. Nanofluid.*, 20(10):135, 2016.

[48] Pingkeng Wu, Alex D. Nikolov, and Darsh T. Wasan. Capillary rise: Validity of the dynamic contact angle models. *Langmuir*, 33(32):7862–7872, 2017.

[49] Huawei Li, Junjie Zhong, Yuanjie Pang, Seyed Hadi Zandavi, Aaron Harrinarine Persad, Yi Xu, Farshid Mostowfi, and David Sinton. Direct visualization of fluid dynamics in sub-10 nm nanochannels. *Nanoscale*, 9(27):9556–9561, 2017.

[50] Siddhartha Das, Prashant R. Waghmare, and Sushanta K. Mitra. Early regimes of capillary filling. *Phys. Rev. E*, 86(6):067301, Dec 2012.

[51] B. V. Zhmud, F. Tiberg, and K. Hallstensson. Dynamics of capillary rise. *J. Coll. Interface Sci.*, 228(2):263–269, 2000.

[52] S. Supple and N. Quirke. Rapid imbibition of fluids in carbon nanotubes. *Phys. Rev. Lett.*, 90(21):214501, 2003.

[53] N. Fries and M. Dreyer. The transition from inertial to viscous flow in capillary rise. *J. Coll. Interface Sci.*, 327(1):125–128, 2008.

[54] Laurent Joly. Capillary filling with giant liquid/solid slip: Dynamics of water uptake by carbon nanotubes. *J. Chem. Phys.*, 135(21):214705, 2011.

[55] Yan Xiao, Fuzheng Yang, and Ranga Pitchumani. A generalized analysis of capillary flows in channels. *J. Coll. Interface Sci.*, 298(2):880 – 888, 2006.

[56] Michael Dreyer, Antonio Delgado, and Hans-Joseph Path. Capillary rise of liquid between parallel plates under microgravity. *J. Coll. Interface Sci.*, 163(1):158–168, 1994.

[57] D. Quéré. Inertial capillarity. *Europhys. Lett.*, 39(5):533, 1997.

[58] J. Hyväluoma, P. Raiskinmäki, A. Jäsberg, A. Koponen, M. Kataja, and J. Timonen. Simulation of liquid penetration in paper. *Phys. Rev. E*, 73(3):036705, 2006.

[59] D. I. Dimitrov, A. Milchev, and K. Binder. Capillary rise in nanopores: Molecular dynamics evidence for the Lucas-Washburn equation. *Phys. Rev. Lett.*, 99(5):054501, 2007.

[60] Jianchao Cai and Boming Yu. A discussion of the effect of tortuosity on the capillary imbibition in porous media. *Transport Porous Med.*, 89(2):251–263, 2011.

[61] C. H. Bosanquet. LV. on the flow of liquids into capillary tubes. *The London, Edinburgh, and Dublin Philosophical Magazine and Journal of Science*, 45(267):525–531, 1923.

[62] Niels Roelof Tas, J. Haneveld, Henricus V. Jansen, M. Elwenspoek, and Albert van den Berg. Capillary filling speed of water in nanochannels. *Appl. Phys. Lett.*, 85(15):3274–3276, 2004.

[63] Fredrik Persson, Lasse Højlund Thamdrup, Morten Bo Lindholm Mikkelsen, S. E. Jaarlgard, Peder Skafte-Pedersen, Henrik Bruus, and Anders Kristensen. Double thermal oxidation scheme for the fabrication of SiO2 nanochannels. *Nanotechnol.*, 18(24):245301, 2007.

[64] Jung Min Oh, Telli Faez, Sissi de Beer, and Frieder Mugele. Capillarity-driven dynamics of water–alcohol mixtures in nanofluidic channels. *Microfluid. Nanofluid.*, 9(1):123–129, 2010.

[65] Anpan Han, Giampietro Mondin, Nicole G. Hegelbach, Nicolaas F. de Rooij, and Urs Staufer. Filling kinetics of liquids in nanochannels as narrow as 27 nm by capillary force. *J. Coll. Interface Sci.*, 293(1):151–157, 2006.

[66] Jeroen Haneveld, Niels R. Tas, Nataliya Brunets, Henri V. Jansen, and Miko Elwenspoek. Capillary filling of sub-10nm nanochannels. *J. Appl. Phys.*, 104(1):014309, 2008.

[67] Peter G. Petrov and Jordan G. Petrov. Comparison of the static and dynamic contact angle hysteresis at low velocities of the three-phase contact line. *Colloids and Surfaces*, 61(0):227 – 240, 1991.

[68] P. Joos, P. Van Remoortere, and M. Bracke. The kinetics of wetting in a capillary. *J. Coll. Interface Sci.*, 136(1):189–197, 1990.

[69] R. V. Sedev, C. J. Budziak, J. G. Petrov, and A. W. Neumann. Dynamic contact angles at low velocities. *J. Coll. Interface Sci.*, 159(2):392–399, 1993.

[70] V. D. Sobolev, N. V. Churaev, M. G. Velarde, and Z. M. Zorin. Surface tension and dynamic contact angle of water in thin quartz capillaries. *J. Coll. Interface Sci.*, 222(1):51–54, 2000.

[71] T. D. Blake and J. M. Haynes. Kinetics of liquidliquid displacement. *J. Coll. Interface Sci.*, 30(3):421–423, 1969.

[72] Mihail Nicolae Popescu, John Ralston, and Rossen Sedev. Capillary rise with velocity-dependent dynamic contact angle. *Langmuir*, 24(21):12710–12716, 2008.

[73] G. Martic, F. Gentner, D. Seveno, D. Coulon, J. De Coninck, and T. D. Blake. A molecular dynamics simulation of capillary imbibition. *Langmuir*, 18(21):7971–7976, 2002.

[74] Michael E. Mackay, Tien T. Dao, Anish Tuteja, Derek L. Ho, Brooke Van Horn, Ho-Cheol Kim, and Craig J. Hawker. Nanoscale effects leading to non-einstein-like decrease in viscosity. *Nature Mat.*, 2(11):762, 2003.

[75] Deborah Ortiz-Young, Hsiang-Chih Chiu, Suenne Kim, Kislon Voïtchovsky, and Elisa Riedo. The interplay between apparent viscosity and wettability in nanoconfined water. *Nat. Commun.*, 4:2482, 2013.

[76] Niels Asger Mortensen and Anders Kristensen. Electroviscous effects in capillary filling of nanochannels. *Appl. Phys. Lett.*, 92(6):063110, 2008.

[77] Vinh-Nguyen Phan, Chun Yang, and Nam-Trung Nguyen. Analysis of capillary filling in nanochannels with electroviscous effects. *Microfluid. Nanofluid.*, 7(4):519, 2009.

[78] Marcus Hultmark, Jeffrey M. Aristoff, and Howard A. Stone. The influence of the gas phase on liquid imbibition in capillary tubes. *J. Fluid Mech.*, 678:600–606, 2011.

[79] Fabien Chauvet, Sandrine Geoffroy, Abdelkrim Hamoumi, Marc Prat, and Pierre Joseph. Roles of gas in capillary filling of nanoslits. *Soft Matter*, 8(41):10738–10749, 2012.

[80] Hong Yan, Jiuan Wei, Shuwen Cui, Shenghua Xu, Zhiwei Sun, and Ruzeng Zhu. On the applicability of Young–Laplace equation for nanoscale liquid drops. *Russ. J. Phys. Chem. A*, 90(3):635–640, 2016.

[81] Hailong Liu and Guoxin Cao. Effectiveness of the Young–Laplace equation at nanoscale. *Scientific reports*, 6:23936, 2016.

[82] Saeid Vafaei and Dongsheng Wen. Modification of the Young–Laplace equation and prediction of bubble interface in the presence of nanoparticles. *Adv. Coll. Interf. Sci.*, 225:1–15, 2015.

[83] Saul Goldman. Generalizations of the Young–Laplace equation for the pressure of a mechanically stable gas bubble in a soft elastic material. *J. Chem. Phys.*, 131(18):184502, 2009.

[84] Elton Oyarzua, Jens H. Walther, Andrés Mejía, and Harvey A. Zambrano. Early regimes of water capillary flow in slit silica nanochannels. *Phys. Chem. Chem. Phys.*, 17(22):14731–14739, 2015.

[85] Efstathios E. Michaelides. Brownian movement and thermophoresis of nanoparticles in liquids. *Int. J. Heat Mass Transfer*, 81:179–187, 2015.

[86] John Tyndall. On haze and dust. *NATURE*, 1:339–342, 1870.

[87] Robert Brown. On the particles contained in the pollen of plants; and on the general existence of active molecules in organic and inorganic bodies. *Edinburgh New Philosophical Journal*, 5:358–371, 1828.

[88] Mark Haw. Einstein's random walk. *Physics World*, 18(1):19, 2005.

[89] Albert Einstein. Über die von der molekularkinetischen theorie der wärme geforderte bewegung von in ruhenden flüssigkeiten suspendierten teilchen. *Annalen der physik*, 322(8):549–560, 1905.

[90] Marian Von Smoluchowski. Zur kinetischen theorie der brownschen molekularbewegung und der suspensionen. *Annalen der physik*, 326(14):756–780, 1906.

[91] J. Clerk Maxwell. On stresses in rarified gases arising from inequalities of temperature. *Philosophical Transactions of the royal society of London*, 170:231–256, 1879.

[92] Paul S. Epstein. Zur theorie des radiometers. *Zeitschrift für Physik*, 54(7-8):537–563, 1929.

[93] G. S. McNab and A. Meisen. Thermophoresis in liquids. *J. Coll. Interface Sci.*, 44(2):339–346, 1973.

[94] L. Talbot, R. K. Cheng, R. W. Schefer, and D. R. Willis. Thermophoresis of particles in a heated boundary layer. *J. Fluid Mech.*, 101(04):737–758, 1980.

[95] C. F. Schadt and R. D. Cadle. Thermal forces on aerosol particles1. *J. Phys. Chem.*, 65(10):1689–1694, 1961.

[96] James R. Brock. On the theory of thermal forces acting on aerosol particles. *J. Coll. Sci.*, 17(8):768–780, 1962.

[97] B. V. Derjaguin and Yu. Yalamov. Theory of thermophoresis of large aerosol particles. *J. Coll. Sci.*, 20(6):555–570, 1965.

[98] Zhigang Li and Hai Wang. Thermophoretic force and velocity of nanoparticles in the free molecule regime. *Phys. Rev. E*, 70(2):021205, 2004.

[99] Jun Wang and Zhigang Li. Thermophoretic force on micro-and nanoparticles in dilute binary gas mixtures. *Phys. Rev. E*, 84(2):021201, 2011.

[100] Jun Wang and Zhigang Li. Negative thermophoresis of nanoparticles in the free molecular regime. *Phys. Rev. E*, 86(1):011201, 2012.

[101] Jun Wang, Shuang Luo, and Guodong Xia. Thermophoretic force on nanocylinders in the free molecule regime. *Phys. Rev. E*, 95(3):033101, 2017.

[102] Minsub Han. Thermophoresis in liquids: A molecular dynamics simulation study. *J. Coll. Interface Sci.*, 284(1):339–348, 2005.

[103] Alain Martin and M. Mounir Bou-Ali. Determination of thermal diffusion coefficient of nanofluid: Fullerene–toluene. *Comptes Rendus Mécanique*, 339(5):329–334, 2011.

[104] Jacopo Buongiorno. Convective transport in nanofluids. *J. Heat Transfer*, 128(3):240–250, 2006.

[105] Zoubida Haddad, Eiyad Abu-Nada, Hakan F. Oztop, and Amina Mataoui. Natural convection in nanofluids: Are the thermophoresis and Brownian motion effects significant in nanofluid heat transfer enhancement? *Internat. J. Thermal Sci.*, 57:152–162, 2012.

[106] Philipp A. E. Schoen, Jens H. Walther, Salvatore Arcidiacono, Dimos Poulikakos, and Petros Koumoutsakos. Nanoparticle traffic on helical tracks: Thermophoretic mass transport through carbon nanotubes. *Nano Lett.*, 6(9):1910–1917, 2006.

[107] Amelia Barreiro, Riccardo Rurali, Eduardo R. Hernandez, Joel Moser, Thomas Pichler, Laszlo Forro, and Adrian Bachtold. Subnanometer motion of cargoes driven by thermal gradients along carbon nanotubes. *Science*, 320(5877):775–778, 2008.

[108] Matthew Becton and Xianqiao Wang. Thermal gradients on graphene to drive nanoflake motion. *J. Chem. Theory Comput.*, 10(2):722–730, 2014.

[109] Emanuele Panizon, Roberto Guerra, and Erio Tosatti. Ballistic thermophoresis of adsorbates on free-standing graphene. *Proc. Natl. Acad. Sci. USA*, 114(34):E7035–E7044, 2017.

[110] Philipp A. E. Schoen, Jens H. Walther, Dimos Poulikakos, and Petros Koumoutsakos. Phonon assisted thermophoretic motion of gold nanoparticles inside carbon nanotubes. *Appl. Phys. Lett.*, 90(25):253116, 2007.

[111] Matukumilli V. D. Prasad and Baidurya Bhattacharya. Phonon scattering dynamics of thermophoretic motion in carbon nanotube oscillators. *Nano Lett.*, 16(4):2174–2180, 2016.

[112] M. v. Smoluchowski. M. v. smoluchowski, phys. z. 13, 1069 (1912). *Phys. Z.*, 13:1069, 1912.

[113] Richard P. Feynman, Robert B. Leighton, Matthew Sands, and E. M. Hafner. The Feynman lectures on physics; vol. i. *Am. J. Phys.*, 33(9):750–752, 1965.

[114] Christian Van den Broeck, Ryoichi Kawai, and Pascal Meurs. Microscopic analysis of a thermal Brownian motor. *Phys. Rev. Lett.*, 93(9):090601, 2004.

[115] Christian Van den Broeck, Pascal Meurs, and Ryoichi Kawai. From Maxwell demon to Brownian motor. *New J. Phys.*, 7(1):10, 2005.

[116] Z. C. Tu. Efficiency at maximum power of Feynman's ratchet as a heat engine. *J. Phys. A: Math. Theor.*, 41(31):312003, 2008.

[117] Juan M. R. Parrondo and Pep Español. Criticism of Feynman's analysis of the ratchet as an engine. *Am. J. Phys.*, 64(9):1125–1130, 1996.

[118] Z. C. Tu and X. Hu. Molecular motor constructed from a double-walled carbon nanotube driven by axially varying voltage. *Phys. Rev. B*, 72(3):033404, 2005.

[119] Charles S. Peskin, Garrett M. Odell, and George F. Oster. Cellular motions and thermal fluctuations: The Brownian ratchet. *Biophys. J.*, 65(1):316–324, 1993.

[120] Anthony G. Vecchiarelli, Ling Chin Hwang, and Kiyoshi Mizuuchi. Cell-free study of f plasmid partition provides evidence for cargo transport by a diffusion-ratchet mechanism. *Proc. Natl. Acad. Sci. USA*, 110(15):E1390–E1397, 2013.

[121] Saveez Saffarian, Ivan E. Collier, Barry L. Marmer, Elliot L. Elson, and Gregory Goldberg. Interstitial collagenase is a Brownian ratchet driven by proteolysis of collagen. *Science*, 306(5693):108–111, 2004.

[122] Peter Hänggi and Fabio Marchesoni. Artificial Brownian motors: Controlling transport on the nanoscale. *Rev. Modern Phys.*, 81(1):387, 2009.

[123] Joel S. Bader, Richard W. Hammond, Steven A. Henck, Michael W. Deem, Gregory A. McDermott, James M. Bustillo, John W. Simpson, Gregory T. Mulhern, and Jonathan M. Rothberg. DNA transport by a micromachined Brownian ratchet device. *Proc. Natl. Acad. Sci. USA*, 96(23):13165–13169, 1999.

[124] Alexander Van Oudenaarden and Steven G. Boxer. Brownian ratchets: Molecular separations in lipid bilayers supported on patterned arrays. *Science*, 285(5430):1046–1048, 1999.

[125] Karin John, Peter Hänggi, and Uwe Thiele. Ratchet-driven fluid transport in bounded two-layer films of immiscible liquids. *Soft Matter*, 4(6):1183–1195, 2008.

[126] Andrew R. Leach. *Molecular modelling: Principles and applications.* Pearson Education, 2nd edition, 2001.

[127] Frank Jensen. *Introduction to computational chemistry.* John Wiley & Sons, 2001.

[128] Tamar Schlick. *Molecular Modeling and Simulation: An Interdisciplinary Guide*, volume 21. Springer, 2nd edition, 2010.

[129] Daan Frenkel and Berend Smit. *Understanding molecular simulation: From algorithms to applications*, volume 1. Academic press, 2nd edition, 2001.

[130] Attila Szabo and Neil S. Ostlund. *Modern quantum chemistry: Introduction to advanced electronic structure theory.* Courier Corporation, 2012.

[131] Norman L. Allinger. Conformational analysis. 130. mm2. a hydrocarbon force field utilizing v1 and v2 torsional terms. *J. Am. Chem. Soc.*, 99(25):8127–8134, 1977.

[132] Norman L. Allinger, Young H. Yuh, and Jenn Huei Lii. Molecular mechanics. the mm3 force field for hydrocarbons. 1. *J. Am. Chem. Soc.*, 111(23):8551–8566, 1989.

[133] H. J. C. Berendsen, J. R. Grigera, and T. P. Straatsma. The missing term in effective pair potentials. *J. Phys. Chem.*, 91(24):6269–6271, 1987.

[134] William L. Jorgensen, Jayaraman Chandrasekhar, Jeffry D. Madura, Roger W. Impey, and Michael L. Klein. Comparison of simple potential functions for simulating liquid water. *J. Chem. Phys.*, 79(2):926–935, 1983.

[135] Maurice L. Huggins and Joseph E. Mayer. Interatomic distances in crystals of the alkali halides. *J. Chem. Phys.*, 1(9):643–646, 1933.

[136] B. J. Alder and T. E. Wainwright. Phase transition for a hard sphere system. *J. Chem. Phys.*, 27(5):1208–1209, 1957.

[137] Berni J. Alder and T. E. Wainwright. Studies in molecular dynamics. i. general method. *J. Chem. Phys.*, 31(2):459–466, 1959.

[138] Mark Tuckerman. *Statistical mechanics: Theory and molecular simulation.* Oxford University Press, 2010.

[139] Jens H. Walther, R. Jaffe, Timur Halicioglu, and Petros Koumoutsakos. Carbon nanotubes in water: Structural characteristics and energetics. *J. Phys. Chem. B*, 105(41):9980–9987, 2001.

[140] Michael P. Allen. Introduction to molecular dynamics simulation. *Computational Soft Matter: From Synthetic Polymers to Proteins*, 23:1–28, 2004.

[141] L. N. Kantorovich. Elimination of the long-range dipole interaction in calculations with periodic boundary conditions. *Phys. Rev. B*, 60(23):15476, 1999.

[142] Hernán A. Makse, Shlomo Havlin, Moshe Schwartz, and H. Eugene Stanley. Method for generating long-range correlations for large systems. *Phys. Rev. E*, 53(5):5445, 1996.

[143] M. A. González. Force fields and molecular dynamics simulations. *École thématique de la Société Française de la Neutronique*, 12:169–200, 2011.

[144] Loup Verlet. Computer "experiments" on classical fluids. i. thermodynamical properties of Lennard-Jones molecules. *Phys. Rev.*, 159(1):98, 1967.

[145] Michael Levitt, Miriam Hirshberg, Ruth Sharon, Keith E. Laidig, and Valerie Daggett. Calibration and testing of a water model for simulation of the molecular dynamics of proteins and nucleic acids in solution. *J. Phys. Chem. B*, 101(25):5051–5061, 1997.

[146] Charles L. Brooks III, B. Montgomery Pettitt, and Martin Karplus. Structural and energetic effects of truncating long ranged interactions in ionic and polar fluids. *J. Chem. Phys.*, 83(11):5897–5908, 1985.

[147] Martine Prevost, Daniel Van Belle, Guy Lippens, and Shoshana Wodak. Computer simulations of liquid water: Treatment of long-range interactions. *Molecular Physics*, 71(3):587–603, 1990.

[148] T. Werder, Jens Honore Walther, R. L. Jaffe, T. Halicioglu, and P. Koumoutsakos. On the water-carbon interaction for use in molecular dynamics simulations of graphite and carbon nanotubes. *J. Phys. Chem. B*, 107(6):1345–1352, 2003.

[149] Valentin N. Popov. Carbon nanotubes: Properties and application. *Mat. Sci. Eng. R*, 43(3):61–102, 2004.

[150] Lukas Häner. Modular molecular builder. Master's thesis, ETH Zurich, 6 2003.

[151] David Chandler. Introduction to modern statistical mechanics. *Introduction to Modern Statistical Mechanics, by David Chandler, pp. 288. Foreword by David Chandler. Oxford University Press*, 1, 1987.

[152] J. T. Padding and Willem J. Briels. Time and length scales of polymer melts studied by coarse-grained molecular dynamics simulations. *J. Chem. Phys.*, 117(2):925–943, 2002.

[153] Robert E. Rudd and Jeremy Q. Broughton. Coarse-grained molecular dynamics and the atomic limit of finite elements. *Phys. Rev. B*, 58(10):R5893, 1998.

[154] Herman J. C. Berendsen, J. P. M. Postma, Wilfred F. van Gunsteren, A. DiNola, and J. R. Haak. Molecular dynamics with coupling to an external bath. *J. Chem. Phys.*, 81(8):3684–3690, 1984.

[155] SA Adelman and JD Doll. Generalized langevin equation approach for atom/solid-surface scattering: General formulation for classical scattering off harmonic solids. *J. Chem. Phys.*, 64(6):2375–2388, 1976.

[156] Hans C Andersen. Molecular dynamics simulations at constant pressure and/or temperature. *J. Chem. Phys.*, 72(4):2384–2393, 1980.

[157] Hideki Tanaka, Koichiro Nakanishi, and Nobuatsu Watanabe. Constant temperature molecular dynamics calculation on Lennard-Jones fluid and its application to watera. *J. Chem. Phys.*, 78(5):2626–2634, 1983.

[158] Ben Leimkuhler, Emad Noorizadeh, and Florian Theil. A gentle stochastic thermostat for molecular dynamics. *J. Stat. Phys.*, 135(2):261–277, 2009.

[159] Shuichi Nosé. A unified formulation of the constant temperature molecular dynamics methods. *J. Chem. Phys.*, 81(1):511–519, 1984.

[160] William G. Hoover. Canonical dynamics: Equilibrium phase-space distributions. *Phys. Rev. A*, 31(3):1695, 1985.

[161] Herman J. C. Berendsen. *Simulating the physical world: Hierarchical modeling from quantum mechanics to fluid dynamics*. Cambridge University Press, 2007.

[162] Glenn J. Martyna, Michael L. Klein, and Mark Tuckerman. Nosé–Hoover chains: The canonical ensemble via continuous dynamics. *J. Chem. Phys.*, 97(4):2635–2643, 1992.

[163] Brad Lee Holian, Arthur F. Voter, and Ramon Ravelo. Thermostatted molecular dynamics: How to avoid the Toda demon hidden in Nosé-Hoover dynamics. *Phys. Rev. E*, 52(3):2338, 1995.

[164] A. C. Brańka. Nosé-Hoover chain method for nonequilibrium molecular dynamics simulation. *Phys. Rev. E*, 61(5):4769, 2000.

[165] Berk Hess. *Stochastic concepts in molecular simulation*. PhD thesis, University of Groningen, 2002.

[166] Robert M. Shroll and David E. Smith. Molecular dynamics simulations in the grand canonical ensemble: Application to clay mineral swelling. *J. Chem. Phys.*, 111(19):9025–9033, 1999.

[167] V. A. Bakaev and W. A. Steele. Grand canonical ensemble computer simulation of adsorption of argon on a heterogeneous surface. *Langmuir*, 8(1):148–154, 1992.

[168] Yves Guissani and Bertrand Guillot. A numerical investigation of the liquid–vapor coexistence curve of silica. *J. Chem. Phys.*, 104(19):7633–7644, 1996.

[169] José Alejandre, Dominic J. Tildesley, and Gustavo A. Chapela. Molecular dynamics simulation of the orthobaric densities and surface tension of water. *J. Chem. Phys.*, 102(11):4574–4583, 1995.

[170] Hirofumi Daiguji. Ion transport in nanofluidic channels. *Chem. Soc. Rev.*, 39(3):901–911, 2010.

[171] Fatemeh Jabbari, Ali Rajabpour, and Seifollah Saedodin. Thermal conductivity and viscosity of nanofluids: A review of recent molecular dynamics studies. *Chem. Eng. Sci.*, 174:67–81, 2017.

[172] Christopher J. Mundy, Sundaram Balasubramanian, Ken Bagchi, Mark E. Tuckerman, Glenn J. Martyna, and Michael L. Klein. Nonequilibrium molecular dynamics. *Reviews in Computational Chemistry, Volume 14*, pages 291–397, 2000.

[173] Meisam Pourali and Ali Maghari. Non-equilibrium molecular dynamics simulation of thermal conductivity and thermal diffusion of binary mixtures confined in a nanochannel. *Chem. Phys.*, 444:30–38, 2014.

[174] Carlos Nieto-Draghi, Josep Bonet Ávalos, and Bernard Rousseau. Computing the Soret coefficient in aqueous mixtures using boundary driven nonequilibrium molecular dynamics. *J. Chem. Phys.*, 122(11):114503, 2005.

[175] D. M. Heyes, E. R. Smith, D. Dini, H. A. Spikes, and T. A. Zaki. Pressure dependence of confined liquid behavior subjected to boundary-driven shear. *J. Chem. Phys.*, 136(13):134705, 2012.

[176] David MacGowan and Denis J. Evans. Heat and matter transport in binary liquid mixtures. *Phys. Rev. A*, 34(3):2133, 1986.

[177] Andrea Perronace, Cindy Leppla, Frédéric Leroy, Bernard Rousseau, and Simone Wiegand. Soret and mass diffusion measurements and molecular dynamics simulations of n-pentane–n-decane mixtures. *J. Chem. Phys.*, 116(9):3718–3729, 2002.

[178] Gaurav Arya, Hsueh-Chia Chang, and Edward J. Maginn. A critical comparison of equilibrium, non-equilibrium and boundary-driven molecular dynamics techniques for studying transport in microporous materials. *J. Chem. Phys.*, 115(17):8112–8124, 2001.

[179] W. G. Hoover. Nonequilibrium molecular dynamics. *Annual Review of Physical Chemistry*, 34(1):103–127, 1983.

[180] Miroslav Rubeš, Jiří Kysilka, Petr Nachtigall, and Ota Bludskỳ. DFT/CC investigation of physical adsorption on a graphite (0001) surface. *Phys. Chem. Chem. Phys.*, 12(24):6438–6444, 2010.

[181] Ikutaro Hamada. Adsorption of water on graphene: A van der waals density functional study. *Phys. Rev. B*, 86(19):195436, 2012.

[182] Zhiting Li, Yongjin Wang, Andrew Kozbial, Ganesh Shenoy, Feng Zhou, Rebecca McGinley, Patrick Ireland, Brittni Morganstein, Alyssa Kunkel, Sumedh P. Surwade, et al. Effect of airborne contaminants on the wettability of supported graphene and graphite. *Nature Mat.*, 12(10):925, 2013.

[183] Wilfred F. van Gunsteren, Xavier Daura, Niels Hansen, Alan E. Mark, Chris Oostenbrink, Sereina Riniker, and Lorna J. Smith. Validation of molecular simulation: An overview of issues. *Angew. Chem. Int. Ed.*, 57(4):884–902, 2018.

[184] Joseph Wang. Cargo-towing synthetic nanomachines: Towards active transport in microchip devices. *Lab on a Chip*, 12(11):1944–1950, 2012.

[185] Byron D. Gates, Qiaobing Xu, Michael Stewart, Declan Ryan, C. Grant Willson, and George M. Whitesides. New approaches to nanofabrication: Molding, printing, and other techniques. *Chem. Rev.*, 105(4):1171–1196, 2005.

[186] Abhijit Biswas, Ilker S. Bayer, Alexandru S. Biris, Tao Wang, Enkeleda Dervishi, and Franz Faupel. Advances in top–down and bottom–up surface nanofabrication: Techniques, applications & future prospects. *Adv. Coll. Interf. Sci.*, 170(1-2):2–27, 2012.

[187] Huigao Duan and Karl K. Berggren. Directed self-assembly at the 10 nm scale by using capillary force-induced nanocohesion. *Nano Lett.*, 10(9):3710–3716, 2010.

[188] Wouter Sparreboom, Albert van den Berg, and Jan C. T. Eijkel. Transport in nanofluidic systems: A review of theory and applications. *New J. Phys.*, 12(1):015004, 2010.

[189] M. Whitby and N. Quirke. Fluid flow in carbon nanotubes and nanopipes. *Nature Nanotechnol.*, 2(2):87, 2007.

[190] Patrick Abgrall and Nam Trung Nguyen. Nanofluidic devices and their applications. *Anal. Chem.*, 80(7):2326–2341, 2008.

[191] Di Wei, Marc JA Bailey, Piers Andrew, and Tapani Ryhänen. Electrochemical biosensors at the nanoscale. *Lab on a Chip*, 9(15):2123–2131, 2009.

[192] Tuan Vo-Dinh, Brian M. Cullum, and David L. Stokes. Nanosensors and biochips: Frontiers in biomolecular diagnostics. *Sensors and Actuators B: Chemical*, 74(1-3):2–11, 2001.

[193] Kannan Balasubramanian. Challenges in the use of 1d nanostructures for on-chip biosensing and diagnostics: A review. *Biosensors and Bioelectronics*, 26(4):1195–1204, 2010.

[194] Jongho Lee, Tahar Laoui, and Rohit Karnik. Nanofluidic transport governed by the liquid/vapour interface. *Nature Nanotechnol.*, 9(4):317, 2014.

[195] James Munsie Bell and F. K. Cameron. The flow of liquids through capillary spaces. *J. Phys. Chem.*, 10(8):658–674, 1906.

[196] Miguel Angel González and José LF Abascal. The shear viscosity of rigid water models. *J. Chem. Phys.*, 132(9):096101, 2010.

[197] Ramona S. Taylor, Liem X. Dang, and Bruce C. Garrett. Molecular dynamics simulations of the liquid/vapor interface of SPC/E water. *J. Phys. Chem.*, 100(28):11720–11725, 1996.

[198] C. Vega and E. De Miguel. Surface tension of the most popular models of water by using the test-area simulation method. *J. Chem. Phys.*, 126(15):154707, 2007.

[199] J. Szekely, A. W. Neumann, and Y. K. Chuang. The rate of capillary penetration and the applicability of the Washburn equation. *J. Coll. Interface Sci.*, 35(2):273–278, 1971.

[200] S. Chibbaro, L. Biferale, F. Diotallevi, S. Succi, K. Binder, D. Dimitrov, A. Milchev, S. Girardo, and D. Pisignano. Evidence of thin-film precursors formation in hydrokinetic and atomistic simulations of nano-channel capillary filling. *Europhys. Lett.*, 84(4):44003, 2008.

[201] Damien Duvivier, Terence D. Blake, and Joël De Coninck. Toward a predictive theory of wetting dynamics. *Langmuir*, 29(32):10132–10140, 2013.

[202] Die Yang, Marta Krasowska, Craig Priest, Mihail N. Popescu, and John Ralston. Dynamics of capillary-driven flow in open microchannels. *J. Phys. Chem. C*, 115(38):18761–18769, 2011.

[203] J.-T. Cheng and N. Giordano. Fluid flow through nanometer-scale channels. *Phys. Rev. E*, 65(3):031206, 2002.

[204] Simon Gruener, Tommy Hofmann, Dirk Wallacher, Andriy V. Kityk, and Patrick Huber. Capillary rise of water in hydrophilic nanopores. *Phys. Rev. E*, 79(6):067301, 2009.

[205] Jacob N. Israelachvili. Measurement of the viscosity of liquids in very thin films. *J. Coll. Interface Sci.*, 110(1):263–271, 1986.

[206] R. G. Horn, D. T. Smith, and W. Haller. Surface forces and viscosity of water measured between silica sheets. *Chemical Physics Letters*, 162(4-5):404–408, 1989.

[207] Uri Raviv, Pierre Laurat, and Jacob Klein. Fluidity of water confined to subnanometre films. *NATURE*, 413(6851):51, 2001.

[208] Hui Zhang, Ali A. Hassanali, Yun Kyung Shin, Chris Knight, and Sherwin J. Singer. The water–amorphous silica interface: Analysis of the stern layer and surface conduction. *J. Chem. Phys.*, 134(2):024705, 2011.

[209] D. Duncan, D. Li, J. Gaydos, and A. W. Neumann. Correlation of line tension and solid-liquid interfacial tension from the measurement of drop size dependence of contact angles. *J. Coll. Interface Sci.*, 169(2):256–261, 1995.

[210] Hong Peng, Greg R. Birkett, and Anh V. Nguyen. The impact of line tension on the contact angle of nanodroplets. *Mol. Sim.*, 40(12):934–941, 2014.

[211] David Quéré. Wetting and roughness. *Annu. Rev. Mater. Res.*, 38:71–99, 2008.

[212] Yoshinori Nakamura, Andreas Carlson, Gustav Amberg, and Junichiro Shiomi. Dynamic wetting at the nanoscale. *Phys. Rev. E*, 88(3):033010, 2013.

[213] TD Blake and Joël De Coninck. The influence of solid–liquid interactions on dynamic wetting. *Adv. Coll. Interf. Sci.*, 96(1-3):21–36, 2002.

[214] Wylie Stroberg, Sinan Keten, and Wing Kam Liu. Hydrodynamics of capillary imbibition under nanoconfinement. *Langmuir*, 28(40):14488–14495, 2012.

[215] M. Rauscher and S. Dietrich. Wetting phenomena in nanofluidics. *Annu. Rev. Mater. Res.*, 38:143–172, 2008.

[216] Cathy J. Ridgway, Patrick A. C. Gane, and Joachim Schoelkopf. Effect of capillary element aspect ratio on the dynamic imbibition within porous networks. *J. Coll. Interface Sci.*, 252(2):373–382, 2002.

[217] Konstantin G. Kornev and Alexander V. Neimark. Spontaneous penetration of liquids into capillaries and porous membranes revisited. *J. Coll. Interface Sci.*, 235(1):101–113, 2001.

[218] Taras Andrukh, Daria Monaenkova, Binyamin Rubin, Wah-Keat Lee, and Konstantin G Kornev. Meniscus formation in a capillary and the role of contact line friction. *Soft Matter*, 10(4):609–615, 2014.

[219] Vinh Nguyen Phan, Nam-Trung Nguyen, Chun Yang, Pierre Joseph, Lyes Djeghlaf, David Bourrier, and Anne-Marie Gue. Capillary filling in closed end nanochannels. *Langmuir*, 26(16):13251–13255, 2010.

[220] Chirodeep Bakli and Suman Chakraborty. Effect of entrapped phase on the filling characteristics of closed-end nanopores. *Soft Matter*, 11(1):161–168, 2015.

[221] Daniel Schneider, Rustem Valiullin, and Peter A Monson. Filling dynamics of closed end nanocapillaries. *Langmuir*, 30(5):1290–1294, 2014.

[222] R. Qiao and N. R. Aluru. Surface-charge-induced asymmetric electrokinetic transport in confined silicon nanochannels. *Appl. Phys. Lett.*, 86(14):143105, 2005.

[223] R. Qiao and N. R. Aluru. Charge inversion and flow reversal in a nanochannel electro-osmotic flow. *Phys. Rev. Lett.*, 92(19):198301, 2004.

[224] Christian D. Lorenz, Paul S. Crozier, Joshua A. Anderson, and Alex Travesset. Molecular dynamics of ionic transport and electrokinetic effects in realistic silica channels. *J. Phys. Chem. C*, 112(27):10222–10232, 2008.

[225] Dimitrios Argyris, David R. Cole, and Alberto Striolo. Ion-specific effects under confinement: The role of interfacial water. *ACS Nano.*, 4(4):2035–2042, 2010.

[226] Aleksandar Popadić, Jens H. Walther, Petros Koumoutsakos, and Matej Praprotnik. Continuum simulations of water flow in carbon nanotube membranes. *New J. Phys.*, 16(8):082001, 2014.

[227] Jens Honore Walther, Richard L. Jaffe, E. M. Kotsalis, Thomas Werder, Timur Halicioglu, and Petros Koumoutsakos. Hydrophobic hydration of C60 and carbon nanotubes in water. *Carbon*, 42(5):1185–1194, 2004.

[228] H. A. Zambrano, Jens Honore Walther, and R. L. Jaffe. Molecular dynamics simulations of water on a hydrophilic silica surface at high air pressures. *J. Mol. Liq.*, 198:107–113, 2014.

[229] Norman T. Huff, Ersan Demiralp, Tahir Cagin, and William A. Goddard III. Factors affecting molecular dynamics simulated vitreous silica structures. *Journal of non-crystalline solids*, 253(1-3):133–142, 1999.

[230] Nabin Kumar Karna, Elton Oyarzua, Jens H. Walther, and Harvey A. Zambrano. Effect of the meniscus contact angle during early regimes of spontaneous imbibition in nanochannels. *Phys. Chem. Chem. Phys.*, 18(47):31997–32001, 2016.

[231] Konstantin G. Kornev and Alexander V. Neimark. Modeling of spontaneous penetration of viscoelastic fluids and biofluids into capillaries. *J. Coll. Interface Sci.*, 262(1):253–262, 2003.

[232] A. V. Plyukhin. Thermophoresis as persistent random walk. *Phys. Lett. A*, 373(25):2122–2124, 2009.

[233] M. A. Rahman and M. Z. Saghir. Thermodiffusion or Soret effect: Historical review. *Int. J. Heat Mass Transfer*, 73:693–705, 2014.

[234] Seshasai Srinivasan and M. Ziad Saghir. Experimental approaches to study thermodiffusion: A review. *Internat. J. Thermal Sci.*, 50(7):1125–1137, 2011.

[235] F. Zheng. Thermophoresis of spherical and non-spherical particles: A review of theories and experiments. *Adv. Coll. Interf. Sci.*, 97:255–278, 2002.

[236] Wanguang Li and E. James Davis. The effects of gas and particle properties on thermophoresis. *J. Aerosol Sci.*, 26(7):1085–1099, 1995.

[237] F. Debbasch and J. P. Rivet. The Ludwig–Soret effect and stochastic processes. *J. Chem. Thermodynamics*, 43(3):300–306, 2011.

[238] C. Ludwig. Diffusion between unequally heated regions of initially uniform solutions. *Sitzber. Bayer Akad. Wiss. Wien*, 20:539, 1856.

[239] C. Soret. Sur l'etat d'equilibre que prend au point de vue de sa concentration une dissolution saaline primitivement homogene dont deux parties sont portees a des temperatures differentes. *Ann. Chim. Phys.*, 22:293–297, 1881.

[240] PF Geelhoed, R. Lindken, and J. Westerweel. Thermophoretic separation in microfluidics. *Chem. Eng. Res. Des.*, 84(5):370–373, 2006.

[241] Yajian Zheng, Hui Liu, Yi Wang, Cong Zhu, Shuming Wang, Jingxiao Cao, and Shining Zhu. Accumulating microparticles and direct-writing micropatterns using a continuous-wave laser-induced vapor bubble. *Lab on a Chip*, 11(22):3816–3820, 2011.

[242] Sumio Iijima. Helical microtubules of graphitic carbon. *NATURE*, 354(6348):56–58, 1991.

[243] S. Joseph and N. R. Aluru. Hierarchical multiscale simulation of electrokinetic transport in silica nanochannels a the point of zero charge. *Langmuir*, 22(21):9041–9051, 2006.

[244] Savas Berber, Young-Kyun Kwon, and David Tománek. Unusually high thermal conductivity of carbon nanotubes. *Phys. Rev. Lett.*, 84(20):4613, 2000.

[245] Mainak Majumder, Nitin Chopra, Rodney Andrews, and Bruce J. Hinds. Nanoscale hydrodynamics: Enhanced flow in carbon nanotubes. *NATURE*, 438(7064):44–44, 2005.

[246] Jason K. Holt, Hyung Gyu Park, Yinmin Wang, Michael Stadermann, Alexander B. Artyukhin, Costas P. Grigoropoulos, Aleksandr Noy, and Olgica Bakajin. Fast mass transport through sub-2-nanometer carbon nanotubes. *Science*, 312(5776):1034–1037, 2006.

[247] Sony Joseph and N. R. Aluru. Why are carbon nanotubes fast transporters of water? *Nano Lett.*, 8(2):452–458, 2008.

[248] M. M. J. Treacy, T. W. Ebbesen, and J. M. Gibson. Exceptionally high young's modulus observed for individual carbon nanotubes. *NATURE*, 381(6584):678, 1996.

[249] R. Rurali and E. R. Hernandez. Thermally induced directed motion of fullerene clusters encapsulated in carbon nanotubes. *Chem. Phys. Lett.*, 497(1):62–65, 2010.

[250] Quan-Wen Hou, Bing-Yang Cao, and Zeng-Yuan Guo. Thermal gradient induced actuation in double-walled carbon nanotubes. *Nanotechnol.*, 20(49):495503, 2009.

[251] Jige Chen, Yi Gao, Chunlei Wang, Renliang Zhang, Hong Zhao, and Haiping Fang. Impeded mass transportation due to defects in thermally driven nanotube nanomotor. *J. Phys. Chem. C*, 119(30):17362–17368, 2015.

[252] Harvey A. Zambrano, Jens Honore Walther, and Richard Lawrence Jaffe. Thermally driven molecular linear motors: A molecular dynamics study. *J. Chem. Phys.*, 131(24):241104, 2009.

[253] Zhengrong Guo, Tienchong Chang, Xingming Guo, and Huajian Gao. Mechanics of thermophoretic and thermally induced edge forces in carbon nanotube nanodevices. *J. Mech. Phys. Solids*, 60(9):1676–1687, 2012.

[254] I. Santamaría-Holek, D. Reguera, and JM Rubi. Carbon-nanotube-based motor driven by a thermal gradient. *J. Phys. Chem. C*, 117(6):3109–3113, 2013.

[255] Ning Wei, Hui-Qiong Wang, and Jin-Cheng Zheng. Nanoparticle manipulation by thermal gradient. *Nanoscale Res. Lett.*, 7(1):1–9, 2012.

[256] Junichiro Shiomi and Shigeo Maruyama. Water transport inside a single-walled carbon nanotube driven by a temperature gradient. *Nanotechnol.*, 20(5):055708, 2009.

[257] Kerstin Falk, Felix Sedlmeier, Laurent Joly, Roland R. Netz, and Lydéric Bocquet. Molecular origin of fast water transport in carbon nanotube membranes: Superlubricity versus curvature dependent friction. *Nano Lett.*, 10(10):4067–4073, 2010.

[258] Ming D. Ma, Luming Shen, John Sheridan, Jefferson Zhe Liu, Chao Chen, and Quanshui Zheng. Friction of water slipping in carbon nanotubes. *Phys. Rev. E*, 83(3):036316, 2011.

[259] Ming Ma, François Grey, Luming Shen, Michael Urbakh, Shuai Wu, Jefferson Zhe Liu, Yilun Liu, and Quanshui Zheng. Water transport inside carbon nanotubes mediated by phonon-induced oscillating friction. *Nature Nanotechnol.*, 10(8):692–695, 2015.

[260] David Van Der Spoel, Erik Lindahl, Berk Hess, Gerrit Groenhof, Alan E. Mark, and Herman J. C. Berendsen. Gromacs: fast, flexible, and free. *J. Comput. Chem.*, 26(16):1701–1718, 2005.

[261] SeongJun Heo and Susan B. Sinnott. Investigation of the influence of thermostat configurations on the mechanical properties of carbon nanotubes in molecular dynamics simulations. *J. Nanosci. Nanotechnol.*, 7(4-5):1518–1524, 2007.

[262] T. Werder, J. H. Walther, R. Jaffe, T. Halicioglu, F. Noca, and P. Koumoutsakos. Molecular dynamics simulations of contact angles of water droplets in carbon nanotubes. *Nano Lett.*, 1(12):697–702, 2001.

[263] Sridhar Kumar Kannam, B. D. Todd, Jesper Schmidt Hansen, and Peter J. Daivis. How fast does water flow in carbon nanotubes? *J. Chem. Phys.*, 138(9):094701, 2013.

[264] John A. Thomas and Alan J. H. McGaughey. Reassessing fast water transport through carbon nanotubes. *Nano Lett.*, 8(9):2788–2793, 2008.

[265] Chao Chen, Luming Shen, Ming Ma, Jefferson Zhe Liu, and Quanshui Zheng. Brownian motion-induced water slip inside carbon nanotubes. *Microfluid. Nanofluid.*, 16(1-2):305–313, 2014.

[266] G. V. Dedkov. Friction on the nanoscale: New physical mechanisms. *Materials Letters*, 38(5):360 – 366, 1999.

[267] Rakesh Rajegowda, Sridhar Kumar Kannam, Remco Hartkamp, and Sarith P. Sathian. Thermophoretic transport of ionic liquid droplets in carbon nanotubes. *Nanotechnol.*, 28(15):155401, 2017.

[268] Chunhong He and Goodarz Ahmadi. Particle deposition with thermophoresis in laminar and turbulent duct flows. *Aerosol Sci. Tech.*, 29(6):525–546, 1998.

[269] Jiong Zhao, Jia-Qi Huang, Fei Wei, and Jing Zhu. Mass transportation mechanism in electric-biased carbon nanotubes. *Nano Lett.*, 10(11):4309–4315, 2010.

[270] Daniele Vigolo, Giovanni Brambilla, and Roberto Piazza. Thermophoresis of microemulsion droplets: Size dependence of the Soret effect. *Phys. Rev. E*, 75(4):040401, 2007.

[271] Anastasios I. Skoulidas, David M. Ackerman, J. Karl Johnson, and David S. Sholl. Rapid transport of gases in carbon nanotubes. *Phys. Rev. Lett.*, 89(18):185901, 2002.

[272] R. Saito, G. Dresselhaus, and M. S. Dresselhaus. Tunneling conductance of connected carbon nanotubes. *Phys. Rev. B*, 53(4):2044, 1996.

[273] Gang Wu and Baowen Li. Thermal rectification in carbon nanotube intramolecular junctions: Molecular dynamics calculations. *Phys. Rev. B*, 76(8):085424, 2007.

[274] Qiaoli Zhou, Fanyan Meng, Zhuhong Liu, and Sanqiang Shi. The thermal conductivity of carbon nanotubes with defects and intramolecular junctions. *J. Nanomater.*, 2013(2514103):12, 2013.

[275] Jung Sang Suh, Jin Seung Lee, and Hoseong Kim. Linearly joined carbon nanotubes. *Synthetic Metals*, 123(3):381–383, 2001.

[276] Jin Seung Lee, Geun Hoi Gu, Hoseong Kim, Kwang Seok Jeong, Jiwon Bae, and Jung Sang Suh. Growth of carbon nanotubes on anodic aluminum oxide templates: Fabrication of a tube-in-tube and linearly joined tube. *Chem. Mater.*, 13(7):2387–2391, 2001.

[277] Itsuo Hanasaki, Akihiro Nakatani, and Hiroshi Kitagawa. Molecular dynamics study of ar flow and he flow inside carbon nanotube junction as a molecular nozzle and diffuser. *Science and Technology of Advanced Materials*, 5(1):107–113, 2004.

[278] Gaurav Arora and Stanley I. Sandler. Molecular sieving using single wall carbon nanotubes. *Nano Lett.*, 7(3):565–569, 2007.

[279] Jiaye Su, Keda Yang, and Hongxia Guo. Asymmetric transport of water molecules through a hydrophobic conical channel. *RSC Advances*, 4(76):40193–40198, 2014.

[280] Itsuo Hanasaki and Akihiro Nakatani. Water flow through carbon nanotube junctions as molecular convergent nozzles. *Nanotechnol.*, 17(11):2794, 2006.

[281] Brian W. Smith, Marc Monthioux, and David E. Luzzi. Encapsulated C60 in carbon nanotubes. *Nature*, 396(6709):323, 1998.

[282] Xiaoming Sun, Sasa Zaric, Dan Daranciang, Kevin Welsher, Yuerui Lu, Xiaolin Li, and Hongjie Dai. Optical properties of ultrashort semiconducting single-walled carbon nanotube capsules down to sub-10 nm. *J. Am. Chem. Soc.*, 130(20):6551–6555, 2008.

[283] Antonis N. Andriotis, Madhu Menon, Deepak Srivastava, and George Froudakis. Extreme hydrogen sensitivity of the transport properties of single-wall carbon-nanotube capsules. *Phys. Rev. B*, 64(19):193401, 2001.

[284] Hiroshi Somada, Kaori Hirahara, Seiji Akita, and Yoshikazu Nakayama. A molecular linear motor consisting of carbon nanotubes. *Nano Lett.*, 9(1):62–65, 2008.

[285] Sumio Iijima, Toshinari Ichihashi, and Yoshinori Ando. Pentagons, heptagons and negative curvature in graphite microtubule growth. *NATURE*, 356(6372):776–778, 1992.

[286] Mildred S. Dresselhaus, Gene Dresselhaus, and Peter C. Eklund. *Science of fullerenes and carbon nanotubes: Their properties and applications.* Elsevier, 1996.

[287] Aron Cummings, Mohamed Osman, Deepak Srivastava, and Madhu Menon. Thermal conductivity of Y-junction carbon nanotubes. *Phys. Rev. B*, 70(11):115405, 2004.

[288] Shigeo Maruyama, Yasuhiro Igarashi, Yuki Taniguchi, and Junichiro Shiomi. Anisotropic heat transfer of single-walled carbon nanotubes. *J. Therm. Sci. Tech.-JPN*, 1(2):138–148, 2006.

[289] Vitaly V. Chaban and Oleg V. Prezhdo. Water boiling inside carbon nanotubes: Toward efficient drug release. *ACS Nano.*, 5(7):5647–5655, 2011.

[290] Dmitry Alexeev, Jie Chen, Jens H. Walther, Konstantinos P. Giapis, Panagiotis Angelikopoulos, and Petros Koumoutsakos. Kapitza resistance between few-layer graphene and water: Liquid layering effects. *Nano Lett.*, 15(9):5744–5749, 2015.

[291] Nam-Trung Nguyen, Yee-Cheong Lam, Soon-Seng Ho, and Cassandra Lee-Ngo Low. Improvement of rectification effects in diffuser/nozzle structures with viscoelastic fluids. *Biomicrofluidics*, 2(3):034101, 2008.

[292] P. Abgrall and A. M. Gue. Lab-on-chip technologies: Making a microfluidic network and coupling it into a complete microsystem - a review. *J. Micromech. Microeng.*, 17(5):R15, 2007.

[293] Petr Král and Boyang Wang. Material drag phenomena in nanotubes. *Chem. Rev.*, 113(5):3372–3390, 2013.

[294] John A. Thomas and Alan J. H. McGaughey. Water flow in carbon nanotubes: Transition to subcontinuum transport. *Phys. Rev. Lett.*, 102:184502, May 2009.

[295] Sony Joseph and N. R. Aluru. Pumping of confined water in carbon nanotubes by rotation-translation coupling. *Phys. Rev. Lett.*, 101(6):064502, 2008.

[296] J. Azamat, J. J. Sardroodi, and A. Rastkar. Water desalination through armchair carbon nanotubes: A molecular dynamics study. *RSC Adv.*, 4(109):63712–63718, 2014.

[297] Sundus Erbas-Cakmak, David A. Leigh, Charlie T. McTernan, and Alina L. Nussbaumer. Artificial molecular machines. *Chem. Rev.*, 115(18):10081–10206, 2015.

[298] Polina Pine, Yuval E. Yaish, and Joan Adler. Simulation and vibrational analysis of thermal oscillations of single-walled carbon nanotubes. *Phys. Rev. B*, 83(15):155410, 2011.

[299] Zeke Insepov, Dieter Wolf, and Ahmed Hassanein. Nanopumping using carbon nanotubes. *Nano Lett.*, 6(9):1893–1895, 2006.

[300] Hu Qiu, Rong Shen, and Wanlin Guo. Vibrating carbon nanotubes as water pumps. *Nano Res.*, 4(3):284–289, 2011.

[301] Juan M. R. Parrondo, J. M. Blanco, F. J. Cao, and R. Brito. Efficiency of Brownian motors. *Europhys. Lett.*, 43(3):248, 1998.

[302] Lydéric Bocquet and Roland R. Netz. Nanofluidics: Phonon modes for faster flow. *Nature Nanotechnol.*, 10(8):657–658, 2015.

[303] Xingyu Lin, Qian Yang, Longhua Ding, and Bin Su. Ultrathin silica membranes with highly ordered and perpendicular nanochannels for precise and fast molecular separation. *ACS Nano.*, 9(11):11266–11277, 2015.

[304] Mainak Majumder, Nitin Chopra, and Bruce J. Hinds. Mass transport through carbon nanotube membranes in three different regimes: Ionic diffusion and gas and liquid flow. *ACS Nano.*, 5(5):3867–3877, 2011.

[305] Alessio Alexiadis and Stavros Kassinos. The density of water in carbon nanotubes. *Chem. Eng. Sci.*, 63(8):2047–2056, 2008.

[306] Jun Wang, Yu Zhu, Jian Zhou, and Xiao-Hua Lu. Diameter and helicity effects on static properties of water molecules confined in carbon nanotubes. *Phys. Chem. Chem. Phys.*, 6(4):829–835, 2004.

[307] Joshua Driskill, Davide Vanzo, Dusan Bratko, and Alenka Luzar. Wetting transparency of graphene in water. *J. Chem. Phys.*, 141(18):18C517, 2014.